Mathematical modeling of focal axonal swellings arising in traumatic brain injuries and neurodegenerative diseases.

Pedro Doria Maia

A thesis proposal
submitted in partial fulfillment of the
requirements for the degree of

Doctor of Philosophy

University of Washington

2014

Program Authorized to Offer Degree: UW Applied Mathematics

University of Washington

Abstract

Mathematical modeling of focal axonal swellings arising in traumatic brain injuries and neurodegenerative diseases.

Pedro Doria Maia

Chair of the Supervisory Committee:
Dr. J. Nathan Kutz
Department of Applied Mathematics

There is a broad need in the neuroscience, neurological and biomedical engineering communities to better classify, quantify and diagnose Focal Axonal Swellings (FAS) and their impact on cognitive deficits and/or neural functionality. FAS is a critical biomarker in several leading neurodegenerative diseases such as Alzheimer's, Parkinson's, Multiple Sclerosis, and others. They are also a hallmark feature of concussions and Traumatic Brain Injuries – the leading cause of death among youngsters worldwide and a lightning rod issue in contact sports. In this work, we discuss how different shapes of FAS can affect neuronal signaling and degrade the information encoded in spike trains. We adapted theoretical estimates, derived in idealized axonal geometry settings, to real axons with much more challenging structures. Our methods highlight potential trouble spots of axonal morphology and provide a starting point for novel FAS diagnosis. Finally, we discuss the collective effects of FAS in neuronal networks, where stable response patterns are lost, jeopardizing the system's ability to transmit information. A better understanding of the macroscopic effects of FAS pathologies – that occur at a cellular level– can shine new light onto the cognitive, behavioral, perceptual and sensory-motor impairments resulting from such disorders.

TABLE OF CONTENTS

LIST OF FIGURES

ACKNOWLEDGMENTS

I would like to express my special gratitude to my advisor Dr. J. Nathan Kutz; you have been an outstanding mentor for me, always enthusiastic and encouraging. Your advice on both research as well as on my career have been priceless. It was a privilege to be part of the Kutz Lab, where exciting cutting-edge applied math is punctuated with lunches at Chipotle and amazing *cappuccinos*. Thanks also for enabling my quarter-long visit to Harvard University during your sabbatical year at the Radcliffe Institute for Advanced Studies and my participation in several conferences and workshops.

I would also like to thank my committee members, Dr. Eric Shea-Brown, Dr. Jeffrey Riffell and Dr. Mark Kot for your assistance along these years. Professor Shea-Brown was of pivotal importance for my studies in computational neuroscience, leading vibrant journal-club discussions, multidisciplinary seminars and readings. I also thank Dr. Jeffrey Riffel for sharing his expertise in neurobiology and Dr. Mark Kot for his attentive reading and suggestions to improve this manuscript.

I am very grateful to former and current members of the Kutz lab that taught me so much: Dr. Eli Shlizerman, Dr. Edwin Ding, Dr. Matt Williams, Dr. Bingni Brunton, Dr. Steve Brunton, Dr. Xing Fu, Benjamin Lansdel and Syuzanna Sargsyan.

Several faculty members contributed to my background as an applied mathematician: Dr. Anne Greenbaum, Dr. Loyce Adams, Dr. Ulrich Hetmaniuk, Dr. Randall LeVeque and Dr. J. Nathan Kutz (Numerical Analysis and Scientific Computing), Dr. Chris Bretherton and Dr. Ka-Kit Tung (Analytical Methods), Dr. Mark Kot and Dr. Hong Qian (Biomathematics and Stochastic Analysis). I am especially thankful to Dr. Bernard Deconinck (Nonlinear waves, Dynamical Systems, Asymptotic Methods) for his dedication to students both as faculty and graduate program coordinator. To you all, my sincerest thanks.

I was very fortunate to have some of the brightest and friendliest colleagues in the Ap-

plied Mathematics Department. There are too many of you to list, but thanks for sharing the grad-school road with me, and for all the help and good company you have provided throughout these past years.

Finally, I wish to thank my friends and family for their love and never-ending support.

DEDICATION

This work is dedicated to my family and friends.

Chapter 1

INTRODUCTION

In this chapter we contextualize Concussions and Traumatic Brain Injuries (TBI), review the main *in vivo* and *in vitro* techniques, and discuss their injurious effects across different spatial scales. We discuss in depth the hallmark pathological implications of TBI at cellular level– Focal Axonal Swellings. This feature is actually universal in neurodegenerative diseases of the central nervous system such as Multiple Sclerosis, Alzheimer's disease, Parkinson's disease and others.

1.1 Traumatic Brain Injuries (TBI)

Traumatic Brain Injury (TBI) is recognized as the leading cause of death and permanent disability among young people [60]. Worldwide, 10 million deaths and/or hospitalizations annually are directly attributable to TBI and an estimated 57 million currently alive people have experienced some form of brain injury [120]. In the United States, at least 1.7 million cases are estimated per year either as an isolated injury or along with others [34]. TBI has also been described as the signature wound of the wars in Iraq and Afghanistan. More than 2,000,000 U.S. military personnel have been deployed to those countries since the beginning of the conflicts. It has been estimated that 10% - 20% of all veterans of these conflicts experienced some sort of TBI, with blast injuries being the leading cause. ([60, 120]). A growing body of evidence suggests that even mild concussions, if induced repeatedly, can lead to permanent brain damage. Such findings have made TBI a lightning rod issue in almost all contact sports, but especially football [33]. This issue is constantly in the press and mass-media vehicles:

- Sports-related brain injuries landing more kids in ERs
- Cycling is the top sport for head injuries

- High school football player dies from TBI
- How to save football from TBI

Traumatic Brain Injury is defined as damage to the brain resulting from an external mechanical force, such as that caused by rapid acceleration or deceleration, blast waves, crush, an impact or penetration by a projectile [120]. Concussions are a subclass of TBI and sometimes referred to as mild TBI. The main symptoms of TBI in humans include:

- headache, fatigue, dizziness,
- difficulty sleeping, memory problems,
- irritability, anxiety, depression,
- apathy, lack of patience,
- problems with concentration, balance and coordination.

As reviewed in [101], the pathophysiology of TBI is complex and its effects occur in many different spatial scales. See Figure 1.1. At the cellular/microscopic scale, axons can be injured and interrupt axonal transport. TBI can trigger neuroinflammation that can lead to axonal swellings and neurodegeneration (Fig. 1.1A). At larger/macroscopic scales, injuries are apparent in the white matter tracts and hemorrhage (Fig. 1.1B). Finally, at the whole brain scale, damage to tracts interrupts long-distance communication between brain regions. Damage to white matter microstructure is illustrated in Fig. 1.1C and reduced network interactions in Fig. 1.1D.

One of the most challenging aspects of research in neurodegenerative diseases and TBI is understanding how neuronal pathologies developed at a cellular level [59, 84] compromise the functionality of an entire network of neurons. It is customary to schematize TBI process as:

1. Primary Injury: is the direct result of the external force, involves mechanical tissue deformation (see Fig. 1.2).

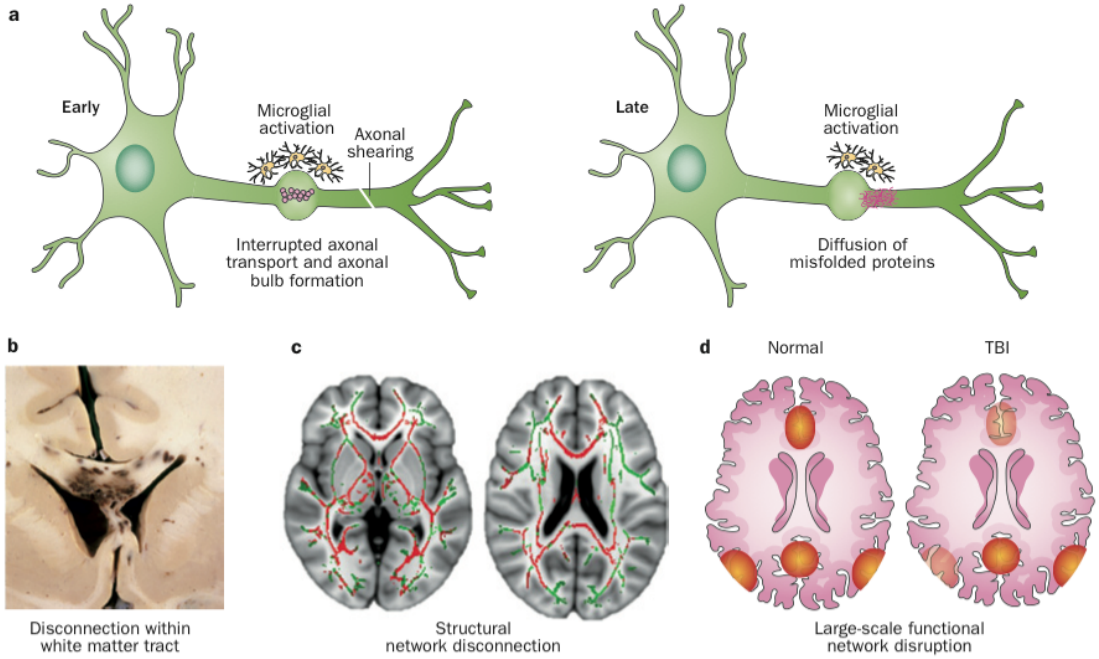

Figure 1.1: Effects of TBI across spatial scales. **a.** At the microscopic scale, axonal injury can interrupt axonal transport, produce axonal swellings, and trigger neuroinflammation that can lead to neurodegeneration. **b.** At the macroscopic scale, injuries are apparent in large white matter tracts – seen here in a postmortem specimen with black regions of haemorrhage. **c.** At the whole brain scale, damage to tracts interrupts long-distance communication between brain regions. Damage to white matter microstructure is illustrated here as reduced fractional anisotropy (red regions; green indicates intact structure). **d.** White matter damage can disrupt interactions between nodes of a brain network, represented here as reduced interactions between the default mode network (red/yellow regions). Figure from Sharp et al. [101].

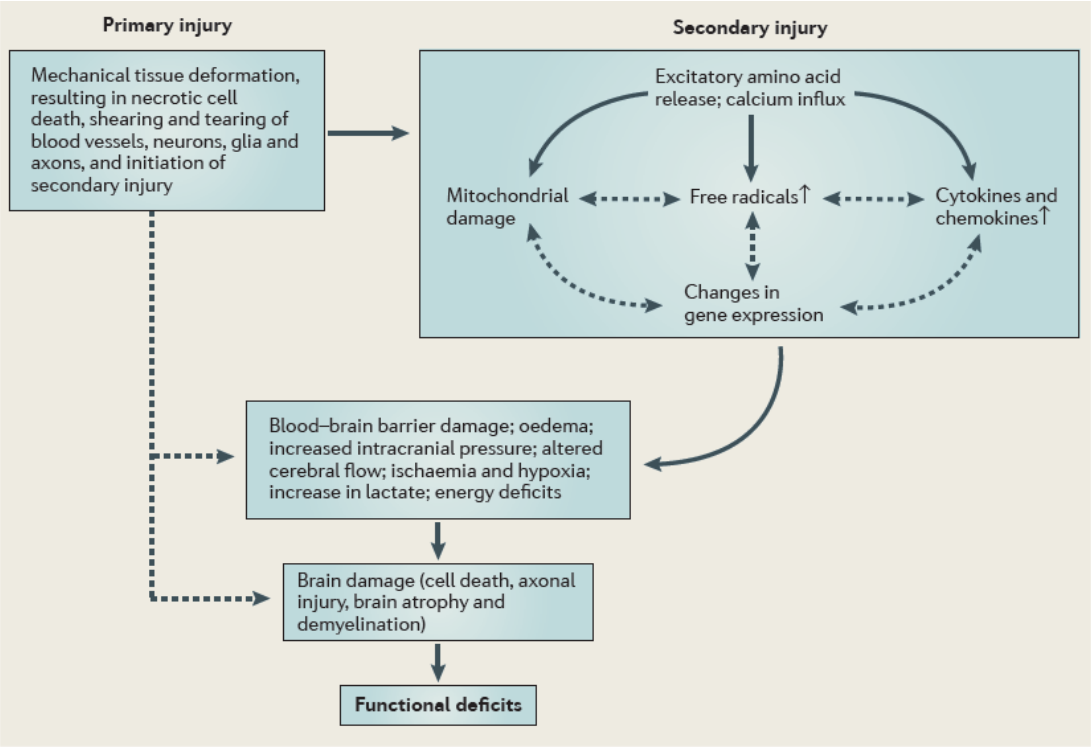

Figure 1.2: Pathophysiology schematics of Traumatic Brain Injury. The primary injury is the direct result of the external force and involves mechanical tissue deformation. It initiates secondary injury with diffuse neuronal depolarization and release of neurotransmitters and a massive influx of calcium – that leads to energy deficits, free radical formation and initiation of cell death. Studies indicate that the adult brain is capable of substantial structural and functional reorganization after injury, which may contribute to spontaneous functional recovery. Interventions targeting secondary injury mechanisms and modulating neuroplasticity promote functional recovery in animal models of TBI. Solid lines represent established interactions or pathways, whereas dashed lines represent possible interactions or pathways. Figure from Xiong et al. [120].

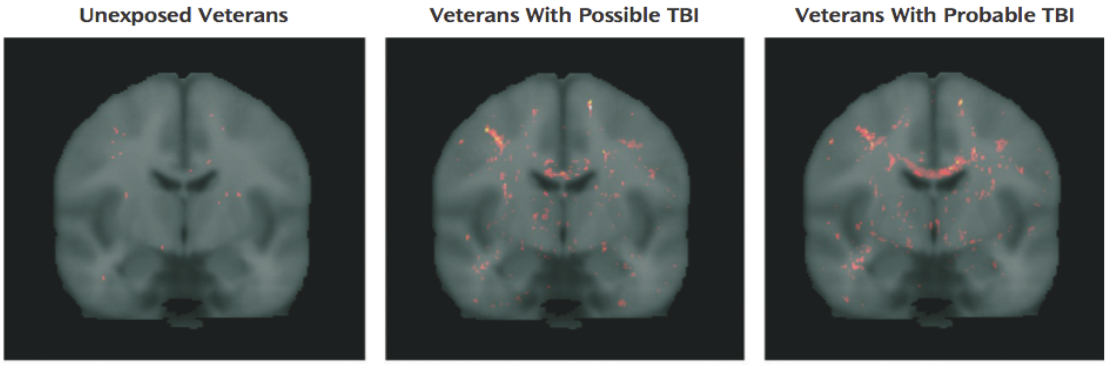

Figure 1.3: Diffusion Tensor Imaging (DTI) can detect abnormalities in white matter regions, i.e., regions with low fractional anisotropy (so called Potholes, in red). DTI is inadequate to study how damage occurs at a cellular level, and the necessary resolution can only be achieved after autopsy or via *in vitro* experiments. Figure from Jorge et al. [60].

2. Secondary Injury: complex cascade of biochemical reactions after TBI. Massive calcium influx degrade lipids, proteins and nucleic acids. Calcium sequestration in mitochondria leads to calcium disturbance, energy deficits, free radical formation and cell death. (see Fig. 1.2).

The result of these complex cascades after TBI is eventually cell damage and death, which causes functional deficits. Substantial experimental and clinical data have accumulated over the past decade indicating that the adult brain is capable of substantial structural and functional reorganization after injury, which may contribute to spontaneous functional recovery. The importance of the secondary injury is well summarized in the following passage:

> "As the primary injury occurs immediately after the moment of trauma, it can only be preventable (for example, through the use of a seat belt or helmet). By contrast, the elongated nature of secondary injury development provides a window of opportunity for therapeutic intervention, which may prevent and/or reduce secondary brain damage and improve long-term patient outcome. (...) Interventions targeting secondary injury mechanisms and modulating neuroplasticity promote functional recovery in animal models of TBI. " (Xiong et al. [120])

TBI patients usually have their brains monitored by magnetic resonance imaging techniques to reveal abnormalities in white matter fiber structure. The most common of these techniques is the Diffusion Tensor Imaging (DTI) that can reveal microscopic details about tissue architecture (location

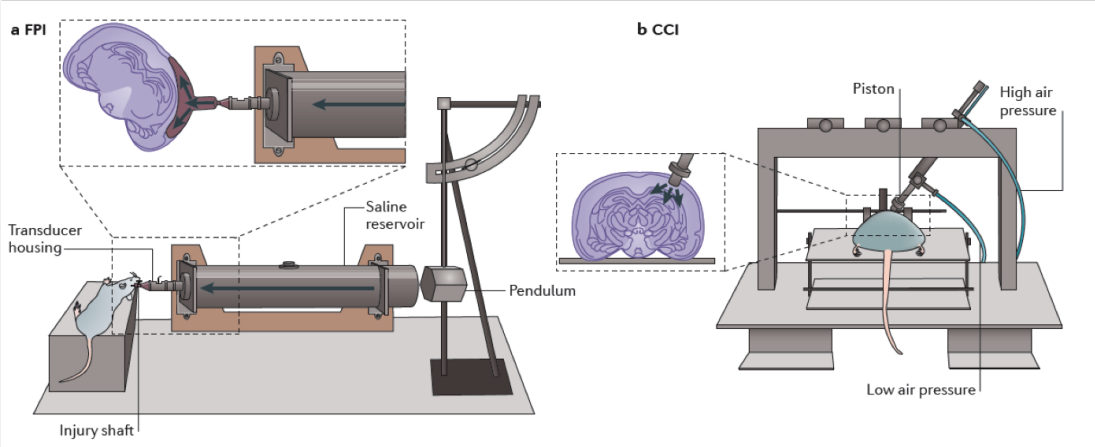

Figure 1.4: TBI experiments *in vivo*. **a.** The fluid percussion injury (FPI) device uses rapid injection of a fluid pulse into the epidural space. **b.** The controlled cortical impact (CCI) injury model uses an air or electromagnetic driven piston to penetrate the brain at a known distance and velocity. Figure from Xiong et al. [120].

and orientation of the tracts). White matter lesions and trauma change the normal diffusion orientation of water molecules (anisotropy) and are a proxy for axonal injuries. Figure 1.3 shows DTI images of of veteran's brains with mild injuries, revealing areas of decreased fractional anisotropy – potholes (in red). Overall, white matter potholes constitute a sensitive biomarker of axonal injury that can be identified in mild TBI at acute and chronic stages of its clinical course (see [60]).

1.1.1 TBI experiments in vivo

Due to the heterogeneous nature of TBI insults, numerous animal models have been developed. Although larger animals are closer in size and physiology to humans, rodents are mostly used in TBI research owing to their modest cost, small size and standardized outcome measurements. A few specific models widely used in research include ([120]):

- *Fluid Percussion Injury* (Fig 1.4A): The injury is inflicted by a pendulum striking the piston of a reservoir of fluid to generate a fluid pressure pulse to the intact dura through a craniotomy. The percussion produces brief displacement and deformation of brain tissue, and the severity

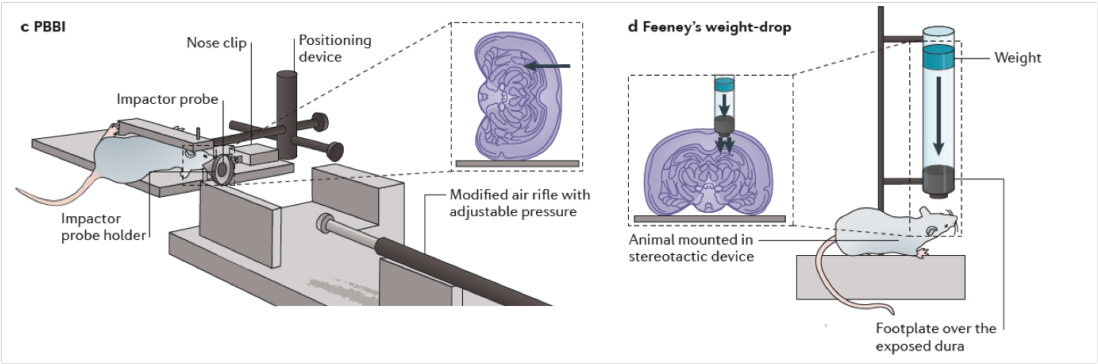

Figure 1.5: TBI experiments *in vivo*. **c.** The penetrating ballistic-like brain injury (PBBI) involves the transmission of projectiles with high energy (transmission of a metal rod or expansion of the probes elastic balloon). **d.** In Feeneys weight-drop model ([36]), a metal disk is placed over the skull to prevent bone fracture. Figure from Xiong et al. [120].

of injury depends on the strength of the pressure pulse. It is highly reproducible, allows fine tuning of injury severity but requires craniotomy and have high mortality rate. The (lateral) FPI model is one of the most widely used TBI animal models

- *Controlled Cortical Impact* (Fig 1.4B): This model uses a pneumatic or electromagnetic impact device to drive a rigid impactor onto the exposed, intact dura and mimics cortical tissue loss, acute subdural hematoma, axonal injury, concussion, blood-brain barrier dysfunction and even coma. It has been applied to ferrets, rats, mice, swine and monkeys.

- *Penetrating Ballistic-Like Brain Injury* (Fig 1.5C): This model is caused by transmission of projectiles with high energy and a leading shockwave, which produces a temporary cavity in the brain that is many times the size of the projectile itself. A novel non-fatal model for low-velocity PBBI has been established in rats involving a modified air rifle that accelerates a pellet.

- *Weight drop models* (Figs 1.5D and Fig 1.6E): In weight-drop models, the skull is exposed (with or without a craniotomy) to a free falling, guided weight. Injury severity in these models

can be altered by adjusting the mass of the weight and the height from which it falls.

1. In Feeneys weight-drop model ([36]), the weight is delivered to the intact dura through a craniotomy, which causes a cortical contusion.
2. Shohamis group ([104]) introduced a rodent model for closed head injury using a weight-drop impact delivered to one side of an unprotected skull in rats or mice while the head was placed on a hard surface.
3. Marmarou ([78]) developed a model of diffuse axonal injury to mimic diffuse TBI in humans which is typically caused by falls or motor vehicle accidents. Rats are placed on a foam bed and subjected to the impact by dropping the brass weight onto the stainless steel disc.

- *Blast TBI* (Fig 1.6F): Uses a compression-driven shock tube to simulate blast effects that mimics real blast- induced mild TBI seen in recent military conflicts. Non-impact blast injury lead prominently to diffuse axonal injury. Exposure of the head alone to a severe explosive blast causes significant neurological damage. Low level blast causes cognitive deficits (in rats).

1.1.2 TBI experiments in vitro

The non-invasive imaging techniques used in human TBI patients do not have yet enough resolution to study damage at a cellular level. It is also difficult to do physiology experiments on post-mortem animal neurons. To overcome these difficulties, several *in vitro* techniques try to mimic TBI injuries in neurons growing in cell-cultures. A few of these techniques include:

- *Beads at tip of atomic force microscope*: In the setup of Magdesian et al. ([72]), a bead attached to the tip of cantilever deliver sub-nanoNewton forces to the cell. See Figure 1.7 for details.

- *Stretch injuries*: In the setup of Hemphill et al. [52], the elastic membranes in which neurons are cultured are quickly stretched, transferring injurious forces to cells. See Figure 1.8 for details.

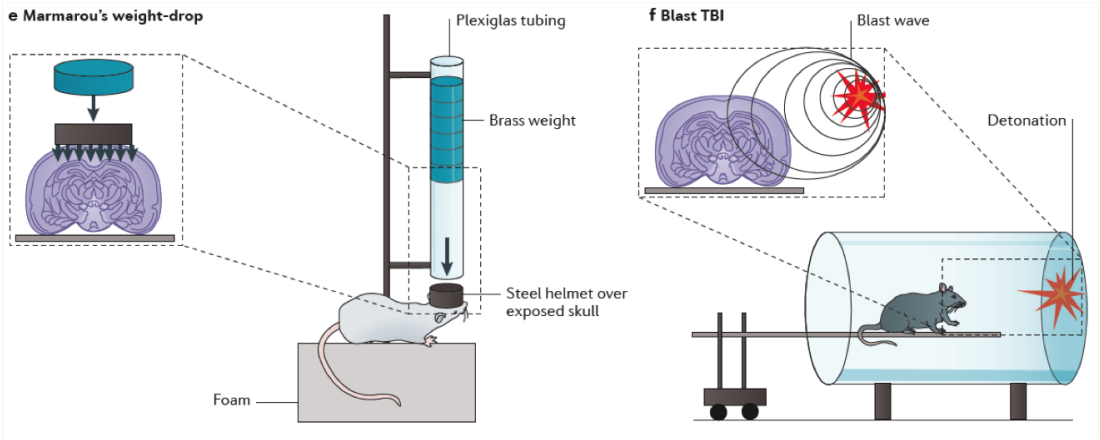

Figure 1.6: TBI experiments *in vivo*. **e.** In Marmarous weight-drop model ([78]), a metal disk is placed over the skull to prevent bone fracture. **f.** Blast brain injury can be caused by the primary injury related to the blast and other mechanisms; for example, the thoracic effect. Figure from Xiong et al. [120].

- *Impactor injuries*: In the setup of Fayaz et al. [35], a rubber impactor descends upon the neurons inflicting injury. The descent velocity can be controlled allowing for injuries of different intensities. See Figure 1.9 for details.

Such *in vitro* techniques allow detailed studies of Focused Axonal Swellings (FAS), which are the dominant hallmark feature of the impact of TBI on neurons.

1.2 Focal Axonal Swellings (FAS)

In this section we discuss Focal Axonal Swellings (FAS) in details; We review the importance of axons in neural computations and discuss FAS resulting from traumatic brain injuries and in several neurodegenerative diseases of the central nervous system, including Multiple Sclerosis, Alzheimer's and Parkinson's disease.

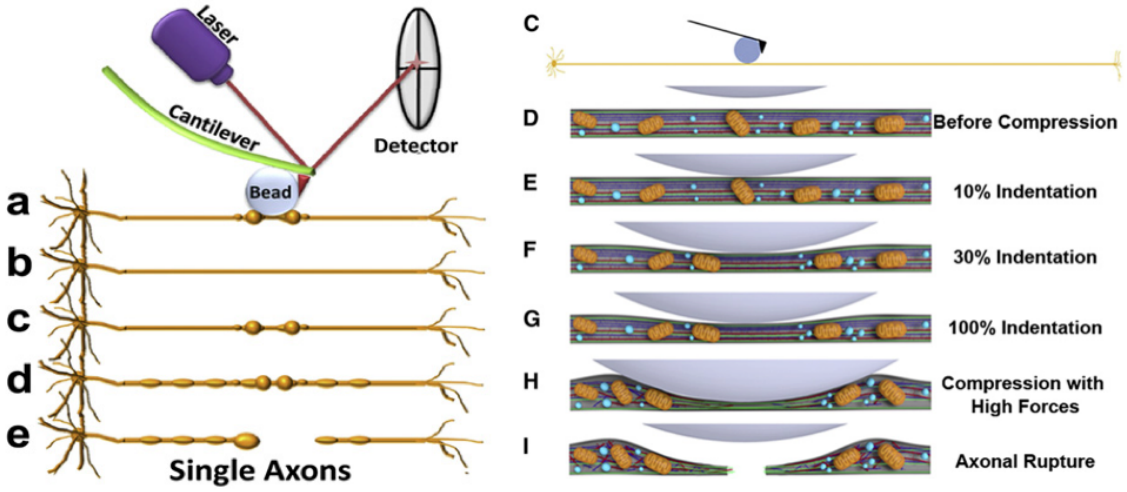

Figure 1.7: TBI experiments *in vitro*: neurons were grown in microfluidic chambers with their axons extended through microgrooves. **a.** The axons were gradually compressed with sub-nanoNewton (nN) forces applied by a bead attached to the tip of the atomic force microscope cantilever. The axonal response to compression depended on the time and force applied and four distinct responses were identified: **b.** axons recovered their original state, **c.** stayed permanently deformed, **d.** entered a degenerative process with increasing formation of FAS, **e.** and finally resulted in axonal rupture. The drawing in the right panel show axonal responses to compression and its effect to mitochondria (orange), tubulin (red), neurofilament (dark blue), actin (green), and vesicles (light blue). Figure from Magdesian et al. [72].

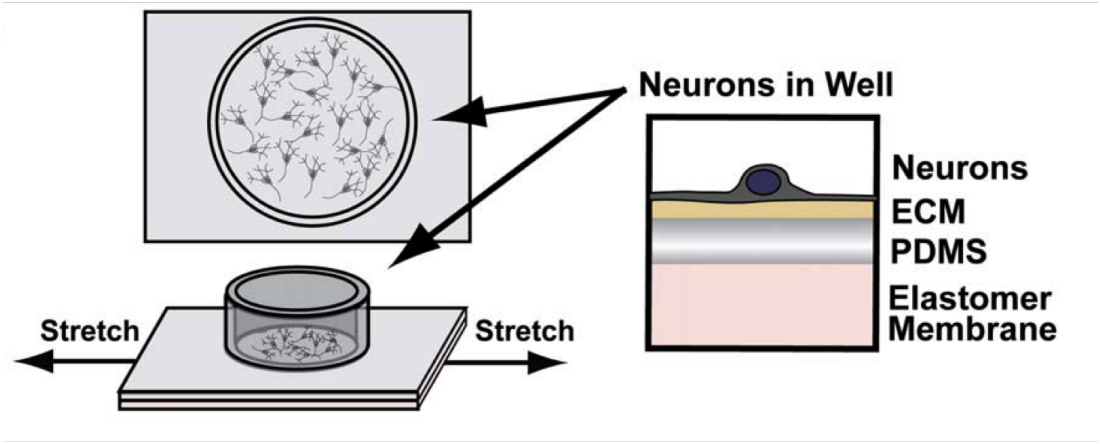

Figure 1.8: TBI experiments *in vitro*: neurons were cultured on elastomer membranes that can be quickly stretched. Magnetic tweezers and coated paramagnetic beads are bound to neurons and transfer injurious forces to the cells. Figure from Hemphill et al. [52].

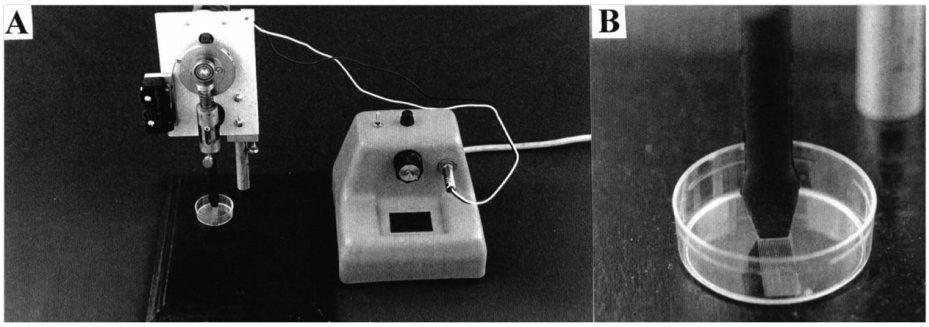

Figure 1.9: TBI experiments *in vitro*: rubber impactor descends upon the tracks, inflicting injury to the neurons. Starting height and descent velocity are controlled by the centrally mounted turn-knob. Figure from Fayaz et al. [35].

1.2.1 Importance of axonal computations

From a signal processing point of view, recent reviews highlight the fact that axons do more than just faithfully transmit spike train encodings from upstream to downstream neurons: they are responsible for important signal and information processing [7, 15, 24, 25]. Thus, it is not coincidental that axonal deformation, regional compactation, swellings, and myelin abnormalities resulting from TBI in humans [68, 87], rodents [97], and swine [14] are directly related to post-traumatic cognitive, physical and psychosocial dysfunctions. In theory, all these geometric structure changes can drastically alter axonal functionality and Action Potential (AP) propagation dynamics.

Axonal injuries induced by *in vitro* techniques were discussed in the previous section. However, recordings of voltage spike trains before and after a FAS have not been performed to date. In this work we want to demonstrate how spike trains can be dramatically reshaped due to changes in the geometry of the axonal core conductor and provide a framework to quantify these changes. Ultimately, our goal is to connect how the observed morphological pathologies in single neurons, which are the fundamental computational building-blocks for all cognition and neurosensory integration, distort the activity of an entire neural population, leading to post-traumatic cognitive and behavioral dysfunction.

1.2.2 FAS in Traumatic Brain Injuries

The severity of TBI may range from mild, where a brief change in mental status or consciousness is observed, to severe, where an extended period of unconsciousness or amnesia can occur in addition to a long-term change of mental status. Despite heterogeneous neuropathological consequences, axonal damage is perhaps the most commonly observed feature across all severities of closed head injury (see Johnson et al. [59] for a recent review). Thus axons provide a clear biophysical marker for evaluating cognitive and behavioral deficits induced by TBI.

Typically, TBI induces widespread axonal damage over spatial regions which include a large number of neurons (10^2-10^6), thus it has been termed diffuse axonal injury (DAI). In extreme cases, axons can be sheared, or disconnected, leading to cell death and more pronounced cognitive and behavioral deficit. This is known as traumatic axonal injury (TAI). But even in mild TBI without notable cell death, injured axons undergo a sequence of changes that culminate in FAS or so-called

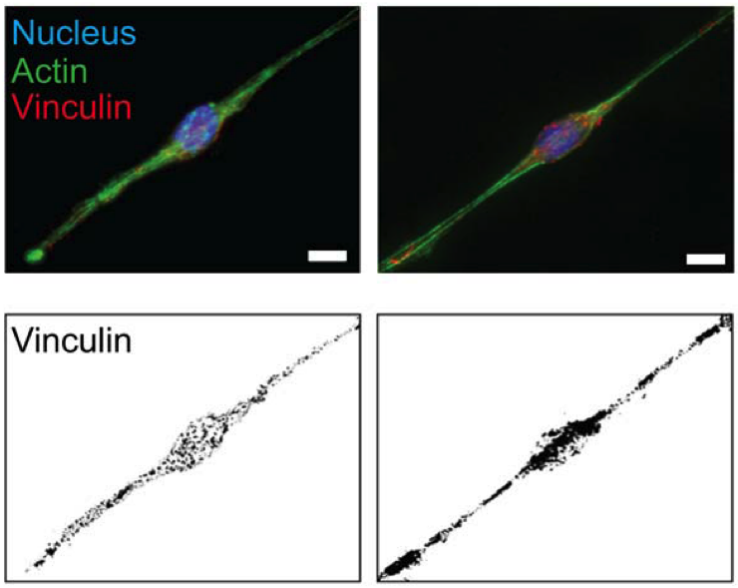

Figure 1.10: Focal Axonal Swelling from *in vitro* experiment of Hemphill et al. [52]. The biochemical markers indicate regions where adhesion of coated beads most likely occurred. Scale bars correspond to 8 and 10 mm.

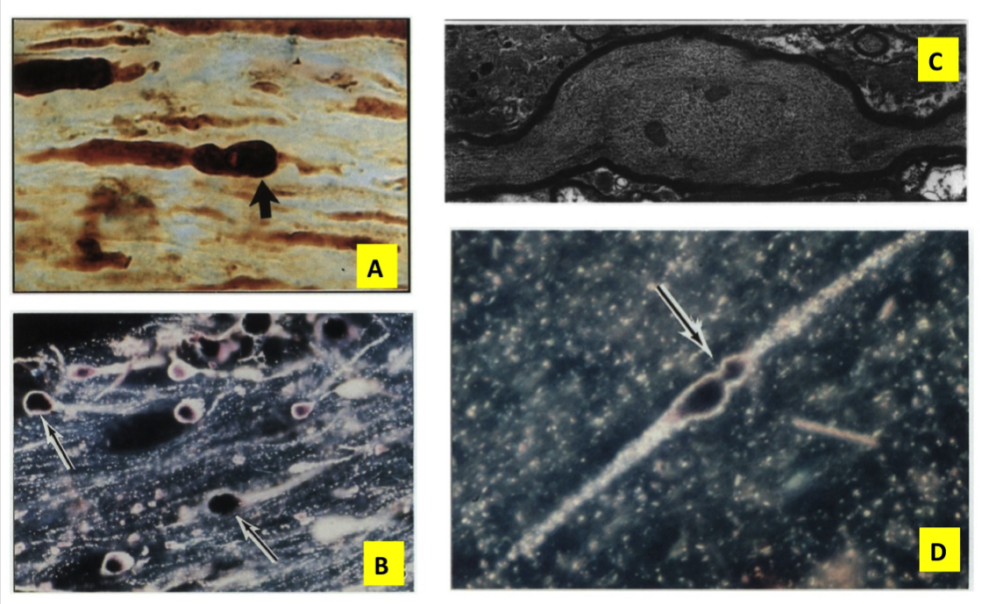

Figure 1.11: Focal Axonal Swellings (FAS) from Maxwell et al. [80]. **a.** Light micrograph illustrates, early after fluid percussion injury, the occurrence of FAS. (magnification $\times$ 1200). **b.** Within several hours of the insult, the axon shows a lobulated swelling, with a site of axonal narrowing. Typically, these lobulated swellings disconnect several hours later. **c.** Longitudinal section of FAS 1h after stretch-injury to the adult guinea-pig optic nerve. The section represents an early stage in the development of the FAS. A relatively low number of membranous organelles occur within the axoplasm. (magnification of $\times$ 9300). **d.** Some FAS form conspicuous proximal bulbs (arrows) as well as less dramatic, detached distal axonal bulbs.

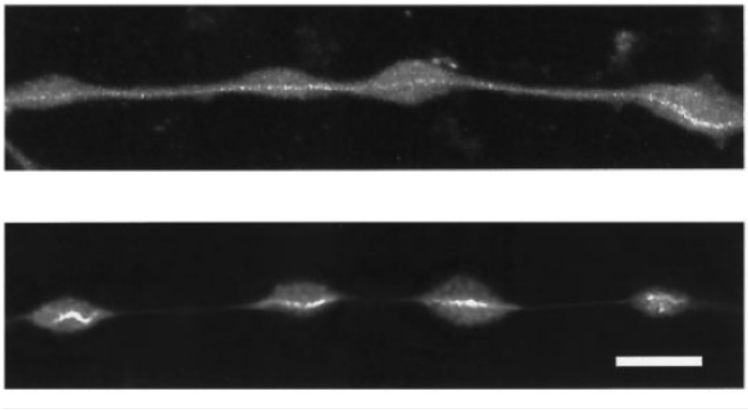

Figure 1.12: Focal Axonal Swellings (FAS) from Smith et al. [105] show human axons 2 hr after dynamic stretch injury. Confocal (top) and deconvolution (bottom) microscopy on properly stained axons reveal a central core of neurofilament in the FAS.

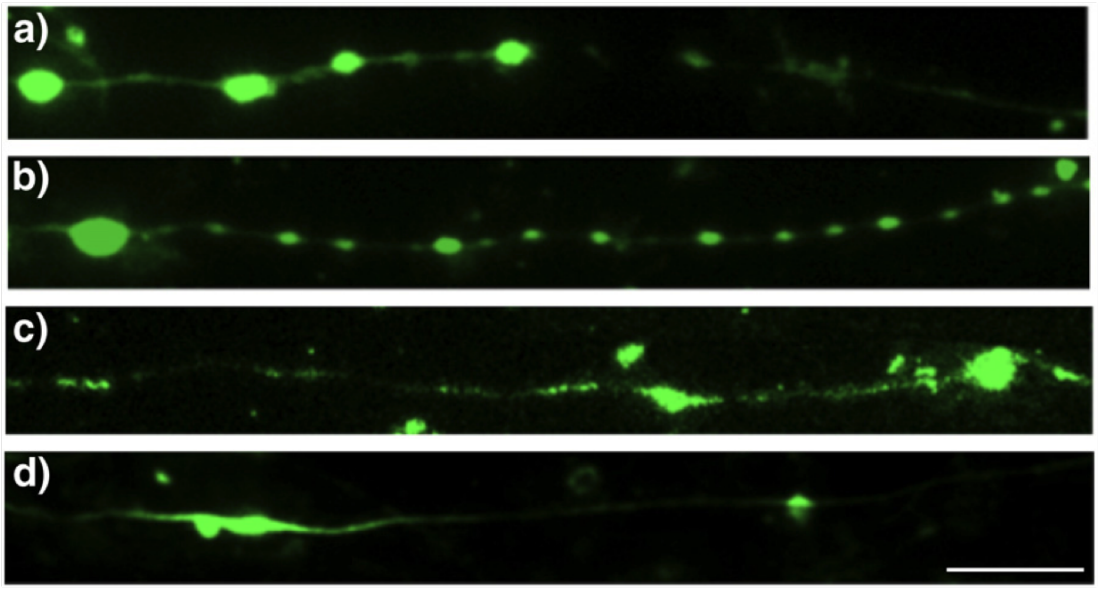

Figure 1.13: Focal Axonal Swellings (FAS) from Tang-Schomer et al. [108]. Immunofluorescent images of axons 3h after dynamic stretch injury. FAS appear along the axonal length like beads on a string. Swellings display accumulations of **a.** tubulin, **b.** the tau protein, **c.** amyloid precursor protein (APP), and **d.** neurofilament (NF200). Scale bar, 10 μm.

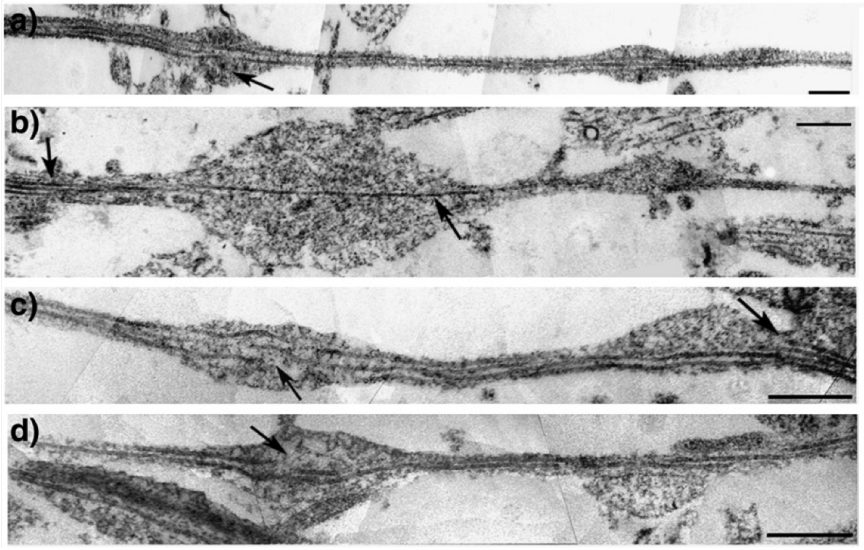

Figure 1.14: Focal Axonal Swellings (FAS) from Tang-Schomer et al. [108]. Transmission electron microscopy images of axons 3h after dynamic stretch injury. Some microtubules break within FAS (arrows) while others traverse the swollen region intact. Scale bars: 500 nm.

varicosities [72, 80, 105, 119]. FAS can lead to a 30-fold increase in axon diameters, potentially interrupting axonal transport [108, 109] and/or significantly impairing the underlying spike train propagation responsible for encoding information in neural activity [74]. FAS typically develops within a period of 2-6 hours after the initial injury in animals, and approximately 12 hours or longer in humans [12, 19, 45, 80]. During this time, information encoded in voltage spikes are potentially delayed, reflected and/or deleted due to the FAS, thus compromising neural computation and functionality. Such time scales for producing morphological changes in the axons have given rise to a hope that pharmacological agents may be introduced into patients to suppress and/or counteract the deleterious effects of FAS [52].

1.2.3 FAS in Multiple Sclerosis

Multiple Sclerosis is a common inflammatory disease of the central nervous system where axon damage is responsible for permanent neurological deficits [50, 111]. It is also the most common cause of neurologic disability in young adults [110].

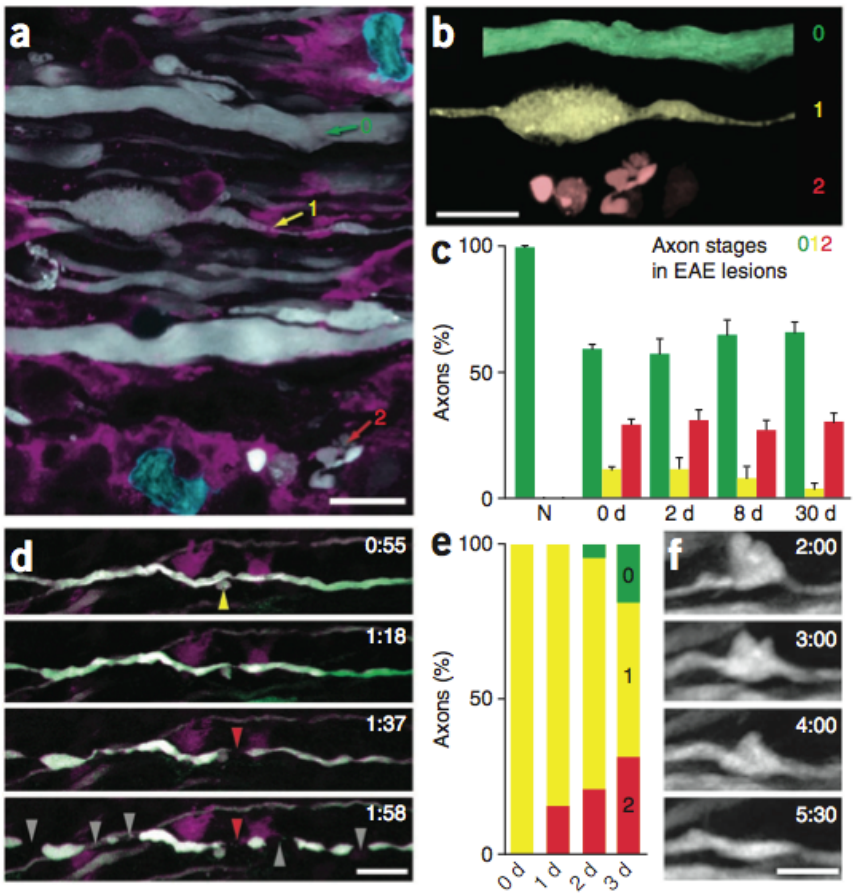

Figure 1.15: FAS in Multiple Sclerosis. In vivo imaging of axonal degeneration in mice. **a.** Axons (white), activated macrophages/microglia (magenta) and T cells (cyan) in an acute spinal encephalomyelitis (EAE) lesion. **b.** Pseudo-colored axons isolated from those shown in **a**: normal appearing (0, green), swollen (1, yellow), and fragmented (2, red). **c.** Frequency of axon stages in normal spinal cord (N) and axons days after EAE lesions. **d.** Time-lapse images of a stage 1 axon (white) in EAE and activated macrophages/microglia (magenta). Time is shown as hour:min; The axon first breaks (red arrowhead) near a small swelling (yellow arrowhead) at a putative node of Ranvier before fragmenting (gray arrowheads). **e.** Fate of stage 1 axons imaged 13 d after the peak of EAE. **f.** Time-lapse images of recovering stage 1 axon (time is as shown in d). Scale bar in a,b, 10 μm; scale bar in d, 25 μm; scale bar in f, 10 μm. Figure from Nikic et al. [86].

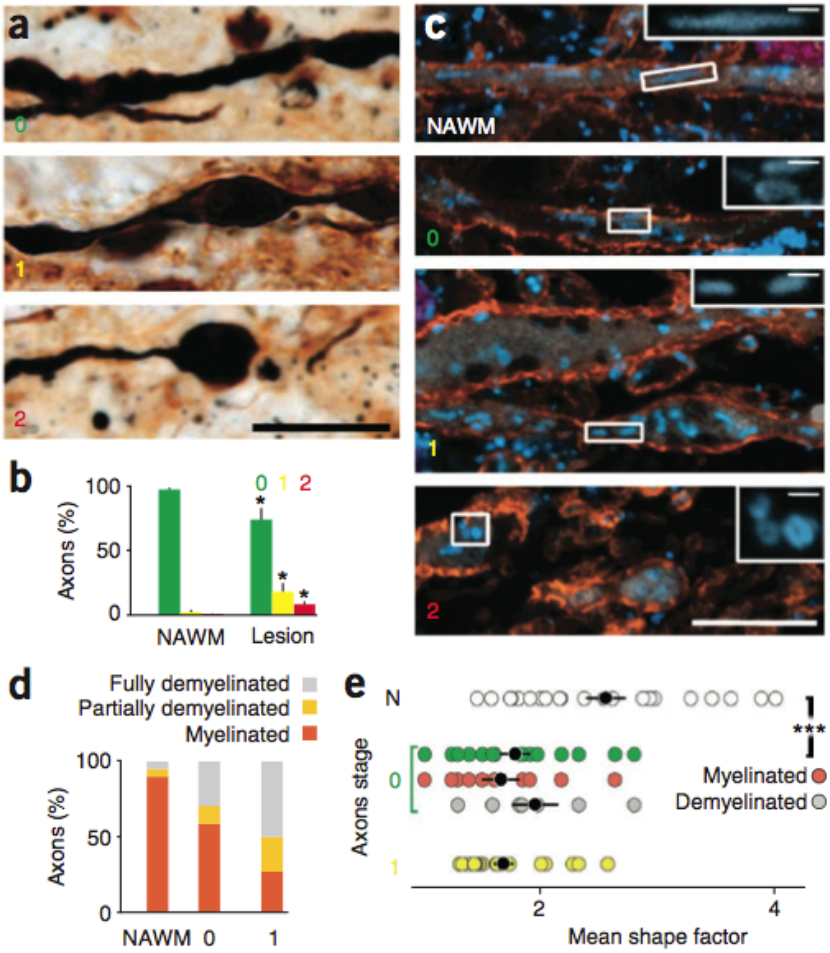

Figure 1.16: FAS in Multiple Sclerosis. Axonal changes in animal model are consistent with human axonal degeneration following multiple sclerosis lesions. **a.** Representative axons in different stages of degeneration in an acute human multiple sclerosis lesion. **b.** Prevalence of axonal degeneration stages in normal-appearing white matter (NAWM) and in acute multiple sclerosis lesions. **c.** Axon (top) located around an active multiple sclerosis lesion, and examples of stage 0,1 and 2 axons located inside the same lesion. **d.** Myelination status of axon in degeneration stages 0 and 1. **e.** Comparison of mean mitochondrial shape factors of axons in NAWM (N), and stage 0 and 1 multiple sclerosis axons. Figure from Nikic et al. [86].

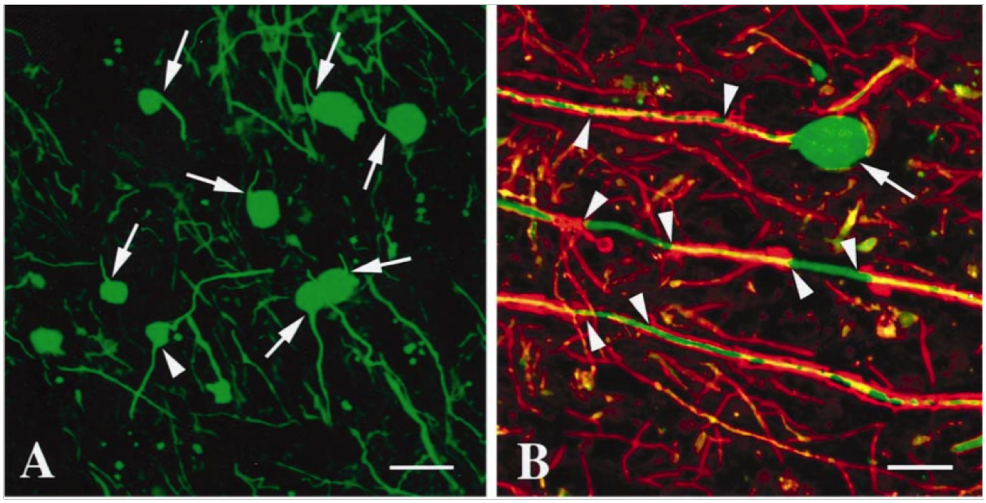

Figure 1.17: FAS in Multiple Sclerosis. Images of axonal changes in Multiple-Sclerosis lesions. Nonphosphorylated neurofilaments are green in all panels. Red indicates myelin. **a.** Centers of active lesions. It shows stacked images of terminal axonal ovoids with single axonal connections (arrows), an axonal ovoid with dual axonal connections (arrowhead), and many normal-appearing axons. **b.** Edges of active lesions. It shows three large axons undergoing active demyelination (arrowheads). One axon ends in a large terminal ovoid (arrow). Figure from Trapp et al. [110].

In the recent work of Nikic et al. ([86]), the authors identified a variant of axon damage in a mouse model of Multiple Sclerosis. The process is characterized by sequential stages, beginning with focal swellings and progressing to axon fragmentation. See Figure 1.15 for details. Notably, most swollen axons persist unchanged for several days, and some recover spontaneously.

The axonal changes in Fig. 1.15 are consistent with focal axonal degeneration detected in acute human multiple sclerosis lesions – depicted in Figure 1.16. Indeed, these results are in accordance with the study of Trapp et al. ([110]), where they analyzed brain tissue obtained at autopsy from human patients with Multiple Sclerosis. Pathological changes in axons were detected in all lesions and confocal microscopy also identified terminal axonal ovoids. See Figure 1.17 for details.

We believe that much of the mathematical modeling of FAS developed throughout this work can be adapted also to Multiple Sclerosis and other neurodegenerative diseases.

1.2.4 FAS in Alzheimer's Disease

Alzheimer disease is the most common type of age-related dementia, affecting approximately 24 million people worldwide, with the number of patients doubling every 20 years as a consequence of the aging population [65]. The disease is characterized by progressive loss of cognitive abilities, severe neurodegeneration, and prominent neuroinflammation.

The studies of Krstic et al. ([65]) revealed that in a healthy aging neuron, a protein extrusion mechanism compensates for failures in protein clearance along the axon. In pathological aging, however, stress-induced amyloid precursor protein accumulates in large swellings (see Figure 1.18). The eventual blockade of axonal transport leads to synaptic destabilization and membrane leakage at FAS.

The formation of abnormal axonal varicosities in mice models for Alzheimer were also reported in Tsai et al. [113]. See Figure 1.19 for details. Thus, FAS also play a role in the pathology of Alzheimer's disease, but the list is not yet complete.

1.2.5 FAS in other neurodegenerative diseases

As reviewed in [20], Focal Axonal Swellings (also termed as axonal dystrophy) are almost universal in neurodegenerative diseases of the central nervous system, as a major pathway to axonal death. In most cases, swellings are associated with progressive accumulation of specific proteins resulting in axonal transport deficits [82].

Other neurological disorders where FAS are also implicated also include Creutzfeldt-Jakob's disease [67], HIV dementia [1] and Parkinsons disease [40]. Parkinson's disease is the second most common neurodegenerative disorder after Alzheimer's disease and affects approximately seven million people globally and one million people in the United States.

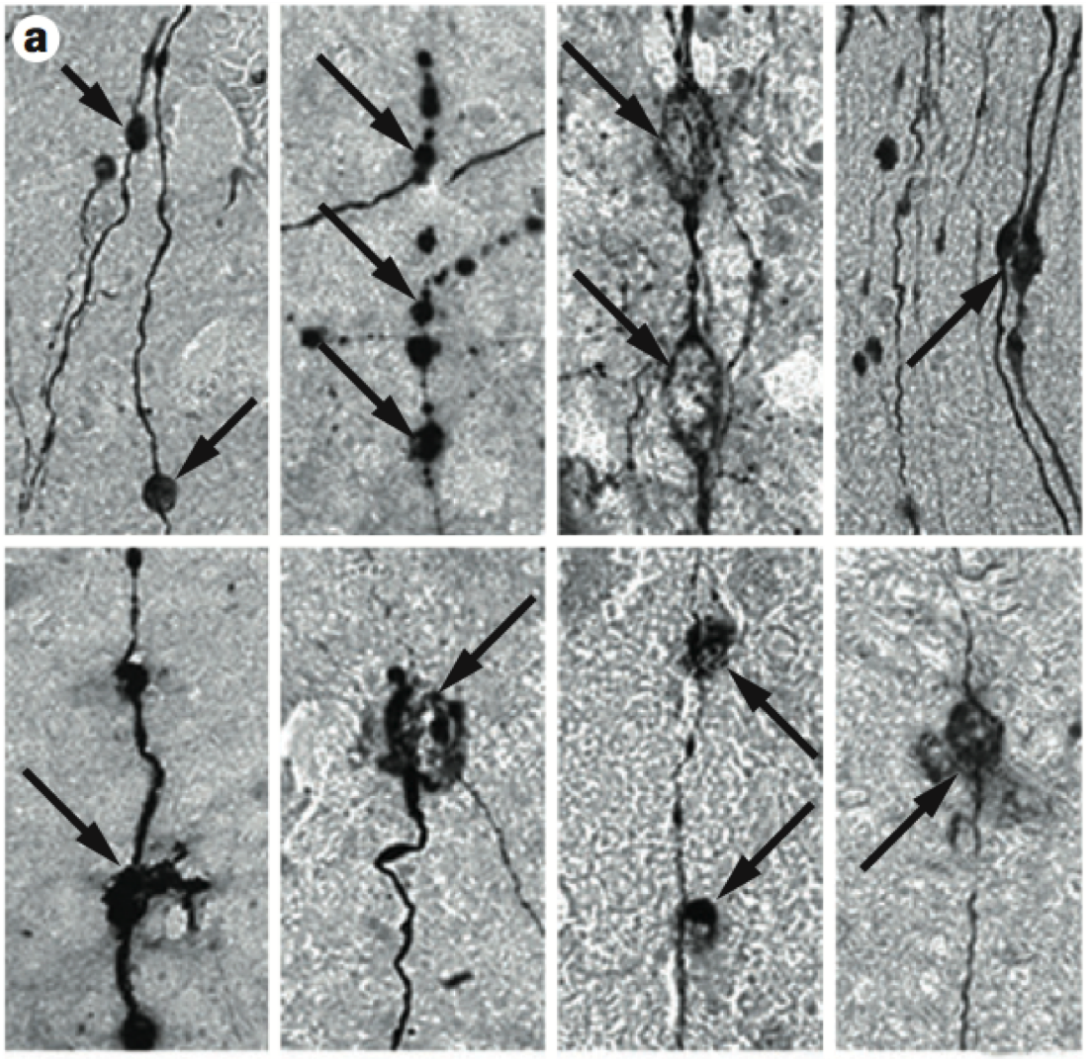

Figure 1.18: FAS in Alzheimer's disease. FAS and leakage are a trigger of senile plaque formation in patients with Alzheimer disease. Experimental support that evolution of senile plaques starts with FAS and varicosities (top row, arrows) and leakage from dystrophic axons (bottom row, arrows) in the cortex. Figure from Krstic et al. [65].

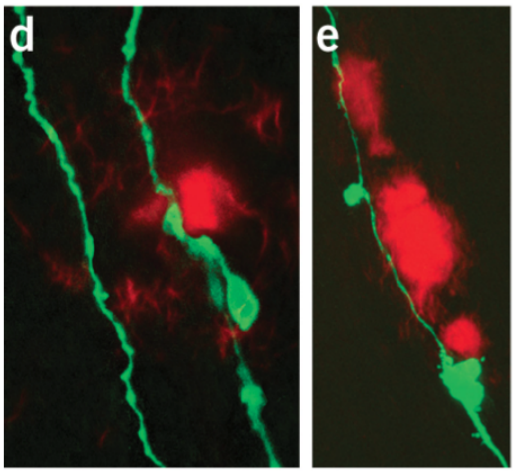

Figure 1.19: FAS in Alzheimer's disease. Formation of abnormal axonal varicosities near fibrillar deposits of transgenic mice model. Individual axons (green) **d.** in the hippocampus and **e.** corpus callosum. Figure from Tsai et al. [113].

Chapter 2

BACKGROUND AND METHODS

In this chapter we review mathematical models of neuronal electrophysiology that generate traveling spikes along the neuron's axon. We derive the active cable equation from basic electrodynamics principles and discuss ionic transmembrane currents. These currents have nonlinear conductances and depend on voltage-gated ion channels, that in turn, can be open or closed depending on the dynamics of their gating variables. We discuss the hallmark model of Hodgkin-Huxley for the squid giant axon and some of it's reductions such as the Morris-Lecar model and the Fitzhugh-Nagumo equations. The interplay of axonal geometrical inhomogeneities with conductance nonlinearities will have a pivotal role in the modeling of FAS. Finally, we introduce a pseudo-spectral algorithm to effectively simulate spike train propagation and review previous numerical and analytical results.

2.1 Neuronal equations

Most of us are familiar with the neuron – an electrically excitable brain cell that processes and transmits information through electrical and chemical signals. Neurons connect to each other via synapses (specialized connections) forming neural networks. A typical neuron has a cell body (soma), dendrites and an axon. At the majority of synapses, signals are sent from the axon of one neuron to a dendrite of another. The propagation of cellular signals was always a central theme in physiology, and the most important landmark in these studies is the work of Alan Hodgkin and Andrew Huxley; they developed the first quantitative model of the propagation of an electrical signal along a squid giant axon and their ideas have since been extended and applied to a wide variety of excitable cells. Because of the central importance of cellular electrical activity in physiology, the importance of the Hodgkin-Huxley model in the study of electrical activity, and because it forms the basis for the study of excitability, it is no exaggeration to say "it is the most important model in

Table 2.1: List of symbols for active cable equations

Symbol	Unit	Description
x	cm	longitudinal spatial coordinate
t	ms	temporal coordinate
$r_{\mathrm{L}}(x)$	$\Omega \cdot \mathrm{cm}$	longitudinal (intracellular) resistivity
$a(x)$	cm	radius of the core conductor
$V(x,t)$	mV	membrane voltage
c_{M}	$\mu\mathrm{F/cm}^2$	specific membrane capacitance
r_{M}	$\Omega \cdot \mathrm{cm}^2$	specific membrane resistance
i_{ion}	$\mu\mathrm{A/cm}^2$	ionic current per unit area of membrane
i_{ext}	$\mu\mathrm{A/cm}^2$	external current per unit area of membrane

all of the physiological literature" [61]. In this chapter we derive the active cable equation for signal propagation and discuss the Hodgkin-Huxley model and some of its reductions. We also highlight the role of axonal geometry in the models, which will be further explored to add the effects of Focal Axonal Swellings arising in traumatic brain injuries, concussions and neurodegenerative diseases.

2.1.1 Cable theory

All neurons are electrically excitable and maintain voltage gradients across their membranes. It is possible to derive equations for the membrane (voltage) potential along a cable expressed as a function of a single spatial coordinate x and time t. The basic problem is to solve for the potential $V(x,t)$. In this subsection we transcribe the derivation of the *active cable equation* from Dayan and Abbot ([22]), that follows from basic electrodynamical principles: Ohm's Law, Kirchoff's Law, conservation and continuity of current.

> Current flows within a neuron due to voltage gradients. The longitudinal resistance of a cable segment of length $\triangle x$ and radius a is given by multiplying the intracellular resistivity r_L by $\triangle x$ and dividing by the cross-sectional area, πa^2, so that
>
> $$R_L = \frac{r_L \triangle x}{\pi a^2}. \tag{2.1}$$

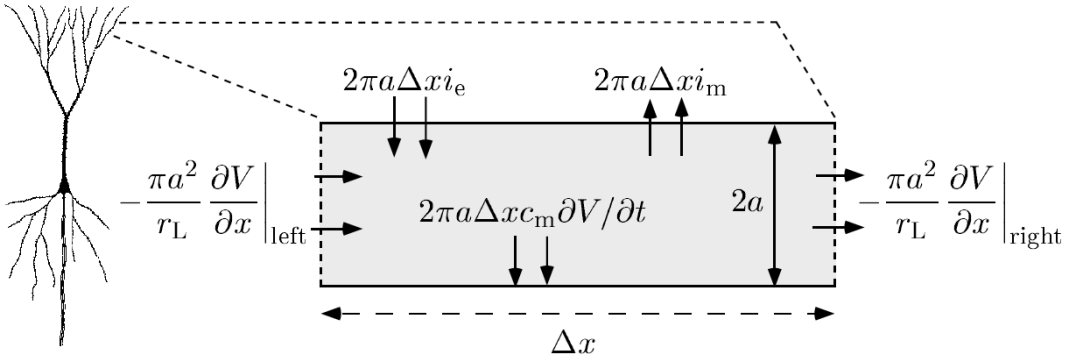

Figure 2.1: The segment of neuron used in the derivation of the cable equation. The longitudinal, membrane, and electrode currents that determine the rate of change of the membrane potential within this segment are denoted. The segment has length $\triangle x$ and radius a. The expression involving the specific membrane capacitances refers to the rate at which charge builds up on the cell membrane, generating changes in the membrane potential. Figure from Dayan and Abbot [22].

The voltage drop across this length of cable, $\triangle V = V(x+\triangle x) - V(x)$, is then related to the amount of longitudinal current flow by Ohm's law. We define currents flowing in the direction of increasing x as positive. By this convention, the relationship between $\triangle V$ and I_L is given by

$$\begin{aligned} \triangle V &= -R_L \cdot I_L, \\ \triangle V &= -\frac{r_L \triangle x I_L}{\pi a^2}. \end{aligned} \tag{2.2}$$

Solving this for the longitudinal current, we find

$$I_L = -\frac{\pi a^2}{r_L} \cdot \frac{\triangle V}{\triangle x}. \tag{2.3}$$

It is useful to take the limit of this expression for infinitesimally short cable segments, that is $\triangle x \to 0$. In this limit, the ratio of $\triangle V$ to $\triangle x$ becomes the derivative $\partial V/\partial x$. We use a partial derivative here because V also depend on time. Thus, at any point along a cable of radius a and intracellular resistivity r_L, the longitudinal current flowing in the direction of increasing x is

$$I_L = -\frac{\pi a^2}{r_L} \cdot \frac{\partial V}{\partial x}. \tag{2.4}$$

The membrane potential $V(x,t)$ is determined by solving a partial differential equation, the cable equation, that describes how the currents entering, leaving and flowing within a neuron

affect the rate of change of the membrane potential. To derive the cable equation, we consider the currents within the small segment shown in Fig. 2.1. This segment has a radius a and a short $\triangle x$. The rate of change of the membrane potential due to currents flowing into and out of this region is determined by its capacitance. The capacitance of a membrane in determined by multiplying the specific membrane capacitance c_m by the area of the membrane. The cylinder of membrane show in Fig. 2.1 has a surface area of $2\pi a \triangle x c_m$. Thus

$$\text{current needed to charge all the membrane} = 2\pi \triangle x c_m \frac{\partial V}{\partial t}. \tag{2.5}$$

All the currents that can change the membrane potential of the segment are shown in Fig. 2.1. Current can flow longitudinally into the segment from neighboring segments (specified earlier). Current can flow across the membrane segment through ion and synaptic receptor channels, or through an electrode. The contribution from ion and synaptic channels is expressed as a current per unit area of membrane i_{ion} times the surface area of the segment, $2\pi a \triangle x$. The electrode is not normally expressed as a current per unit area, but it is convenient for now to define

$$i_{ext} = \frac{\text{total electrode current flowing}}{\text{surface area of that region}}. \tag{2.6}$$

The cable equation is derived by setting

$$\text{current needed to charge all the membrane} = \text{sum all currents}$$

The total longitudinal current entering the cylinder is the difference between the current flowing in (on the left) and that flowing out (on the right). Thus

$$2\pi a \triangle x c_m \frac{\partial V}{\partial t} = -\left(\frac{\pi a^2}{r_L}\frac{\partial V}{\partial x}\right)\Big|_{\text{left}} + \left(\frac{\pi a^2}{r_L}\frac{\partial V}{\partial x}\right)\Big|_{right} - 2\pi a \triangle x (i_{ion} - i_{ext}). \tag{2.7}$$

If we now:

1. Divide both sides of this equation by $2\pi a \triangle x$.
2. Note that

$$\frac{1}{\triangle x}\left[\left(\frac{\pi a^2}{r_L}\frac{\partial V}{\partial x}\right)\Big|_{right} - \left(\frac{\pi a^2}{r_L}\frac{\partial V}{\partial x}\right)\Big|_{\text{left}}\right] \rightarrow \frac{\partial}{\partial x}\left(\frac{\pi a^2}{r_L}\frac{\partial V}{\partial x}\right), \tag{2.8}$$

   where the arrow refers to the limit $\triangle x \rightarrow 0$.

3. Rearrange terms conveniently,

we obtain the active cable equation,

$$c_{\text{m}}\frac{\partial V}{\partial t} = \frac{1}{2a(x)}\frac{\partial}{\partial x}\left(\frac{a^2(x)}{r_{\text{L}}(x)}\frac{\partial V}{\partial x}\right) - i_{\text{ion}} + i_{\text{ext}}. \tag{2.9}$$

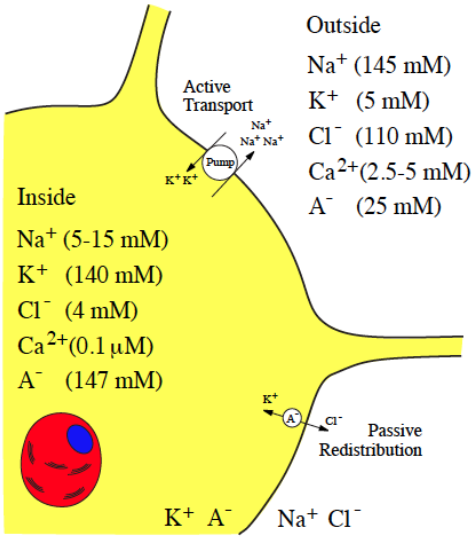

Equilibrium Potentials

$$\begin{aligned}
\mathrm{Na}^+ \quad & 62 \log \tfrac{145}{5} = 90 \text{ mV} \\
& 62 \log \tfrac{145}{15} = 61 \text{ mV} \\
\mathrm{K}^+ \quad & 62 \log \tfrac{5}{140} = -90 \text{ mV} \\
\mathrm{Cl}^- \quad & -62 \log \tfrac{110}{4} = -89 \text{ mV} \\
\mathrm{Ca}^{2+} \quad & 31 \log \tfrac{2.5}{10^{-4}} = 136 \text{ mV} \\
& 31 \log \tfrac{5}{10^{-4}} = 146 \text{ mV}
\end{aligned}$$

Figure 2.2: Ion concentration and Nernst equilibrium potentials in a typical mammalian neuron. A^- are membrane impermeant anions. Temperature $T = 37^o$ C. Figure from Izhikevich [57]

Notice that the term $a^2(x)$ inside the differential operator can only cancel the term $a(x)$ outside the operator if $a(x) = a =$ constant. When r_L is also constant, the equation can be simplified to

$$c_{\mathrm{m}} V_t = \lambda^2 V_{xx} - i_{\mathrm{ion}} + i_{\mathrm{ext}}, \tag{2.10}$$

where $\lambda = \sqrt{a/2r_L}$ is known as the electronic length. To determine the membrane potential, the equation above must be augmented by appropriate boundary conditions and the ionic currents i_{ion} must be specified. If i_{ion} is linear, the equation is referred as *passive* cable equation and analytical solutions can be obtained in terms of Green functions (see [114]). What makes this work mathematically rich is that we have to consider both the *axonal inhomogeneity* (to model focal axonal swellings) and *nonlinear* ionic currents i_{ion}. It is precisely the interplay between these terms that will produce non-trivial effects in spike propagation.

2.1.2 Ionic currents and equivalent circuit

As explained in [57], the ionic current i_{ion} present in neuron membranes is typically a combination of transmembrane currents involving sodium (Na^+), potassium (K^+), calcium (Ca^{2+}) or chloride

(Cl^-) ions. Figure 2.2 depicts differences in the concentration of these ions inside and outside the cell. Such disparities result in electrochemical gradients with two forces driving each ion species:

- *Diffusion*: ionic species exit higher concentrations to lower ones.
- *Coulomb's law*: ionic species charged with same/opposite signs repel/attract each other.

For example, K^+ diffuse out of the cell because the concentration inside is higher than the concentration outside. These ions however, are attracted to the negatively charged interior and repelled from the positively charged exterior of the membrane. At some point the equilibrium E_K is achieved and can be calculated by the Nernst equation (see [57]):

$$E_{ion} = \frac{RT}{zF} \log_{10} \frac{[ion]_{out}}{[ion]_{in}} \tag{2.11}$$

where $[ion]_{in}$ and $[ion]_{out}$ are concentrations of the ions inside and outside the cell, respectively; R is the universal gas constant; T is temperature in degrees Kelvin; F is Faradays constant , z is the valence of the ion ($z = 1$ for Na^+ and K^+; $z = -1$ for Cl^-; and $z = 2$ for Ca^{2+}). Substituting the numbers and using body temperature $T = 310K$ results in

$$E_{ion} \approx 62 \cdot \log_{10} \frac{[ion]_{out}}{[ion]_{in}} \ \ (mV), \tag{2.12}$$

for monovalent (z = 1) ions. The Nernst equilibrium for E_K, E_{Na}, E_{Ca}, E_K, and E_{Cl} for typical mammalian neurons are summarized in Fig. 2.2.

It is also traditional to represent electrical properties of membranes in terms of equivalent circuits similar to the one depicted in Fig 2.3. The term i_{ion} in equation (2.9) typically has the form

$$i_{ion} = I_{Na} + I_{Ca} + I_K + I_{Cl}, \tag{2.13}$$

with

$$\begin{aligned} I_K &= g_K(V, \text{other variables}, t) \cdot (V - E_K), \\ I_{Na} &= g_{Na}(V, \text{other variables}, t) \cdot (V - E_{Na}), \\ I_{Ca} &= g_{Ca}(V, \text{other variables}, t) \cdot (V - E_{Ca}), \\ I_{Cl} &= g_{Cl}(V, \text{other variables}, t) \cdot (V - E_{Cl}), \end{aligned} \tag{2.14}$$

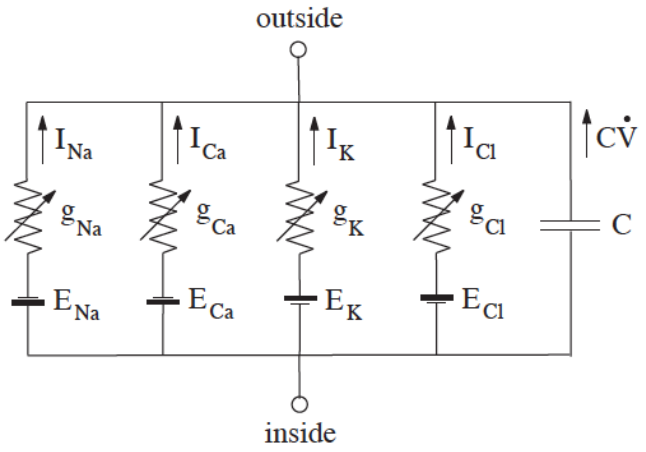

Figure 2.3: Equivalent circuit representation of a patch of cell membrane. Figure from Izhikevich [57].

If the conductance terms, g_K, g_{Na}, g_{Ca}, and g_{Cl}, are constant, the currents are said to be Ohmic. In general, they are not, since they depend on the membrane potential V, channel gating-variables, pharmacological agents, and time. It is precisely the time-dependent variation in conductances that allows a neuron to generate an action potential, or spike.

2.1.3 Conductances and voltage-gated channels

The conductance terms g_K, g_{Na}, g_{Ca} and g_{Cl} depend on their corresponding voltage-gated transmembrane channels. Figure 2.4 illustrates the lipid bilayer in the cell membrane and a K^+ channel which allows current to flow. As explained in [30], a channel is basically a pore with dynamic gates that can be either open or closed. The (global) state of the channel depend on the combined states of these *subunits*.

In the hallmark framework of Hodgkin and Huxley (HH), the K^+ channel is modeled with four independent identical subunits, given by the symbol n, that must all be in an open state for the channel to be in the conducting state. The Na^+ channel is active if three subunits of type m and one subunit of type h are simultaneously open, Ca^{+2} channels are neglected and the Cl^- conductance is

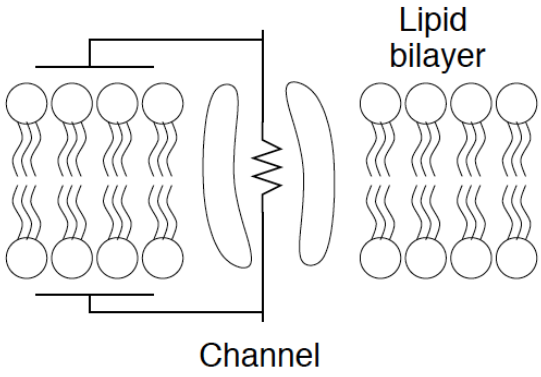

Figure 2.4: Cartoon of the cell membrane showing the insulating lipid bilayer and a K^+ channel which allows current to flow. Figure from Ermentrout and Terman [30].

a simple linear term:

$$\begin{aligned} g_{\mathrm{K}} &= \tilde{g}_{\mathrm{K}} \cdot n^4 \\ g_{\mathrm{Na}} &= \tilde{g}_{\mathrm{Na}} \cdot m^3 \cdot h \\ g_{\mathrm{Cl}} &= \tilde{g}_{\mathrm{Cl}}, \end{aligned} \tag{2.15}$$

where $\tilde{g}_{\mathrm{K}}$, $\tilde{g}_{\mathrm{Na}}$, and $\tilde{g}_{\mathrm{Cl}}$ are the maximal conductances. The dynamics of a subunit (in the simplest scenario) can be described by a two-state process:

$$\text{Closed} \underset{\beta(V)}{\overset{\alpha(V)}{\rightleftarrows}} \text{Open} \tag{2.16}$$

The rates α and β depend on V because the channels are voltage-dependent. We can write a kinetic equation for the average fraction of subunits in the open state x:

$$\dot{x} = \alpha \cdot (1-x) - \beta \cdot x \quad \text{where} \quad x = n, m, h. \tag{2.17}$$

The classical HH differential equations (without spatial propagation) are given by

$$c_m \dot{V} = -\underbrace{\tilde{g}_{\mathrm{Na}} m^3 h (V - E_{\mathrm{Na}})}_{I_{\mathrm{Na}}} - \underbrace{\tilde{g}_{\mathrm{K}} n^4 (V - E_{\mathrm{K}})}_{I_{\mathrm{K}}} - \underbrace{\tilde{g}_{\mathrm{Cl}} (V - E_{\mathrm{Cl}})}_{I_{\mathrm{Cl}}} + i_{\mathrm{ext}} \tag{2.18}$$

$$\dot{x} = \alpha_x (1-x) - \beta_x \quad \text{where} \quad x = n, m, h. \tag{2.19}$$

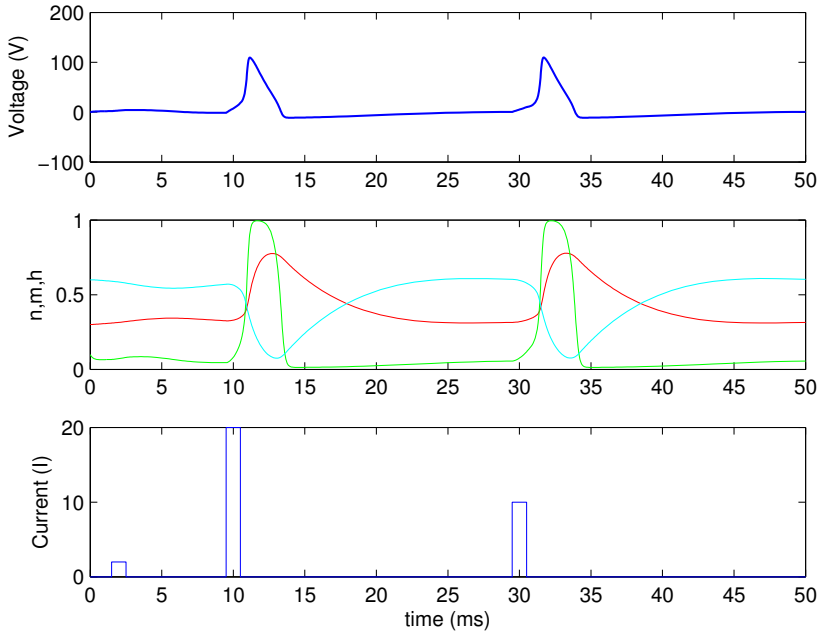

Figure 2.5: Simulating Hodgkin-Huxley differential equations. The system is originally at rest and will produce a spike if stimulated by a sufficiently strong external current.

To match the data recorded from a squid giant axon, Hodgkin and Huxley chose the following parameters and gating functions: $\tilde{g}_{\rm Na} = 120$ mS/cm^3, $\tilde{g}_{\rm K} = 36$ mS/cm^3, $\tilde{g}_{\rm Cl} = 0.3$ mS/cm^3, $E_{\rm Na} = 50$ mV, $E_{\rm K} = -77$ mV, $E_{\rm Cl} = -54.4$ mV, and

$$\begin{aligned}
\alpha_n(V) &= 0.01(V+55)/(1-\exp(-(V+55)/10)) \\
\beta_n(V) &= 0.125\exp(-(V+65)/80)) \\
\alpha_m(V) &= 0.1(V+40)/(1-\exp(-(V+40)/10)) \\
\beta_m(V) &= 4\exp(-(V+65)/18) \\
\alpha_h(V) &= 0.07\exp(-(V+65)/20)) \\
\beta_h(V) &= 1/(1+\exp(-(V+35)/10). \qquad (2.20)
\end{aligned}$$

It is common to rewrite eq (2.17) in terms of steady state functions (x_∞) and time scales (τ_x), i,e:

$$\dot{x} = \frac{x_\infty(V) - x}{\tau_x(V)} \text{ where } x_\infty = \frac{\alpha}{\alpha+\beta} \text{ and } \tau_x = \frac{1}{\alpha+\beta} \text{ for } x = n,m,h. \qquad (2.21)$$

As explained in [57], the different variables (m,n,h) have different time scales; Since τ_m is relatively small, the variable m is relatively fast. Fast activation of Na^+ conductance drives V towards $E_{\rm Na}$, resulting in the upstroke of V. Since τ_n and τ_h are large, the recovery variables n and h are slow and will eventually cause V to go below V_{rest} toward $E_{\rm K}$. See Figure 2.6.

An important property of the system is that the Na^+ current continues to be inactivated (h is small) and is not available for any regenerative functions. Thus, the Hodgkin-Huxley system cannot generate another action potential during this *absolute refractory* period. One of the central results of this work is that focal axonal swellings might delete spikes too close to each other increasing the effective refractory period of the system.

A zoo of ion channels: The equations of Hodgkin and Huxley (2.18)-(2.19) provide a good description of the electrophysiological properties of the giant axon of the squid. But as explained in [41], cortical neurons in vertebrates exhibit a much richer repertoire of electrophysiological properties mostly due to a large variety of different ion channels. Some of these other currents are:

- $I_{\rm NaP}$ – Persistent sodium current.
- $I_{\rm A}$ – Rapidly inactivating potassium current.

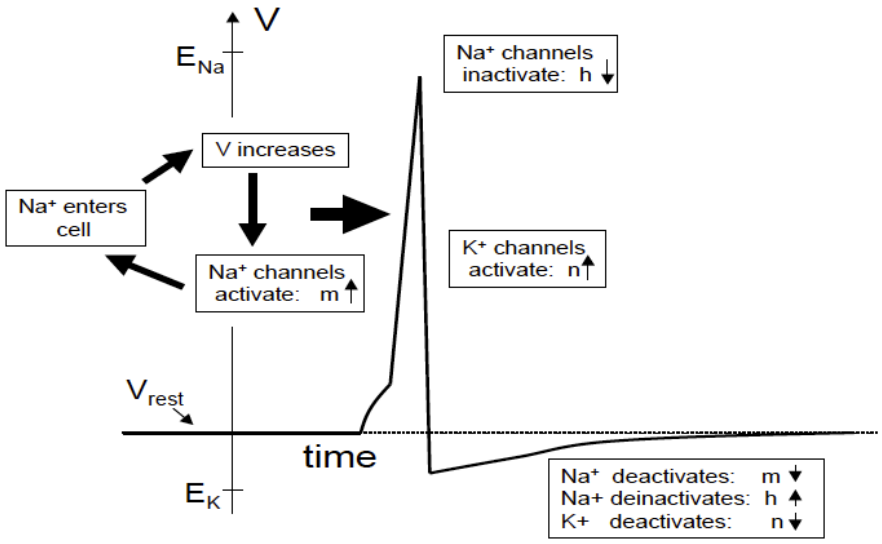

Figure 2.6: The action potential. During the upstroke, sodium channels open and the membrane potential approaches the sodium Nernst potential. During the downstroke, sodium channels are closed, potassium channels are open and the membrane potential approaches the potassium Nernst potential. Figure from Ermentrout and Terman [30].

- I_{L} – High-threshold calcium current.

- I_{T} – Low-threshold calcium current

Neuron models can be very sophisticated biophysically [53, 57] and for detailed simulations one should consider specialized softwares such as NEURON [17, 54]. But instead of adding more details to the HH model, we head in the opposite direction; We will reduce and simplify it, leaving only the most essential features.

2.1.4 Model reductions

The behavior of high-dimensional nonlinear differential equations is hard to analyze. Here we outline the reduction of the Hodgkin-Huxley model to a two-dimensional system that can be studied by means of phase plane analysis. These ideas can be applied analogously to reduce the order of detailed neuron models with a zoo of ion channels.

The first remark is that the dynamics of the gating variable m is much faster than that of the variables. We can do a *quasi steady-state approximation* and replace $m(t)$ by $m_\infty(t)$. The second remark is that $n(t)$ and $h(t)$ are roughly mirror images of each other (see Figure 2.5) , i.e., we may approximate the two variables n and $(1-h)$ by a single effective variable w. Using $(b-h) \approx an$ with some constants a, b and setting $w = b-h = an$, equation (2.18) becomes

$$c_m \dot{V} = -\tilde{g}_{\mathrm{Na}} \big[m_\infty(V)\big]^3 (b-w)(V-E_{\mathrm{Na}}) - \tilde{g}_{\mathrm{K}} \left[\frac{w}{a}\right]^4 (V-E_{\mathrm{K}}) - \tilde{g}_{\mathrm{Cl}}(V-E_{\mathrm{Cl}}) + i_{\mathrm{ext}}, \tag{2.22}$$

or

$$\frac{dV}{dt} = \frac{1}{\tau}[F(V,w) + r \cdot i_{\mathrm{ext}}] \tag{2.23}$$

with $r = 1/\tilde{g}_{\mathrm{Cl}}$, $\tau = r \cdot c_m$ and some function F. Regarding the equations for the auxiliary variable, the m equation disappeared and the others are combined in the variable w, leaving us with a single effective equation

$$\frac{dw}{dt} = \frac{1}{\tau_w} G(V,w), \tag{2.24}$$

where τ_w is a parameter and G a function to be specified. Details of this reduction can be found in [41]. We will review two important reduced models of the form (2.23)-(2.24).

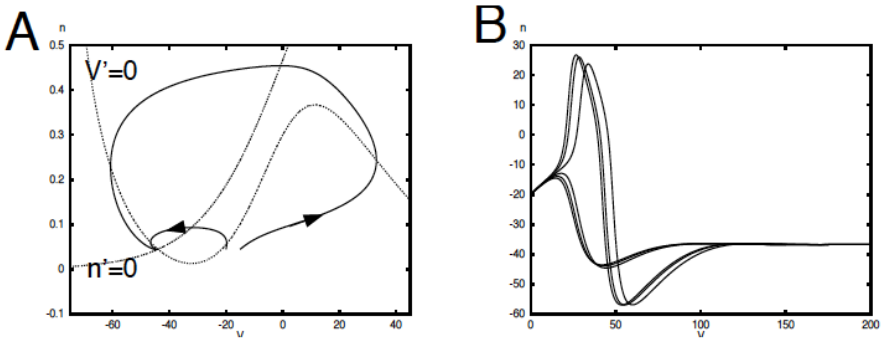

Figure 2.7: (A) Trajectories and nullclines for the Morris-Lecar model. (B) Voltage profile. A small perturbation in voltage from the resting state decays back to rest, while a sufficiently large perturbation in voltage continues to increase and generates an action potential. Figure from Ermentrout and Terman [30].

Morris-Lecar: One of the simplest models for the production of action potentials is a model proposed by Kathleen Morris and Harold Lecar. The model has three channels: a potassium channel, a leak, and a calcium channel. In the simplest version of the model, the equations take the form.

$$\begin{aligned} c_m \frac{dV}{dt} &= -\tilde{g}_{\mathrm{Cl}}(V-E_{\mathrm{Cl}}) - \tilde{g}_{\mathrm{K}} n (V-E_{\mathrm{K}}) - \tilde{g}_{\mathrm{Ca}} m_\infty(V)(V-E_{\mathrm{Ca}}) + i_{ext} \\ \frac{dn}{dt} &= (n_\infty(V)-n)/\tau_n(V), \end{aligned} \tag{2.25}$$

where

$$\begin{aligned} m_\infty &= \frac{1}{2}[1+\tanh((V-V_1)/V_2)] \\ n_\infty &= \frac{1}{2}[1+\tanh((V-V_3)/V_4)] \\ \tau_n &= 1/\cosh((V-V_3)/(2V_4)) \end{aligned} \tag{2.26}$$

Here, V_1, V_2, V_3, V_4 are parameters chosen to fit voltage clamp data. The system is excitable, and as Figure 2.7 demonstrates, a small perturbation in voltage from the resting state decays back to rest, while a sufficiently large perturbation in voltage continues to increase and generates an action potential. Phase plane analysis is very useful in understanding what separates the firing of an action potential from the subthreshold return to rest in this model. See [30, 57] for complete discussions.

FitzHugh-Nagumo: In 1961, after reducing the Hodgkin-Huxley equations, Dick Fitzhugh noticed that the V-nullcline has a cubic shape, while the recovery-nullcline is a monotonic increasing function of the voltage. He developed then a simplified model which captures the essence of these excitable models and became of pivotal importance in the literature (particularly, the mathematical literature). The equations have the form:

$$\begin{aligned} \frac{dV}{dt} &= V(V-a)(1-V)-w+i_{ext} \\ \frac{dw}{dt} &= \varepsilon(V-\gamma w), \end{aligned} \tag{2.27}$$

where $0<a<1$, $\varepsilon>0$ and $\gamma\geq 0$. See [57] for a complete study of the model.

The Fitzhugh-Nagumo equations has been used to model many physiological systems from nerve to heart to muscle and is a favorite model for the study of excitability (see [61]). In most applications, ε is small so that the recovery variable is much slower than the voltage. The *spatial* version of this model will be a favorite model for this work as well.

2.1.5 Interplay between inhomogeneities and nonlinearities

In subsections 2.1.1–2.1.4 we explained that the membrane voltage potential $V(x,t)$ interacts with different species of gating variables w_j. We can now better appreciate the mathematical richness of this system of nonlinear partial differential equations that incorporates (a) the geometry of the core conductor, (b) specific cell properties and (c) multiple active voltage-gated ion channels:

$$\begin{aligned} c_{\mathrm{m}}\frac{\partial V}{\partial t} &= \underbrace{\frac{1}{2a(x)}\frac{\partial}{\partial x}\left(\frac{a^2(x)}{r_{\mathrm{L}}(x)}\frac{\partial V}{\partial x}\right)}_{\text{geometrical inhomogeneity}} - \underbrace{i_{\mathrm{ion}}(V,w_j)}_{\text{nonlinearities}} + i_{\mathrm{ext}}(x,t) \\ \frac{\partial w_j}{\partial t} &= \underbrace{f_j(V,w_j)}_{\text{varying timescales}} \quad ,\text{for } \; j=1,\cdots,N. \end{aligned} \tag{2.28}$$

While nonlinear conductances are responsible for the excitable properties of the membrane, the gating variables have prescribed dynamic equations of their own. In a recent review (for neurobiologists!), Bucher and Goaillard [15] made the following remarks:

> "The findings discussed here clearly show that many axons do not faithfully propagate spikes. Nonlinearities resulting from the gating properties of ion channels and geometric inhomogeneities, as well as neuromodulation, may alter activity patterns between initiation and arrival at presynaptic sites". Bucher et al ([15]).

We underlined most of the above mentioned terms in Eq. (2.28). Moreover:

> " Curiously, reports of activity-dependent changes in conduction velocity and impulse failures have appeared over the better part of the 20th century, and some of the potential functional implications have been insightfully discussed more than 30 years ago. " Bucher et al ([15]).

We will review many of these results in the next sections, since they introduced a wide array of analytical and numerical methods for the study of signal propagation in axons. Finally, they point that

> " despite this long-standing knowledge, the understanding that axons act as conditional rather than faithful conduits of information is only now entering the common consciousness of cellular neuroscientists. This may have to do with the fact that the relevance for neural coding and processing is far from understood. In most cases, we do not even know the magnitude of changes in spike conduction in the context of biologically relevant patterns of activity. " Bucher et al ([15]).

The interplay between geometrical inhomogeneities and nonlinearities becomes of central importance in the studies of Traumatic Brain Injuries and neurogeneration since Focal Axonal Swellings (implicated in all these pathologies) can be 30 times larger than the normal axonal cable. We will discuss and implement numerical methods for Equation (2.28) to gain insight about how FAS degrade the information contained in spike trains.

2.2 Methods

We can compute numerical solutions to neuronal equations in a wide variety of ways. Higher-order finite difference methods are the core of the compartmental modeling performed by software packages such as AXONTREE [75] [76], SPICE [118], GENESIS [10] and NEURON [17, 54]. Boundary value problem methods [83] and Finite Element Methods [2, 121] can also be employed in the study of neuronal dynamics.

Here, we use a pseudo-spectral technique [66, 112] due to the accuracy of the spectral representation (beyond all orders accuracy) and the speed of the underlying Fast Fourier Transform algorithm (FFT). The techniques produces highly-accurate and rapid solutions. However, any of the other techniques mentioned above can also be implemented to generate the results presented here.

2.2.1 *Pseudo-Spectral algorithm:*

To outline the algorithm, define: the vector of variables $\mathbf{u}$ and the linear operator L by

$$\mathbf{u} = \begin{bmatrix} V \\ w_1 \\ \vdots \\ w_N \end{bmatrix}, \quad L(\mathbf{u}) = \begin{bmatrix} \frac{c_m^{-1}}{2a(x)} \frac{\partial}{\partial x} \left(\frac{a^2(x)}{r_{\mathrm{L}}(x)} \frac{\partial \mathbf{u}_1}{\partial x} \right) \\ 0 \\ \vdots \\ 0 \end{bmatrix},$$

the nonlinear operator N and the external forcing $\mathbf{F}(x,t)$ by

$$N(\mathbf{u}) = \begin{bmatrix} -i_{\mathrm{ion}}(\mathbf{u})/c_m \\ f_1(\mathbf{u}) \\ \vdots \\ f_N(\mathbf{u}) \end{bmatrix}, \quad \mathbf{F}(x,t) = \begin{bmatrix} i_{\mathrm{ext}}(x,t)/c_m \\ 0 \\ \vdots \\ 0 \end{bmatrix}.$$

With the definitions above Equation (2.28) can be written in a concise vector form:

$$\frac{\partial \mathbf{u}}{\partial t} = L\mathbf{u} + N(\mathbf{u}) + \mathbf{F} \tag{2.29}$$

The steps of the algorithm are:

1. Determine desired spatial discretization and biophysical parameters.

2. Apply external current i_{ext} to a small spatial region of the resting system to generate a traveling pulse.

3. Fourier Transform Eq. (2.29) to obtain the Fourier mode system of ordinary differential equations:

$$\widehat{\frac{\partial \mathbf{u}}{\partial t}} = \widehat{L\mathbf{u}} + \widehat{N(\mathbf{u})}. + \widehat{\mathbf{F}} \tag{2.30}$$

   Note that the nonlinear operator *couples* all the Fourier modes.

4. Evolve Eq. (2.30) forward in time with any standard time-stepping ODE scheme.

5. Apply the inverse Fourier transform to $\widehat{\mathbf{u}}$ to recover $\mathbf{u}$. Note that the inversion must occur every time-step Δt since the nonlinearity must be re-evaluated and recomputed in Eq. (2.30).

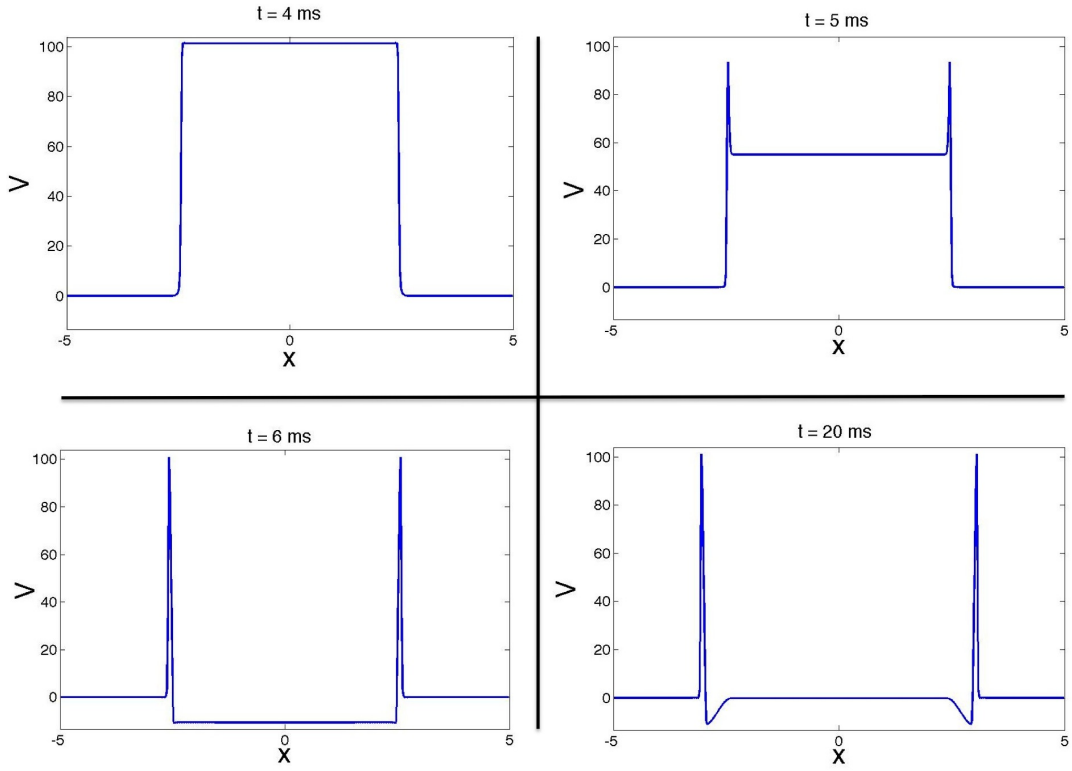

Figure 2.8: Snapshots of the voltage field $V(x,t)$ for different times. An external current shot i_{shot} of sufficient intensity excites a narrow spatial region creating traveling Hodgkin and Huxley spikes. Details of spike stimulation vary according to the specific Action Potential model but its formation is ubiquitous for all of them.

A good option for time-stepping Eq. (2.30) is the Dormand-Prince Runge-Kutta 4-5 algorithm (`ode45` in MATLAB). The use of FFTs constrain the scheme to periodic boundaries, but one can set them sufficiently far away from the region of interest so as to make their effects negligible.

If the radius $a(x)$ and the resistivity $r_L(x)$ are constants no FFT is required for $\widehat{L\mathbf{u}}$ since the only nonzero entry simplifies to $\frac{-ak^2}{2r_L}\widehat{u_1}$. Advantages of this method include the accuracy of the spectral representation (beyond all orders accuracy) and the speed of the underlying FFT algorithm. Our Matlab codes were made available in the supplemental material of [74].

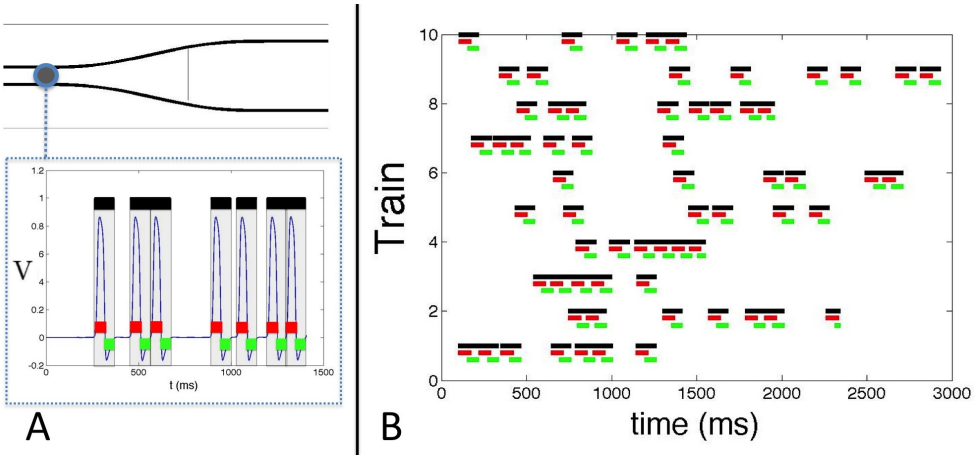

Figure 2.9: Fig. **A** records a FitzHugh-Nagumo spike train as it passes through the measuring spot. We set upper (red) and lower (green) thresholds values for voltage to mark the spike occurring times. The approximate width of a spike (given in black) will be used to estimate the resolution of the system. Fig. **B** shows a raster plot for a small set of Poisson Spike Trains generated with firing rate $\lambda = 0.005$.

2.2.2 Improvements

The pseudo-spectral algorithm described earlier is fairly standard [66, 112], but we added a few improvements to resolve larger spike trains.

Generating spikes effectively: There are several ways to generate a traveling spike pulse that is the basis of the spike-train encoding format, although details of spike train stimulation may vary according to the specific neuronal model used. In this work we will do so by applying a current shot of sufficient intensity Q in a narrow spatial region $[x_L, x_R]$ at time t_j for a short duration τ, i.e.,

$$i_{shot}(t_j) = \begin{cases} Q & \text{if } (x,t) \in [x_L, x_R] \times [t_j, t_j + \tau] \\ 0 & \text{otherwise} \end{cases} \tag{2.31}$$

The length of the narrow region and the values of the parameters above vary according to the selected biophysical model. The spike generation for a Hodgkin-Huxley model is schematized in Figure 2.8. A train of N spikes initiated at times $t_1, \cdots, t_N$ will be generated by successively applying current

shots.

$$i_{\text{train}}(t_1,\cdots,t_N)=\sum_{j=1}^{N} i_{shot}(t_j) \tag{2.32}$$

By setting the external current $i_{\text{ext}}=i_{\text{train}}(t_1,\cdots,t_N)$ in a narrow region of the axon we can generate a propagating spike train. We will refer the train as a Stochastic Poisson Train with firing rate λ if the spike initiation times t_j are generated by a Poisson process; Recall that the Inverse CDF formula for a Poisson random variable is $F_x(x)=1-e^{-\lambda x}$. This can be rearranged to give $x=-ln(1-F_x(x))/\lambda$ and $1-F_x(x)$ can be replaced by a Uniform random variable U(0,1). So, 2 lines in MATLAB suffice to generate intervals and spike times for a Poisson input with a firing rate λ:

```
isi = -log(rand(1,Nspikes))/lambda;
spikes = cumsum(isi);
```

Finally, we remark that each spike in the train (1) requires certain time to be generated by the excitation dynamics of the biophysical model and (2) is followed by a refractory period in which no spikes can occur. Thus, a spike initiated within the refractory period of the previous one will not be formed.

Absorbing Mask: Simulations of large spike trains require large spatial domains $[-L/2,L/2]$. In [2] they map an infinitely long axonal segment into a finite one by applying a judiciously chosen transformation. Nevertheless, significant computational power is spent resolving the dynamics of spikes far from regions of morphological interest. This could be avoided by adding regions to absorb spikes near the endpoints of the spatial domain:

$$Mask=\begin{cases} -M\cdot|V-V^{\text{rest}}| & \text{if } x\in[-\frac{L}{2},-\frac{L}{2}+\varepsilon]\bigcup[\frac{L}{2}-\varepsilon,\frac{L}{2}] \\ 0 & \text{otherwise} \end{cases} \tag{2.33}$$

The mask penalizes with intensity M the values of V differing from V^{rest}, destroying spikes passing through the absorbing regions. See Figure 2.10. It will not affect the spike dynamics elsewhere and the measuring spots will record large spike trains if many current shots are applied. Instead of artificially increasing the spatial domain to fit large trains the mask allows L to be roughly of the same length of regions of morphological interest.

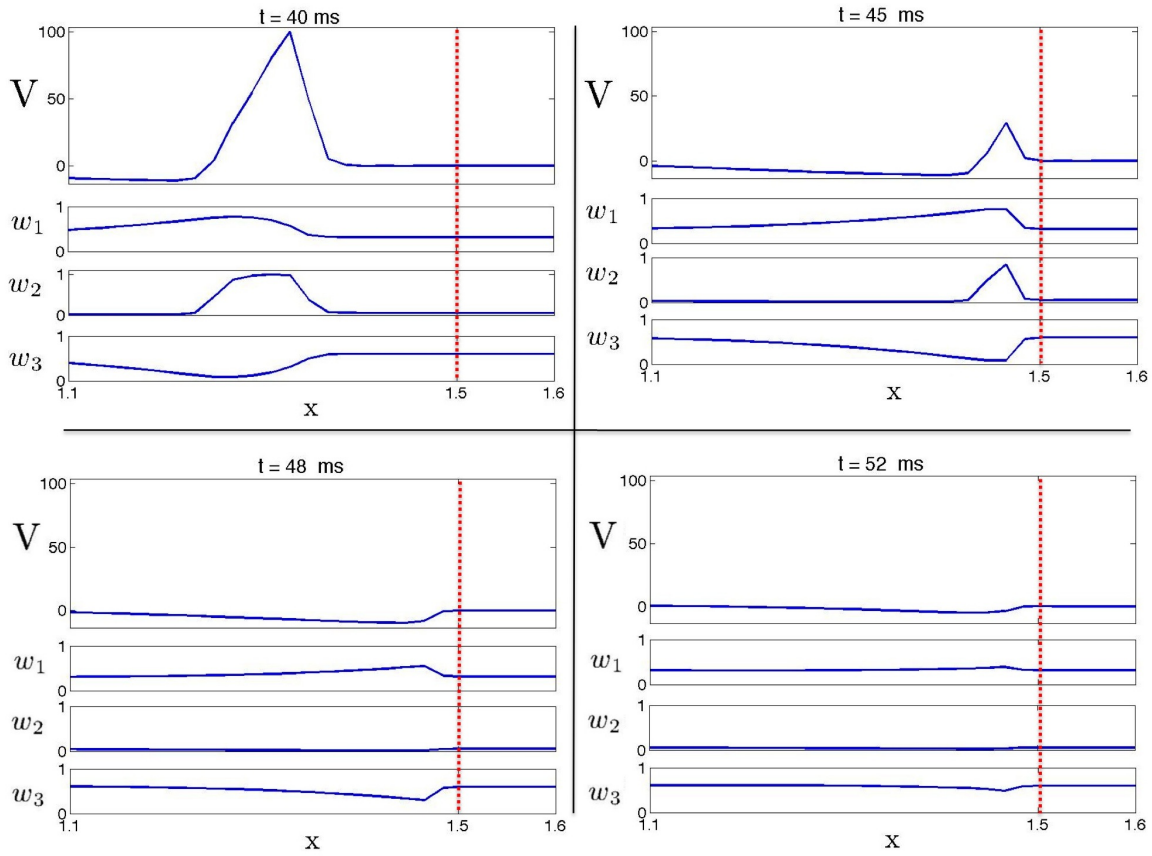

Figure 2.10: Absorbing Mask (in red) placed at $x = 1.5$ destroying a Hodgkin and Huxley spike. Reducing V to V^{rest} breaks down the entire coherent traveling structure and all auxiliary variable fields are eventually reduced to their constant resting state.

Table 2.2: Different propagation behaviors on branch points of passive cable according to Rall's Geometric Ratio (GR) parameter – see Equation 2.34.

value of GR	Description
$GR = 1$	perfect impedance match, propagation occurs in both branches
$GR < 1$	propagation delay past the branch point
$1 < GR < 10$	mother branch may not activate both branches
$GR > 10$	conduction block occurs in all daughter branches

2.2.3 Previous analytical and numerical results

W. Rall ([99]) established pioneering analytical results for passive neuronal cables. His 3/2 law [92, 93] relates geometry to propagation properties in fibers containing linear ionic currents via the Geometrical Ratio (GR) – a key parameter obtained from the diameters of a mother branch splitting into two daughter branches:

$$GR = (d_{\text{daughter 1}}^{3/2} + d_{\text{daughter 2}}^{3/2})/d_{\text{mother}}^{3/2} \tag{2.34}$$

Rall's description of how different GR entail different propagation properties is summarized in Table 2.2. The result was later generalized for splitting into k daughters ([99]). A simple jump discontinuity in diameter is included as a particular case when one of the daughter branches is zero. Even if this description for linear cables has significant discrepancies with the active case ([43]), it helped anticipate many experimental findings in dendrites and spines ([56]).

Markin and Chizmadzhev (see [98] and references therein) simplified i_{ion} to a piecewise linear function of time that mimics the inward flow of sodium ions and outward flow of potassium ions. With a suitable Green's function they find an analytical solution for the voltage dynamics $V(x,t)$. Khodorov [62] combined this result with an impedance match condition to derive a blocking condition for spikes when there is a jump in diameter from δ_B to δ_A,

$$\left(\frac{\delta_A}{\delta_B}\right)^{3/2} > \kappa + 1.11\sqrt{\kappa} - 1.69 \approx 5.2 \tag{2.35}$$

where $\kappa = max(V)/V_\theta$ and V_θ is a known threshold value. Mornev extended this results (Leading Edge model) by deriving a blocking condition for a cubic-shaped i_{ion} of the form $V(V-V_1)(V-V_2)$,

$$\left(\frac{\delta_A}{\delta_B}\right)^{3/2} > \sqrt{1+\frac{1-2\mu}{\mu^3(2-\mu)}} \approx 5.9, \tag{2.36}$$

where $\mu = V_1/V_2$. One can apply equations (2.35)-(2.36) to branch point switching $(\delta_A/\delta_B)^{3/2}$ for the GR. For a review of earlier analytical blocking conditions see [98]. Despite inaccuracies due to undeniable oversimplifications, such conditions do provide a crude global characterization of two out of three propagation regimes based on few geometric parameters. We will show how to construct a regime number that includes not only transmission and blockage but also reflection of pulses.

Zhou and Bell [124] also derived blocking conditions for similar diameter discontinuities in a model of dendritic spine with Morris-Lecar dynamics. Diameter tapering was studied numerically and reflected pulses were reported. Ermentrout and Rinzel ([96], [31]) approximated the inhomogeneous diffusion operator in Equation (2.28) by a linear coupling term in a two compartment model where the latter is enlarged to mimic a jump in the diameter:

$$\frac{1}{2a(x)}\frac{\partial}{\partial x}\left(\frac{a^2(x)}{r_{\text{L}}(x)}\frac{\partial V}{\partial x}\right) \approx \frac{g_l}{d_i}(v_j - v_i), \tag{2.37}$$

where v_j is the voltage of compartment j with unitary diameter and v_i the voltage of compartment i with diameter d_i. Both compartments have Morris-Lecar dynamics and their analysis suggest that reflected waves are a consequence of an unstable periodic orbit in the dynamics of the coupled system. If an incoming initial condition leads to a trajectory that comes near this orbit, then a reflected spike (described as an echo wave) can occur. Their argument is supported by numerical computations.

We stress that all results above simplify drastically either nonlinearities of the neural models or the geometry of the fiber. As a result some incompatibilities and inconsistencies arise such as (i) Khodorov [62] predicting that Hodgkin-Huxley reflected pulses die away, (ii) Altemberger et al. [2] not finding reflections in the Morris-Lecar dynamics when Ermentrout [31] predicted such phenomena for a large range of parameters, and (iii) Zhou and Bell [124] claiming that echo waves do not appear to exist in such models as the FitzHugh-Nagumo system when in fact they do. Additionally, the discontinuous jump in diameter assumed in the analytic theories misses the important fact that slow changes in geometry allow for very large diameter changes to occur without

jeopardizing transmission functionality. We will show in the next chapter that these theories do not capture the proper propagation regimes in more realistic geometrical reconstructions.

The nonlinear nature of the nerve equations constrained most of the investigations on geometry effects to numerical studies. Cooley and Dodge [21] derived a finite difference scheme for a homogeneous Hodgkin-Huxley axon using closed integration formulas obtained from the trapezoidal rule. Numerical analysis of the scheme and some of its variations were discussed in [79]. Khodorov et al. [62] included single step jump in the fiber diameter. Parnas et al. ([88], [90]) modified the derivation in [21] to include an axon of varying diameter. With this modification they concluded that a taper facilitates pulse transmission compared to a jump discontinuity in diameter. Goldstein and Rall [44] studied how step decrease or increase of diameter, branch points, and gradual taper affects shape and velocity of APs in a specific model of the olfactory bulb ([94]). Conduction blockage and reflection were reported. Grossman et al ([46], [47]) demonstrated that contrary to the predictions of Rall that propagation of APs through a branch point fails at high frequencies. Luscher et al. [71] analyzed Hodgkin-Huxley axons with short collaterals and synaptic boutons reporting blockage and reflection of pulses. Boutons are shown to enhance propagation through critical branch points. Investigations on more complex arborizations, influence of spike train frequency to propagation and integrative properties of terminals were done in [70]. Segev [100] highlights the insights gained from such computational models.

The numerical results above and others [2, 121] incorporated nonlinearities and axonal enlargements in much detail then the analytical results but *they lack concise expressions relating geometry to different propagation regimes*. Our goal is to formulate a precise global characterization discriminating transmission, reflection and blockage of action potentials.

Chapter 3

HOW THE GEOMETRY OF FAS CAN AFFECT SPIKE PROPAGATION

In this chapter we develop a theoretical and computational framework to distinguish FAS that minimally affect spike propagation from those that lead to critical phenomenon such as reflection or blockage. We use a few geometrical parameters to model an idealized shaft enlargement and explore the parameter space – characterizing all possible propagation regimes and dynamics in standard Action Potential models. Contrary to earlier notions that large diameter increases mostly lead to blocking, we demonstrate that transmission is stable provided the geometrical changes occur in a slow manner. Our method also identifies a narrow range of parameters leading to a reflection regime. The distinction between these three regimes can be evaluated by a simple function of the geometrical parameters inferred through numerical simulations. We suggest that evaluating this function along axon segments can detect regions most susceptible to (i) transmission failure due to perturbations, (ii) structural plasticity, (iii) critical swellings caused by brain traumas and/or (iv) neurological disorders associated with the breakdown of spike train propagation.

This chapter follows closely the article *Identifying critical regions for spike propagation in axonal segments* by Maia and Kutz (2014) [74]; we removed sections covered or reviewed in other chapters and added details to others. A few parts were also edited to improve the clarity of the text.

We evaluate Action Potentials (spikes) under the influence of geometry in order to: (i) identify different propagation regimes including transmission, reflection and blocking; (ii) provide concise expressions for delimiting regime interfaces for the fully nonlinear, inhomogeneous propagation dynamics; and (iii) characterize the stability of neuron transmission under axonal perturbations. Specifically, the regimes can be characterized by a single parameter η that takes into account how rapidly the transition occurs and the magnitude of the transition. We model an axonal enlargement and/or varicosity by a cylindrical shaft with varying radius $a(x)$. This is reasonable from a biological

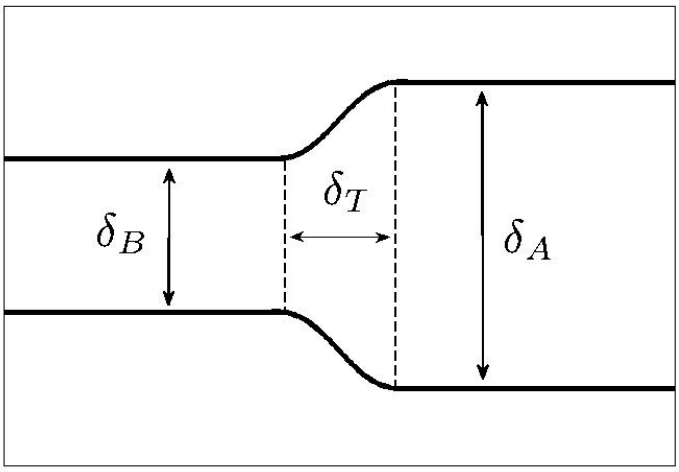

Figure 3.1: Axonal enlargement $a(x)$ given by Eq. (3.1). Diameter δ_B is increased up to diameter δ_A through a transition region of length δ_T.

point of view since the majority of varicosities are essentially tubular (see again [102] and references therein). As illustrated in Fig. 3.1 the diameter δ_B is constant before the inhomogeneity then is increased or decreased in the transition region of length δ_T until it reaches a diameter value of δ_A. The parameter δ_T is of extreme importance since it distinguishes abrupt changes in diameter from slow/adiabatic modifications. This feature is often neglected in both analytical and numerical investigations, but as will be shown, it is found to be critical in practice. Many analytical expressions for $a(x)$ can be used to specify a smooth sigmoid between the two radiuses, but we follow [2] and prescribe the geometry as follows:

$$a(x) = \begin{cases} \delta_B & \text{if } x \leq 0, \\ \tilde{a} & \text{if } 0 \leq x \leq \delta_T, \\ \delta_A & \text{if } x \geq 0. \end{cases} \tag{3.1}$$

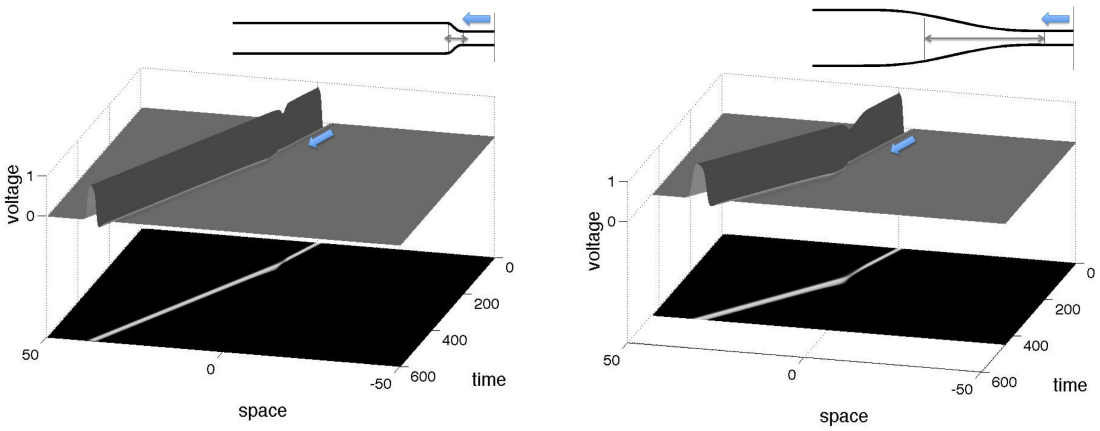

Figure 3.2: Transmission of FitzHugh-Nagumo pulses across an axonal enlargement as in Fig 3.1 for parameters $[\delta_B = 1,\ \delta_T = 0.5,\ \delta_A = 2.1]$ (top) and $[\delta_B = 1,\ \delta_T = 4,\ \delta_A = 5.4]$ (bottom).

where

$$\tilde{a} = \delta_B + (\delta_A - \delta_B)\left[10\frac{x^3}{\delta_T^3} - 15\frac{x^4}{\delta_T^4} + 6\frac{x^5}{\delta_T^5}\right].$$

In what follows, we will explore in detail how different combinations of the parameters δ_B, δ_T and δ_A characterize the transmission, reflection or blockage of the initial traveling spike. Three things should be noted at this early juncture: (i) transitions in which $\delta_B > \delta_A$ always faithfully transmit spike train encodings, (ii) for sufficiently slow geometry changes, i.e. gradual tapering, we observe that transmit spike train encodings are once again faithfully transmitted, even for very large overall increase in diameter where $\delta_B \ll \delta_A$, and (iii) we will show that a single parameter (η) constructed from δ_B, δ_T and δ_A is sufficient to distinguish the various propagation regimes of transmission, blocking and reflection.

3.1 Characterizing spike propagation regimes

In this section we demonstrate through numerical simulations the different propagation regimes for the FitzHugh-Nagumo ([39], [85]) inhomogeneous cable equation subject to geometric changes characterized by the parameters δ_A, δ_B and δ_T. From the variety of dynamical behaviors supported by the model, see for instance [57] or [98], we pick parameters that will lead to the formation of a single traveling pulse. With this pulse, we can characterize the stability of the spike train encoding as

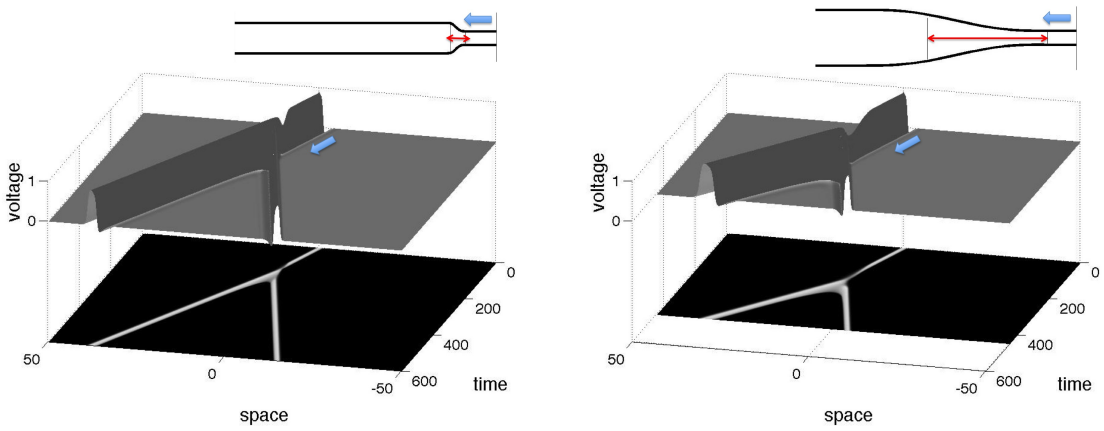

Figure 3.3: Reflection of FitzHugh-Nagumo pulses across an axonal enlargement as in Fig 3.1 for parameters $[\delta_B = 1,\ \delta_T = 0.5,\ \delta_A = 2.2]$ (top) and $[\delta_B = 1,\ \delta_T = 4,\ \delta_A = 5.5]$ (bottom).

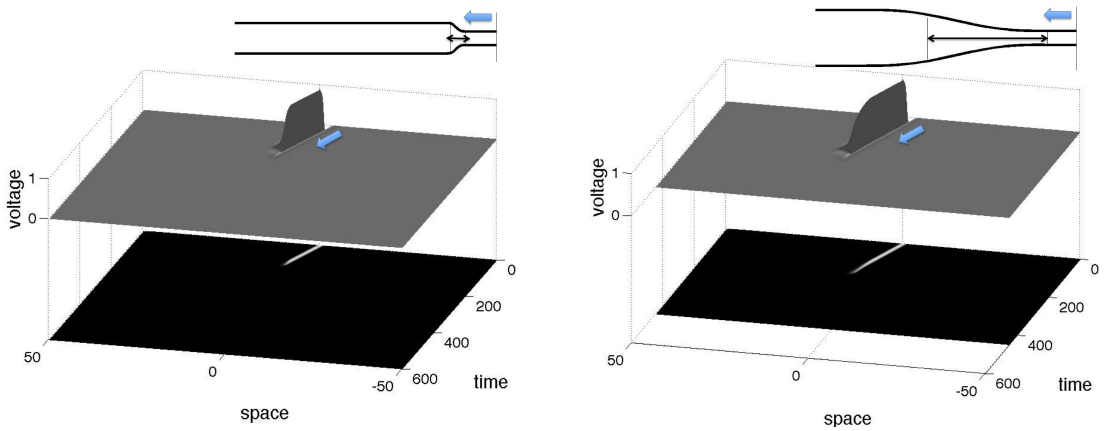

Figure 3.4: Blockage of FitzHugh-Nagumo pulses across an axonal enlargement as in Fig 3.1 for parameters $[\delta_B = 1,\ \delta_T = 0.5,\ \delta_A = 2.3]$ (top) and $[\delta_B = 1,\ \delta_T = 4,\ \delta_A = 5.6]$ (bottom).

a function of axon varicosity. Although the FitzHugh-Nagumo model was chosen, the methodology can be extended to any axonal or dendritic conductance-based model.

3.1.1 Transmission, Blockage and Reflection.

The geometrical description of the propagation is depicted in Fig. 3.1. The basic idea is to think of this geometry change as a prototypical example of varicosity in realistic axons. When going from larger to smaller geometries where $\delta_B > \delta_A$, faithful transmission of spike train encoding is always preserved. However, when going from smaller to larger geometries where $\delta_B < \delta_A$, much more interesting dynamics can potentially occur depending upon the parameters δ_A, δ_B and δ_T. In particular, these parameters determine whether transmission, reflection or blocking occurs. Each case will be considered in turn.

Transmission: In Fig. 3.2 we depict spike transmission for two different set of parameters: (1) a relative small increase in diameter in a short transition length and (2) a large increase in diameter in a longer transition length. In both cases there is increase in the width and speed of the traveling pulse after going through the geometry with the effect greatly pronounced in the latter due to the larger diameter change.

Reflection: A drastic change in the propagation dynamics occurs by slightly increasing δ_A from the previous parameter settings of Fig. 3.2. As illustrated in Fig. 3.3, the pulse decreases its voltage when it reaches the transition zone and splits into two pulses. One is transmitted, with larger speed and width, and the other propagates backwards (or reflected) with the same speed and width of the original pulse. This is the hallmark feature of an axon that exhibits reflection. And although one can see that the information encoded in the single spike does indeed transmit through the axon, the backward propagating spike has the potential to interact with, and potentially destroy, the next spike in a spike train. This has a fundamental impact on the encoding and information transmitted to downstream neurons.

Blockage: A further increase in δ_A from those used in Figs. 3.2 and 3.3 will block the pulse as depicted in Fig. 3.4. Without changing δ_T or δ_B, any larger value of δ_A will result in the same be-

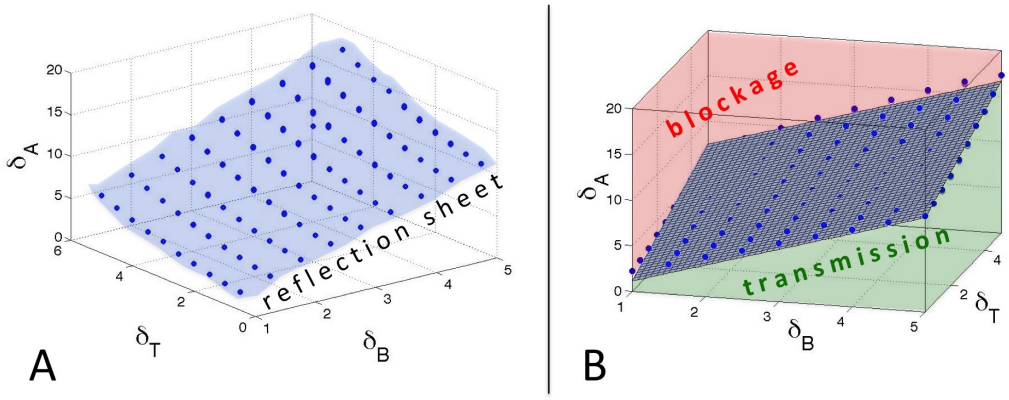

Figure 3.5: Map of the space of axonal tapering parameters $[\delta_A,\ \delta_B,\ \delta_T]$ to their corresponding propagation regimes. In Fig. **A**, reflection occurs for parameters in the blue region. In Fig. **B** the reflection region is approximated by a plane. Blockage occurs for values above the plane and transmission occurs for values below the plan. A planar function $\eta(\delta_A,\ \delta_B,\ \delta_T)$ can be inferred summarizing how geometry relates to function.

havior. Thus the limit of faithful transmission, or an upper limit on varicosity, can be determined under which the axon will perform its natural function.

These different propagation regimes are similar to the ones described in Altemberger et al. [2] for axons modeled by the Hodgkin-Huxley AP model. Thus, contrary to some earlier predictions ([124]), the FitzHugh-Nagumo reduction can in fact capture the qualitative interplay of the ionic currents and the geometrical properties of the cable. We emphasize that not only must the magnitude of the diameter increase be accounted for, but the rate at which the geometrical change takes place as well. Indeed, one can see from the figures presented that quite large geometrical changes can still support transmission provided the change occurs sufficiently slowly. The analytic blocking conditions, such as those described in the previous section, should thus be used with caution since they typically do not include parameters to describe the smoothness of the transition.

Interestingly, many physical systems are allowed to adapt their configuration if the changing conditions occur gradually (adiabatic process) and prevented if it occurs rapidly (diabatic process).

Adiabatic changes are common in optical waveguide theory to assure faithful transmission of data [77]. Thus there are interesting similarities and connections between AP propagation and optical fibers and lightwave transmission systems.

3.1.2 Exploring the parameter space

Here we map points in the parameter space $[\delta_B, \delta_T, \delta_A]$ used to specify different axonal enlargements (see Fig. 3.1) to their corresponding propagations regimes illustrated in Figs. 3.2, 3.3 and Fig. 3.4. We perform simulations for the FitzHugh and Nagumo model, but based on the results of [2] one should expect transmission for $\delta_A < \delta_B$, blockage for $\delta_A \gg \delta_B$ and a thin intermediate region where reflection occurs. Thus we:

1. Fix δ_B and δ_T and explore relatively high values of δ_A where blockage is expected to occur.

2. Perform a bisection-like search algorithm in the range interval of δ_A to delimit where changes in propagation regimes are observed.

3. Explore regions where regime changes in detail by increasing the resolution of the PDE solver.

4. Loop through other values of δ_B and δ_T and perform the algorithm once again. Generate the interface between Transmission (T), Reflection (R) and Blockage (B).

The production of the T-B-R interface in Fig. 3.5 A is the result of the algorithm. Since the reflection region occurs only for a narrow range of parameters it can be well approximated by a two-dimensional plane as displayed in Fig. 3.5 B. Thus, if one selected the geometrical parameters randomly within the displayed range it is unlikely that a reflection would occur. This might not be true for parameters not covered by our simulations since the thickness of the reflection region exhibits an increasing trend (see Figure 3.6).

3.1.3 The T-B-R number η

The best plane fit of the reflection region yields

$$\eta = -1.842 + 2.284 \cdot \delta_B + 1.415 \cdot \delta_T - \delta_A \tag{3.2}$$

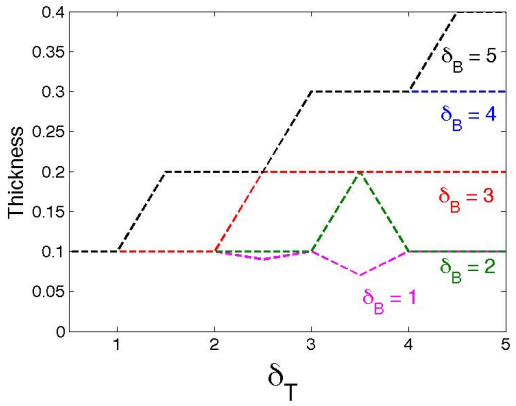

Figure 3.6: Detailing the narrow reflection region from Fig. 3.5. We plot for fixed values of δ_B how the thickness of the sheet varies with δ_T.

where the MATLAB surface fitting tool *sftool* was used to construct this best fit approximation. Within this description, the pulse will be blocked if $\eta \ll 0$ and will be transmitted if $\eta \gg 0$. For $|\eta| \approx 0$ the axon geometry is critically close to the reflection interface separating the transmission and blocking regimes. Eq. (7.1) combines the best of two worlds: the conciseness of an analytical condition with accurate numerical simulations without simplifying assumptions in the nonlinearities of the model and/or geometry of the core conductor. This parameter characterizes axonal enlargements that are critically sensitive and can trigger dramatic dynamical changes in spike propagation. It can be conjectured that extreme axonal swellings induced by brain trauma ([80, 105]) will generate varicosities with $\eta \ll 0$, blocking propagation and ruining axonal function. Intermediate swellings, with $\eta \approx 0$, still allow for transmission but creates reflecting spikes as a partial dysfunction. Finally minor swellings will diminish the value of η, but maintain faithful transmission. The classification of axonal swellings via η can be used to describe the hierarchy of non-disruptive axonal injuries. And since varicosities are present in non-injured axons as well, those structures with $\eta \approx 0$ are more likely to influence connectivity and structural plasticity properties of the neuron ([9, 15, 16, 23, 42, 55]).

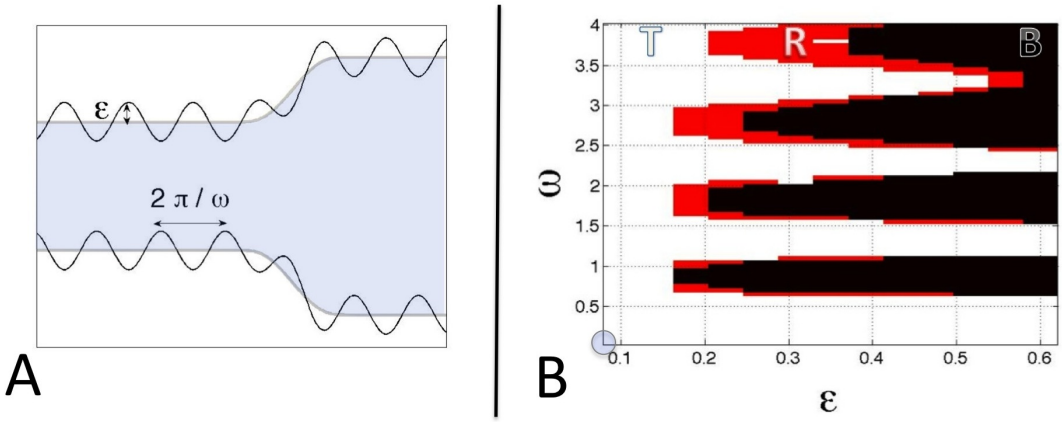

Figure 3.7: Dynamical effects of small perturbations in critical geometric configurations: Fig **A** schematizes an axonal enlargement $a(x)$ for which sinusoidal perturbations are added obtaining $a_\varepsilon(x) = a(x) + \varepsilon \cdot \sin(\omega x)$. Figure **B** shows that an axonal enlargement with parameters $[\delta_B = 5,\ \delta_A = 17,\ \delta_T = 5]$, which originally allow for pulse transmission ($\varepsilon = \omega = 0$), might reflect (red), block (black) or transmit (white) pulses depending of the values of ε and ω in the perturbation term.

3.1.4 Dynamics near critical regions

In this subsection we illustrate how small wrinkles or perturbations in diameter, can dramatically affect spike propagations for axonal enlargements near the critical regime of $|\eta| \approx 0$. Studies near this critical region are performed as follows:

1. We consider axonal enlargements $a(x)$ as given in Fig 3.1 with parameters $\delta_B = 5, \delta_A = 17, \delta_T = 5$ for which the pulse is transmitted.

2. As depicted in Fig. 3.7A, we add a sinusoidal perturbation to the perfect axonal geometry and obtain a modified axon geometry of the form

$$a_\varepsilon(x) = a(x) + \varepsilon \cdot \sin(\omega x). \tag{3.3}$$

   where ε characterizes the strength of the perturbation and ω characterizes the perturbation frequency.

3. We map different values of $[\varepsilon, \omega]$ from $[0, 0.6] \times [0, 4]$ to their corresponding propagation regimes. We explore the parameter space with well resolved steps in the $\varepsilon - \omega$ plane of 0.05 so that more then 1050 different geometrical configurations are ultimately considered. Each configuration considered is classified as supporting transmission, reflection or blocking.

4. The output of this parameter space exploration is displayed in Fig. 3.7B where regions of transmission (white), reflection (red) and blockage (black) are delineated. As might be expected, for $\varepsilon \to 0$, the perturbation goes to zero and transmission always occurs. As $\omega \gg 1$, the perturbation frequency is sufficiently high so that the propagating spike only sees a zero average and transmission is once again accomplished.

We selected this initial set of geometrical parameters because they lead to a small regime number of $\eta = 1.9925$. Thus the initial transmission geometry is located close to a reflection region with large thickness (around 0.5, see Fig 3.6). We avoided studying how perturbations affect the propagation regimes near regions with thin reflection regions since they would likely result in a simple dichotomy between transmission and blockage regimes.

In approximate terms, Fig. 3.7B depicts the transmission region (white) and the blockage (region) as two entangled combs separated by a thin reflection (red) snake-like region. Thus an axonal enlargement of critical regime number ($|\eta| \approx 0$) can virtually switch to any other dynamical regime if either ε or ω are altered.

Our results corroborate the viewpoint of Shepherd and Harris [102]. Namely, that it is not only the size of small bumps (characterized by ε), but also the *spacing* between them (characterized by ω), is of crucial importance. Changes in size or displacements of small axonal microstructures in regions of critical axonal enlargements - induced by eventual long term potentiation effects or metabolical changes - can be of fundamental importance to understand plasticity effects and connectivity. Moreover, if aging or undesirable external effects deteriorate in the creation of ill-placed microstructures they can, in theory, affect spike propagation dynamics leading to potential axonal dysfunction and neuronal disorders.

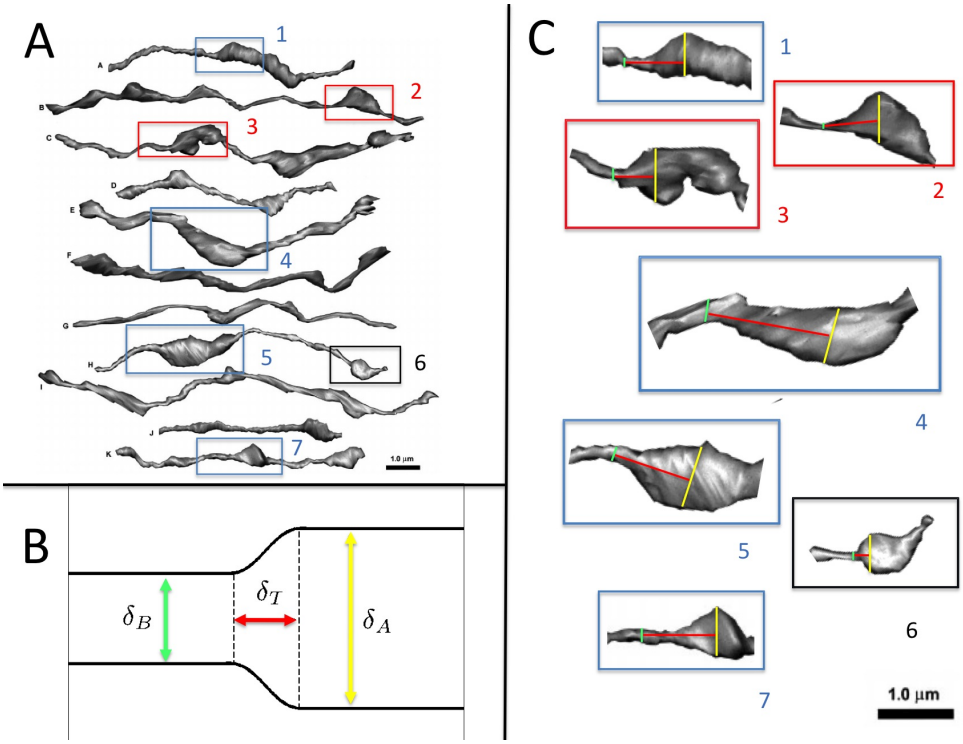

Figure 3.8: (A) Membrane contours for reconstructed unmylienated axon segments of CA3 $\rightarrow$ CA1 rat Hippocampal neurons (Modified from SynapseWeb, Kristen M. Harris, PI, and [102]). The highlighted regimes in blue (transmission), red (reflection) and black (blocking) are the regions of large geometry changes where propagation failure is evaluated. (B) Schematic of axonal enlargement $a(x)$ given by Eq. (3.1) which is applied to regions of large geometry changes identified in A. (C) Detailed enlargements of propagation regimes of most interest where dynamical changes are most likely to occur. Although previous findings (See Table 3.2) predict that all these geometry changes result in blockage, most actually remain faithful in transmission (blue boxes) with some potentially producing reflection (red) or blockage (black). Table 3.1 gives a complete characterization of each highlighted region.

Table 3.1: Characterizing regime numbers from segments displayed in Fig. 3.8 C with suitable normalized geometrical parameters.

Enlargement	δ_B	δ_T	δ_A	η	Prediction
1	1.40	10.37	7.45	5.65	Transmission
2	**1.00**	**9.08**	**8.97**	**1.78**	**Critical Transmission**
3	**1.80**	**7.05**	**9.28**	**0.93**	**Critical Transmission**
4	3.85	21.74	10.22	21.34	Transmission
5	2.45	13.62	11.48	7.37	Transmission
6	**1.20**	**3.02**	**6.94**	**-2.65**	**Blockage**
7	2.31	12.60	8.62	9.04	Transmission

3.2 Applications to axonal classification

As a proof of concept, we apply the results of our theoretical/computational studies to the selected axonal enlargements shown in Fig. 3.8. The biophysics of our AP model is over-simplified for realistically simulating CA1 $\rightarrow$ CA3 hippocampal neurons, but it can be improved by adding synapses, non-uniform distributions of ion channels and a more complete set of ionic currents. We assumed, for example, that the varicosities were made of the same material as the axoplasm. It is likely that a constant resistivity r_L value along the entire axon might not hold. Additionally, most axonal varicosities contained mitochondria (that regulate presynaptic Ca+2) or other possibly electrically active vesicles [102] that were not taken into account by our model. Better quantification of their electrophysiological properties and others, such as distributions of ion channels, pumps, buffers and other molecules, will be required for ideal biophysical modeling. Regardless, our AP model provides interesting results by evaluating the regime number in challenging geometrical configurations. To be more precise, we estimate the geometrical parameters $[\delta_B,\ \delta_T,\ \delta_A]$ using a GNU Image Manipulation Program (GIMP) from the 3D axon reconstructions of Shepherd and Harris [102]. We then apply a normalization compatible with our AP model and calculate the Regime Number η at various points of interest.

The regime numbers for the enlargements in Fig. 3.8C are summarized in Table 3.1. The majority of the varicosities (blue frame) have relatively high values of η and consequently should allow pulse transmission despite significant overall increase in the diameter. This is not surprising

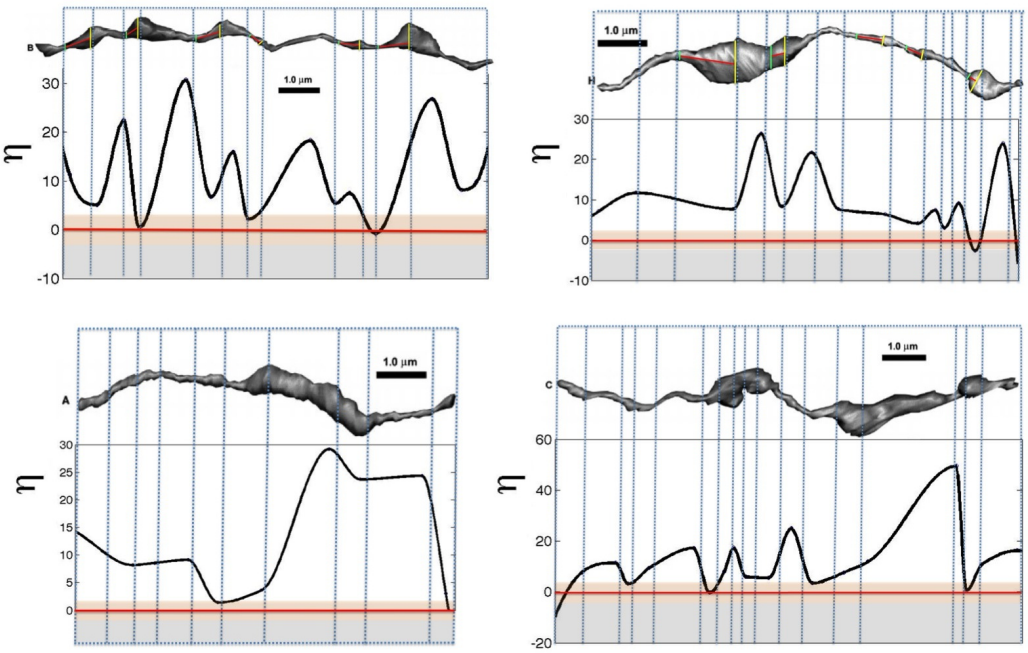

Figure 3.9: Estimates of Regime Number along four prototypical axonal segments. The shaded red region is the region where reflection is likely to occur while the gray region is where blocking of transmission occurs. Note that once the critical η value is evaluated for a given AP model, the axonal segment can be completely characterized without additional simulations of the axon propagation. Such a geometrical evaluation of propagation regimes gives an efficient way to identify potential trouble spots in axon geometry, thus allowing for targeted efforts for drug therapies, for instance. (Modified from SynapseWeb, Kristen M. Harris, PI, and [102]).

Table 3.2: Theoretical predictions of blocking conditions [98]: GR refers to Rall's geometric ratio (2.34), Rall refers to Table 2.2, M-C (Markin and Chizmadzhev) refers (2.35), and Cubic (Mornev) refers to (2.36). Note that almost all the predictions fail to correctly capture the propagation dynamics through the geometry changes.

Enlargement	GR	Rall	M-C	Cubic
1	12.27	Blockage	Blockage	Blockage
2	26.86	Blockage	Blockage	Blockage
3	11.70	Blockage	Blockage	Blockage
4	4.32	Might not transmit	Transmission	Transmission
5	10.14	Blockage	Blockage	Blockage
6	13.9	Blockage	Blockage	Blockage
7	7.2	Might not transmit	Blockage	Blockage

since the changes occurred in a slow manner. In contrast, the segment with the most abrupt increase in diameter (black frame) is predicted to block transmission since it produces a negative value for η. Finally, two of the segments have η values near zero (red frame) and lie close to the interface between transmission, reflection and blockage. It is intriguing that although reflection is expected only for a very narrow range of parameters, such prototypical axonal configurations demonstrated that several variscosities were candidates for reflection behavior.

In Table 3.2 we show how our predictions differ from the earlier analytical blocking conditions from Rall and others. Indeed, the discrepancies between our work and those previously performed are significant, with dramatically different characterizations of the propagation regimes predicted. Our model shows that our characterization remains much more faithful to the true propagation dynamics, thus it can be potentially used to classify realistic axons as shown in Fig. 3.8. Indeed, previous findings, due to their over-simplification, cannot be used to quantitatively predict or classify propagation in real axon geometries.

The most intriguing and powerful use of the techniques developed here is demonstrated in Fig. 3.9. In this figure, we estimate how the regime number varies along entire axonal segments (four axons are demonstrated). We argue that our method gives a practical way to evaluate axon functionality by discriminating between transmission and critical varicosities where reflections (with

$\eta \approx 0$) and/or blockage should occur ($\eta \ll 0$). In particular, one should simply keep track of where the regime number crosses the red zone (near reflection) and grey zones (for blockage) in order to identify potential trouble regions in the axon. With the recent statistical characterization of the distribution and size of axonal swellings induced by injury [72, 108, 109, 119], one can also envision an evaluation procedure for assessing damaged neurons and identifying candidate swellings for blockage through the parameter η. Some traumatic brain injuries, for instance, produce swellings that are thirty-fold the original axon diameter [108, 109]. It can be conjectured that such injured neurons will deteriorate phase coherence properties of the neural network, leading to its dysfunction, and should be prime targets for drug therapies. Alternatively, morphological changes in critical regions of non-injured axons may offer clues as to how neural structural plasticity occurs in practice, with the critical regions mediating the strengthening or weakening of neural connectivity ([9, 15, 16, 23, 42, 55]). This will be the subject of future studies.

3.2.1 Discussion of the results

Physiological studies across a myriad of neural systems seem to agree that axons are much more than reliable cables in which information (spike train encoding) is faithfully transmitted to downstream neurons ([15, 24]). Recently, Debanne et al [25] presented a comprehensive review of experiments reporting unusual operations and propagation dynamics associated with axons. Specifically, propagation failures have been observed in vertebrate spinal axons ([8, 64]), lobster and crayfish motoneurons ([46, 47, 49, 88, 106]), leech sensory neurons ([5, 6, 48, 115, 122]), thalamocortical axons ([27]), rabbit nodose ganglion neurons ([28]), rat dorsal root ganglion neurons ([71, 70]), neurohypophysial axons ([11, 29]), and hippocampal pyramidal cell axons ([26, 81, 107]). Propagation failures also occur when the AP enters a region with an abrupt change in diameter (geometry). This occurs not only with en passant boutons ([13, 58, 123]), but also when impulses propagating along the axon enter the soma ([3, 32, 69]). The review [25] further highlights interesting axonal computations at the brach points of the leech ([5, 6]), where reflection of spike trains can occur ([44, 89, 95]). Such phenomena have also been noted in the axon of a snail neuron ([3]) and demonstrated in dendrites ([18]).

Of critical importance for the information encoded in spike trains and its propagation dynamics

is the axon geometry itself. Indeed, detailed morphological studies highlight the abundance of shaft enlargements and varicosities in axon segments [102]. More recent studies have highlighted the induced geometry changes that occur due to axonal injury [108, 109]. Indeed, traumatic brain injury and concussion studies have produced physiologically relevant statistical information about the distribution of the frequency of the induced axonal swellings and their corresponding size [72, 119]. Such studies reveal the clear role of geometry changes in compromising information encoding to downstream neurons. Additionally, knowledge accumulated over decades (see Section 2.2.3) on analytical and computational studies demonstrate that these enlargements are not simple adornments. Instead they should be regarded as mechanisms that can dramatically alter or modulate the propagation of the original traveling wave: from changes in speed and profile, to even blockage or reflection of the pulse. We revisit this critical subject because (i) most of the analytic reductions posited rely on drastic simplifications of either the geometry and/or nonlinearities of the models and (ii) although numerical investigations allowed for a much accurate understanding of spike train dynamics, they lacked a precise global characterization of the various dynamical regimes observed in practice.

We show that, in a given reduced AP model, a new single number η, that accounts for how rapidly the shaft is enlarged and the magnitude of the enlargement, can characterize all possible propagation regimes in varicosities where regime transitions occur (See Fig. 3.8). This regime number cannot be derived analytically due to the combination of geometry of the shaft and the nonlinearities of the dynamical model. We have developed a computational strategy for computing the regime number and determining its critical value where $\eta \approx 0$. Moreover, the theory guarantees blockage if $\eta \ll 0$ and transmission if $\eta \gg 0$. Near the critical regime $|\eta| \approx 0$, the enlargement is critically close to the transmission, reflection and blocking interface. Thus small perturbations to the axon geometry can lead to significant changes in dynamical response. And although the bulk of this work focuses on the FitzHugh-Nagumo AP model for axons, the methodology can be extended to any axonal or dendritic conductance-based models.

The regime number η provides a concise and practical way to discriminate shaft enlargements or varicosities that are highly susceptible to small perturbations. We illustrate that in those cases, such small perturbations – induced by eventual long-term potentiation effects or metabolical changes – can in fact alter the propagation dynamics and be of fundamental importance to understand plasticity mechanisms and/or neuronal dysfunction. Specifically, if aging effects or swellings caused

by axonal injury result in the creation of ill-placed microstructures, they can in theory affect spike propagation dynamics, leading to potential neuronal disorders associated with axonal dysfunction. Similar undesirable effects might occur in dendrites, since a 5.5-month old child with severe neurobehavioral failure also exhibited numerous varicosities and wild variations in the dendritic diameter ([38, 91]). Our studies, for instance, can be used in conjunction with detailed morphological reconstructions of axons and dendrites in order to identify critical heterogeneous regions and branches that may be more effectively targeted for therapeutic drug delivery in order to combat certain neurological disorders.

3.2.2 Insights on more complex geometries: the axonal pacemaker

The study presented in this chapter focused on changes in the propagation regime of a single pulse within a single swelling. If we consider multiple swellings with different propagation regimes, very complex signaling patterns may emerge.

To illustrate one of these patterns, we construct an axonal "pacemaker" in Figure 3.10. We need two regions that reflect pulses in opposite directions. This way, a pulse can get "trapped" between these regions indefinitely, bouncing back every time it encounter a reflecting enlargement. This is just one example of unusual pattern but one could imagine other constructions.

Acknowledgements: We wish to thank F. Rieke, A. Fairhall, E. Shea-Brown, N. Cayco-Gajic, and E. Shlizerman for insightful discussions related to this portion of the work.

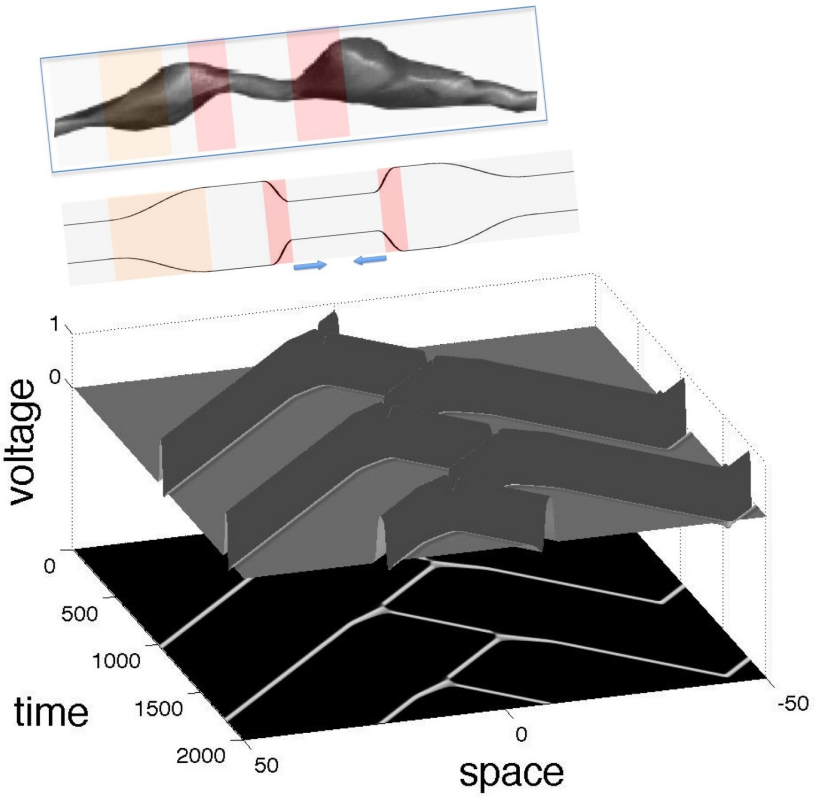

Figure 3.10: The boxed top figure is an axon segment modified from SynapseWeb, Kristen M. Harris, PI, from [102]. It motivates studying propagation in the geometry schematized below, composed by an axonal enlargement that does not affect transmission (orange) followed by two adjacent critical regions (in red) reflecting pulses in opposite directions. The morphological structure can trap a spike indefinitely between the critical regions and operate as a pacemaker. Simulation in the bottom done for the FitzHugh-Nagumo model.

Chapter 4

HOW FAS CAN DEGRADE INFORMATION ENCODED IN SPIKE TRAINS

In this chapter we use spike metric analysis to computationally characterize the effects of FAS on spike train propagation. We compare Poisson spike train classes before and after propagation through an idealized axonal enlargement. Misclassification of spike train classes and low-pass filtering of firing rate activity increases with more pronounced axonal injury. We show that confusion matrices and a calculation of the loss of transmitted information provide a very practical way to characterize how injured neurons compromise the signal processing and faithful conductance of spike trains. The method demonstrates that (i) neural codes encoded with low firing rates are more robust to injury than those encoded with high firing rates, (ii) classification depends upon the length of the spike train used to encode information, and (iii) axonal injuries reduce the variance of spike trains within a given stimulus class. The work introduces a novel framework to quantify the interplay between electrophysiological dynamics with focused axonal swellings generated by injury or other neurodegenerative processes. It further suggests how pharmacology and plasticity may play a role in recovery of neural computation.

This chapter follows closely the article *Compromised axonal functionality after neurodegeneration, concussion and/or traumatic brain injury* by Maia and Kutz (2014) [73]; we removed sections covered or reviewed in other chapters and added details to others. A few parts were also edited to improve the clarity of the text.

Confusion in signal processing: In this chapter we investigate how different (stimulus) classes of spike trains are modified along an injured axon and how they can be potentially misclassified. Our analysis shows that the information loss and probability of misclassification depends on the firing rate and length of the spike train. Figure 4.1 schematizes the analysis performed with classification

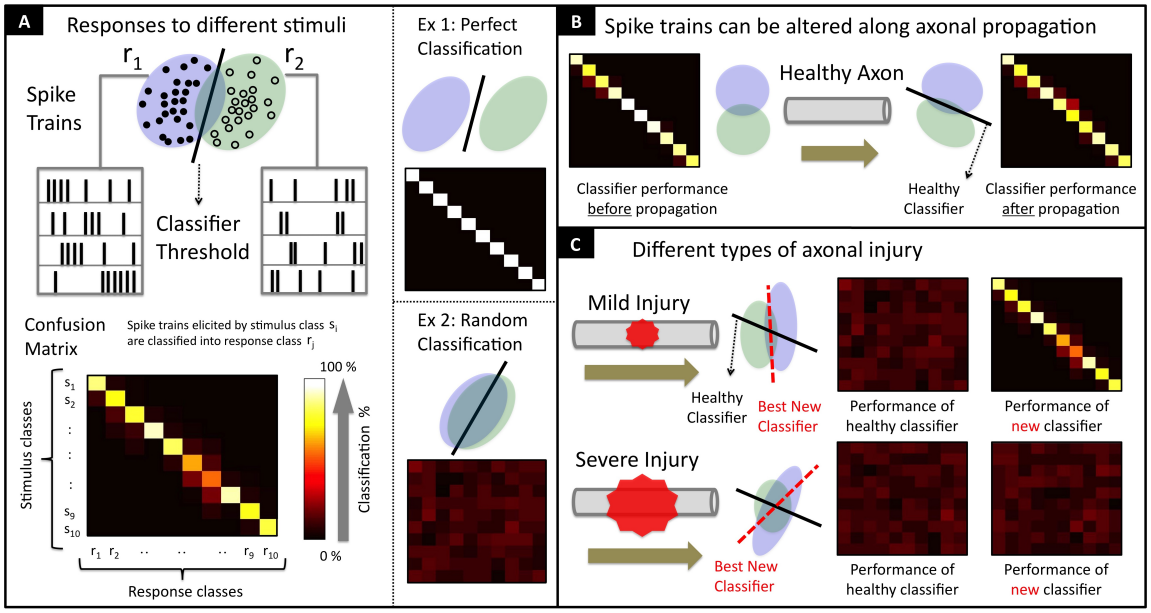

Figure 4.1: Panel **A**. Different stimulus classes elicit spike trains with a degree of separation according to some statistical and/or metric criteria. For multiple stimulus (s_j) and response classes (r_j), the separation is given by a classification or confusion matrix of spike train firing rates. Stimulus classified in the correct response class (s_j and r_j are correctly associated) contribute to the diagonal entries of the confusion matrix while misclassified trains (s_j is incorrectly associated with r_k where $j \neq k$) are responsible for off-diagonal contributions. In the illustration here, and the examples that follow, 10 stimulus/response classes of firing rate activity are considered, leading to a 10×10 confusion matrix. Perfect classification and transmission of information corresponds to a strictly diagonal matrix. The classification becomes less informative as misclassification of the input stimulus occurs and the off-diagonal terms are no longer zero. The limiting case of the confusion matrix is a random classification (no statistical separation) where off-diagonal terms have the same magnitude as diagonal terms. Panel **B**. We assume that an axon is functional when the propagated spike trains are sufficiently separated and informative about which stimulus class triggered them, i.e. the confusion matrix is dominated by the diagonal. Panel **C**. We conjecture that there are two qualitatively different types of axonal injury. A milder injury would reshape spike trains into classes that can still be statistically separated (with a different classifier, in red) but will potentially confuse the triggering stimulus class. A more severe injury would reshape spike trains into classes that are poorly separated by any statistical classifier and uninformative about the original stimulus.

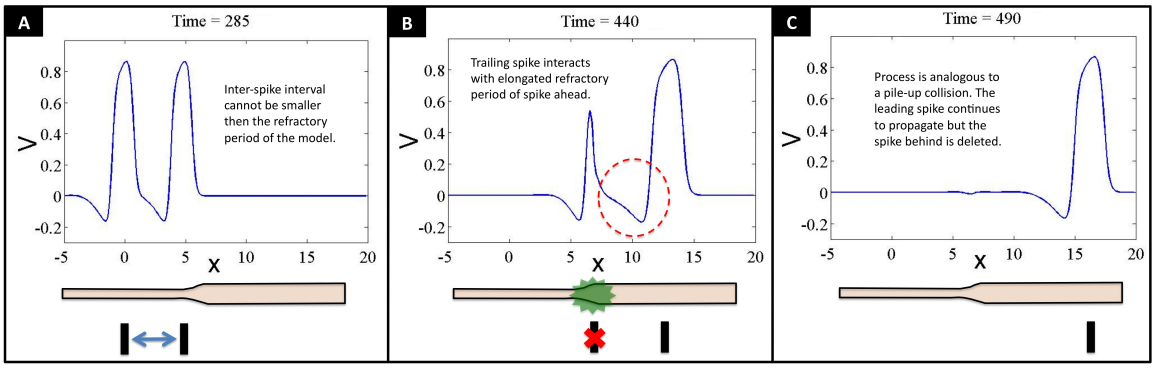

Figure 4.2: Simulation of a pile-up collision. Panel **A** depicts two FitzHugh-Nagumo spikes with a small inter-spike interval between them. In Panel **B**, the front spike reaches the region of axonal enlargement. The change in geometry delays the front spike momentarily allowing the following spike to propagate into its refractory period. In this kind of collision, the trailing spike is deleted and as shown in Panel **C** while the leading spike continues to propagate. Such an effect is responsible for the low-pass filtering of firing rates demonstrated later in the manuscript. The low-pass filtering is strongly dependent upon the size of the FAS.

matrices that only use the pairwise metric distance between spike trains (detailed in Section 4.2). When presented with different stimuli, a healthy neuron generates different classes of spike trains that can be separated by some statistical [22] (for e.g., a linear discriminant) or metric criteria [117] (for e.g., a confusion matrix) (See Panel **A** of Fig. 4.1). Axonal propagation generally modifies the spike train, which may affect the resulting spike train classification: when healthy, the classification after propagation should be quite good (Panel **B** of Fig. 4.1). Mild or severe axonal injury however, leads to degraded statistical/metric separation of spike train response classes. This can generate pronounced effects in the confusion matrix (Panel **C** of Fig. 4.1). Moreover, if neighboring neurons keep the same classifier criteria (or threshold) for both the healthy and damaged spike trains, the encoding-decoding process can have significant amount of stimulus *class confusion*.

Based on the discussion above, we conjecture that two qualitatively different types of injury exist; See Panel **C** of Fig. 4.1. A *mild injury* would reshape spike trains into response classes that can still be separated if a new/different classifier (in red) is used/learned. However, it will probably still confuse the triggering stimulus class for many spike trains until the new classifier is learned. A more *severe injury* would reshape spike trains into response classes that are poorly separated by any classifier, and thus would be completely uninformative about the original stimulus class. In what follows, we quantify the degraded data-processing capabilities of injured neurons.

4.1 Spike collisions and deletion

The extent to which the geometry of the axonal cable can affect the propagation of a *single spike* was reviewed and discussed in detail in the previous chapter. The role of geometry, however, can have further impact on spike train propagation since spikes do not propagate independently. Instead they can interact with each other in a non-trivial manner, especially when there are significant changes in geometry.

The interactions induced by geometry can lead to collision of spikes and consequently to the deletion of one or more of them. Some of these collisions occur even in axonal enlargements known to be in the transmitting regime – where single spikes are known to propagate without many consequences ($\eta \gg 0$ [74]). The deletion of spikes due to morphological axon changes is important as it acts as a low-pass filter for spike train firing rates.

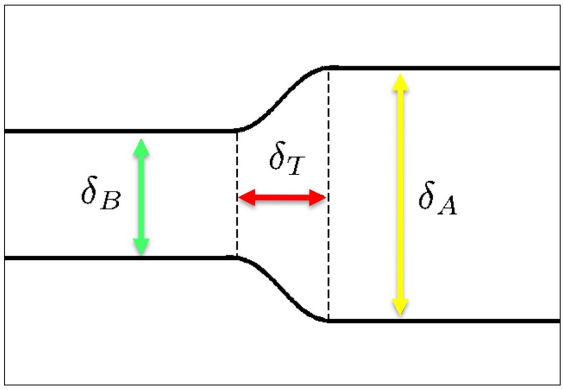

Figure 4.3: Prototypical axonal enlargement. Simulations show that transmission (T), reflection (R), or blockage (B) of spikes can occur depending on the geometric tapering parameters $[\delta_B, \delta_T, \delta_A]$. The relation between geometry and propagation regime is captured by the T-R-B number η (Maia and Kutz [74]).

Pile-up collisions: The first nontrivial collision occurs in an enlargement that allows for transmission. It is a well known analytical result (see [98]) that the speed c of a spike scales with the radius a of the core conductor according to $c \simeq \sqrt{a}$. Recent experimental observations demonstrate the variability of the velocity of a spike propagating along a single axon [7]. Nevertheless our numerical simulations show that when the pulse reaches the axonal enlargement, it is delayed (slows-down) for a short period to adjust its profile (increasing the amplitude and width) before it starts moving forward with increased speed. As a consequence, if two spikes are traveling too close together, the second spike will propagate into the refractory period of the spike ahead and will be attenuated/deleted. This filtering effect [90, 89, 100], or selective blocking effect [62, 88], is particularly problematic for spike trains encoded with high firing rates (See Fig. 4.2 and the animation in the supplemental material).

This pile-up effect increases the minimal distance (or time) required between spikes. It is usually thought that the minimal distance between spikes is determined by the refractory recovery period of the individual neurons [57]. However, axonal geometry changes, especially those created by FAS, can lead to pile-up collisions, and thus it increases the minimum distance between spikes in a way that depends upon the morphological changes. It has been long known that an axonal enlargement

can act as a low-pass filter for firing rate activity [90, 89, 100]. Thus the strength of the filter is directly related to TBI and the induced level of axonal swelling.

In general, the larger the swelling, the stronger the high firing-rate activity is attenuated from neuronal networks. It should also be noted that the deletion of the second spike does not take place immediately and remnants of the soon-to-be deleted spike might affect the propagation of a third spike. Ultimately, the pile-up effect will reshape the original spike train. Such reshaping of a spike train is critical in a spike metric analysis. Indeed, a spike metric analysis directly quantifies such effects and the resulting loss of information.

Collisions with reflected pulses: For specific enlargements where the T-R-B parameters $\eta \approx 0$ [74], reflection of spike trains can occur [44, 89, 95] as has been observed in the axon of a snail neuron [3] and in dendrites [18]. More recently, experimental observations in rat neo-cortical neurons have shown both antidromic and orthodromic propagation, along with a rebound phenomenon, near axonal enlargements [7], thus suggesting that the spike reflection phenomenon may play a role in FAS. The reflection regime will induce the original spike to divide into two pulses: one that will be transmitted and another that will back propagate (See Fig. 4.4 for details and the supplemental materials for an animation). As a consequence, the back propagating or reflected pulse will hit the refractory period of the next spike in the train and vice versa, and both spikes will be deleted. The deletion of both spikes does not take place immediately so that remnants of the deleted spikes can affect a third spike as well. This reshaping of the original spike train is illustrated in Fig. 4.4. For more details about spike reflection, see [31, 74, 96, 124]. The effects of spike-train pile-ups and/or pulse reflections are important types of spike train interactions that can lead to significant modification of a propagating pulse train. A spike train analysis helps to quantify this impact, especially in regards to the loss of transmitted information. And although it is debatable wether or not spike train reflections are a rare event, pile-up events (or selective blocking, studied since [62]) would be a standard phenomenon, especially for filtering high firing-rate activity [90, 89, 100].

4.2 Quantifying changes in spike trains

We now present a series of numerical simulations of spike trains propagating along axons with non-uniform geometries that mimic the effects of FAS observed to results from TBI (see Figure 4.3).

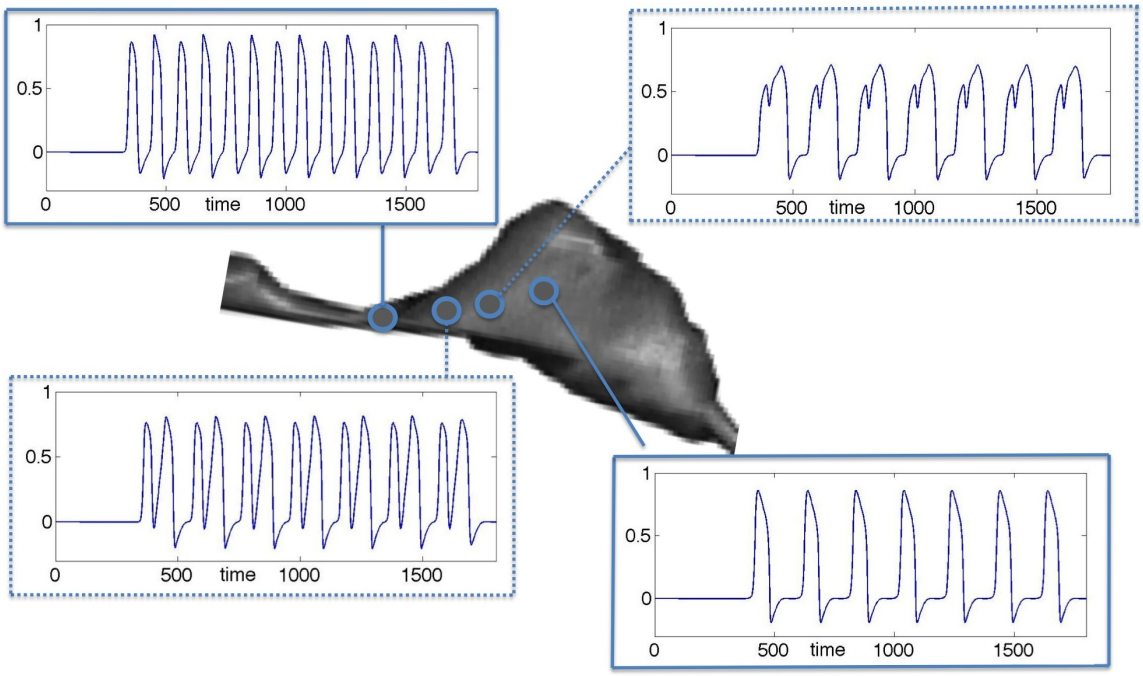

Figure 4.4: Simulation of spike train propagation through a prototypical axonal enlargement in the reflection regime ($\eta \approx 0$). The top left panel records a typical spike train S_A. In the enlargement, back propagating (reflected) spikes are created and collide with the next spike in spike train, deleting both of them (see Section 4.1). The bottom right panel records the spike train after the morphological swelling. Note that although S_A and S_B are measurements of the same propagating train, they differ significantly from each other due to the spatiotemporal dynamics induced by the reflection regime ($\eta \approx 0$). The dissimilarity $d(S_A, S_B)$ is quantified via a spike metric analysis (see Section 4.2.1). The axonal membrane contour is modified from SynapseWeb, and courtesy of Kristen M. Harris, PI,[102].

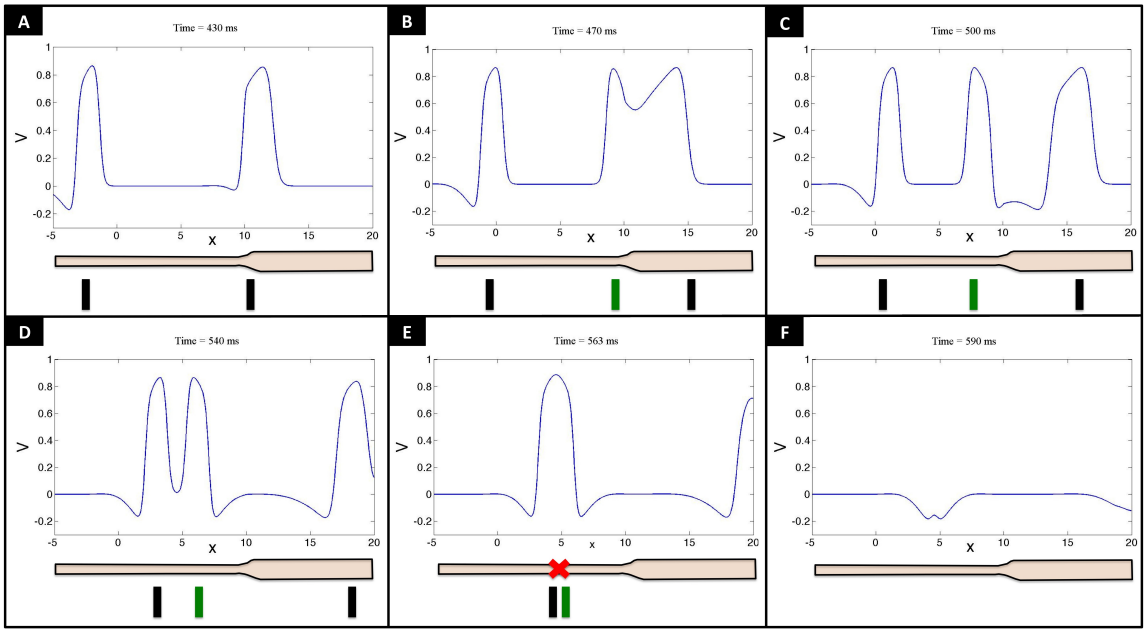

Figure 4.5: Schematics for a collision with a reflected pulse. Fig **A** depicts two FitzHugh Nagumo spikes. In Fig **B-D** the front spike reaches the region of axonal enlargement and divides into two traveling pulses: one propagating forward and another propagating backwards. The backward propagating pulse collides with the second original traveling pulse and, as shown in Fig **E-F**, both spikes are deleted.

The goal is to record simulated spike trains before and after an axonal swelling and quantify how much each train changes. If there is no axonal swelling, spike trains are unchanged and perfect transmission is achieved.

As a first approximation, we consider axonal swellings composed of the same biophysical material as the rest of the axon but with geometrical features consistent with observed varicosities [108, 109]. As discussed in Section 4.1, the interaction between spike pulses with the geometry and/or other spikes in classic conductance-based models can be nontrivial. Additionally, handling spike trains with large number of pulses in a fast, accurate and efficient manner can be challenging. Our computations utilize a pseudo-spectral numerical routine described in [74] with some improvements such as (a) fast spike generation procedures and (b) boundary masks to keep the computational domain approximately of the same length as the morphological area of interest (see Supplemental Materials). Other computational techniques could be used as well (as in [2] or references therein).

Non-dimensional units: It is convenient to simulate non-dimensional systems instead of the original dimensional ones. Thus, spatial units (x), temporal units (t) and voltage fields (V) will be normalized (unit-less) throughout the entire chapter. See [98] (chapters 5-6) or [30] (chapter 6) for details about the normalization procedure.

4.2.1 Spike metric analysis

Victor et al. [4, 116, 117] , introduced a framework to quantify the dissimilarity between spike trains to better characterize neural codes. Spike trains (formed of zeros and ones) are considered points in a *metric space* where a spike train A can be transformed into another train B by a sequence of elementary steps. A cost is associated with each each step with the following rules: (a) it costs 1 to create/delete a spike and (b) it costs $q\triangle t$ to shift a spike by $\triangle t$ in time, with q being a proportionality constant. The metric *distance* between two trains A and B is given by the minimum cost required to transform train A into train B.

We argue that the spike metric framework is specially tailored to quantify how much morphology and/or axonal pathologies reshape spike trains. In the original spike metric framework the rules of creating, deleting and shifting spikes are just steps in the algorithm to quantify dissimilarity. But as detailed in Section 4.1, spike collisions of different kinds and delays are part of the biophysical

Table 4.1: Relation of spike metric rules and FAS effects

Metric Rule	Cost	Morphological Mechanism
Shift spike by $\triangle t$	$q\triangle t$	* Axonal varicosities can cause spike delays. * Spikes travel faster in larger diameter regions. * Remnants of deleted spikes can affect other spikes.
Delete a spike	1	* Both forward and backward propagating spikes are destroyed if collided. See Figure 4.4. * Spike behind is destroyed in a pile up collision. See Section 4.1 and Figure 4.2. * All spikes are destroyed in blockage regime.
Create a spike	1	* In the reflection regime a second backward propagating spike is created. See Section 4.1.

phenomenology of spike propagation in irregular geometries. We summarize these relations in Table 4.1. Most importantly, the transformation of a spike train into another via axon morphology gains biophysical meaning in understanding both (1) the signal processing performed by the healthy axon, and (2) the pathological loss of information in the injured one.

4.2.2 Quantifying transmitted information in neuron responses.

Victor and Purpura [117] extended the spike train metric framework to investigate how much a neuron's distinct responses are informative about the different stimuli that trigger them. Their setup assumes a given set of stimulus (s_j) and response (r_j) classes that are connected through spike trains $t_j^{(k)}$ where j is the given stimulus and k denotes the kth spike train of that stimulus class. The method

is summarized as:

$$\begin{array}{ccccc} s_1 & \rightarrow & t_1^{(1)}, t_1^{(2)}, t_1^{(3)}, \ldots & \rightarrow & r_1 \\ s_2 & \rightarrow & t_2^{(1)}, t_2^{(2)}, t_2^{(3)}, \ldots & \rightarrow & r_2 \\ \vdots & & \vdots \quad \vdots \quad \vdots & & \vdots \end{array}$$

Stimulus class — elicit spike trains that form — Response class

Neurons with less random behavior are expected to have more consistent response classes, i.e., the metric distances between a train t_j and its peers from class r_j will be (on average) smaller then the distances between t_j and trains from other classes.

The quantity that captures how much the association of the response-to-stimulus classes is informative (non-random) is called the **transmitted information** (TI) and quantified by the parameter H [117]. To study the TI across an injured neuron (see Panel **A** from Fig. 4.6) we follow a slightly more complex setup:

$s_{1B},\ s_{2B},\ \ldots$	$\rightarrow$	$r_{1B},\ r_{2B},\ \ldots$	$\rightarrow$	$\star$
External set of stimulus classes generate trains.		The spike trains are arranged in response classes.		Spike trains will travel until they reach the injury.
				$\downarrow$
$r_{1A},\ r_{2A},\ \ldots$	$\leftarrow$	$s_{1A},\ s_{2A},\ \ldots$	$\leftarrow$	$\star\star$
Modified trains are arranged again in response classes.		Injury acts as novel set of stimulus classes on trains.		The injury can reshape each train in a different manner.

Within this context we pose the following questions: are the neuron's response classes $r_{1A}, r_{2A}, \ldots$ after the axonal swelling less informative than the classes $r_{1B}, r_{2B}, \ldots$ before the injury? If yes, which is expected due to the neuronal damage and FAS, what is the relative loss of TI? How many reshaped trains from a post-injury response class can still be tracked back to its original pre-injury class? How many will be confused for a different class? We will address these questions in the next sections.

A simple example: To review the methodology on a simple system [117], consider 2 stimulus classes (s_1, s_2) and a sample of 40 trains triggered by each class: $t_1^{(1)}, t_1^{(2)}, \cdots, t_1^{(40)}$ and $t_2^{(1)}, t_2^{(2)}, \cdots, t_2^{(40)}$

forming two response classes (r_1, r_2). Then the algorithm works as follows:

1. Calculate for each response train the Average Metric Distance (AMD) between itself and (1) response trains elicited from its own stimulus class and (2) response trains elicited from the other stimulus class.

2. Classify trains by choosing the smallest AMD:

	closer to r_1		closer to r_2
for each train elicited by s_1:	α_{11}	or	α_{12}
for each train elicited by s_2:	α_{21}	or	α_{22}

   where the α_{ij} give the number of pulse trains classified into each response class.

3. The α_{ij} are computed by adding a value of 1 to the selected class. If the AMDs are equal, add 0.5 to both classes. The results can be summarized in a **classification matrix A**. An example may look like:

$$\begin{array}{c|cc} & r_1 & r_2 \\ \hline s_1 & 37 & 3 \\ s_2 & 2 & 38 \end{array} \rightarrow \mathbf{A} = \begin{pmatrix} 37 & 3 \\ 2 & 38 \end{pmatrix}$$

   Here, 3 out of the 40 trains triggered by s_1 were, on average, closer to the trains induced by s_2, and 2 out of the 40 trains triggered by s_2 were closer to the trains induced by s_1. It is the same schematic as presented in Figure 4.1.

4. From the classification matrix, calculate the associated transmitted information (H). The matrix above has $H = 0.664$ (See Eq. (4.1) below).

The TI quantifies how much the association of the response-to-stimulus is non-random. In Table 4.2 we present some other examples: a perfect classification matrix, i.e., with maximum TI, is given by a diagonal matrix with entries equal to 40. Since there are only 2 classes, perfect transmission gives $H = \log_2 2 = 1$. Intuitively, TI penalizes non-perfect classification matrices proportionally to the magnitude of its off-diagonal terms. The most random scenario is given by a matrix with all entries equal to 20, where all classes are equally probable and $H = 0$.

In relation to TBI, $H = 1$ would be a healthy axon where faithful spike train propagation is unimpaired. A score of $H = 0$ would represent complete, or random, confusion (misclassification) of the spike trains propagated, and thus a severe loss of cognitive functionality. Our expectation is that H scores would vary from zero to $\log_2$ (*# classes*) as a function of the level of injury.

The above illustrative example was for only two stimulus classes and two response classes. More generally, consider N_{tot} spike trains elicited by stimulus classes $s_1, s_2, \ldots, s_C$ with associated response classes $r_1, r_2, \ldots, r_C$. A classification matrix, $\mathbf{A}$ with computed elements α_{ij}, can then be constructed, and the TI is given by:

$$\begin{aligned} H &= \frac{1}{N_{\text{tot}}} \sum_{\alpha,\beta} \mathbf{A}(s_\alpha, r_\beta) \Big[\log_2 \mathbf{A}(s_\alpha, r_\beta) - \log_2 \sum_a \mathbf{A}(s_a, r_\beta) \\ &\quad - \log_2 \sum_b \mathbf{A}(s_\alpha, r_b) + \log_2 N_{\text{tot}} \Big] \end{aligned} \tag{4.1}$$

More sophisticated criteria than the average metric distance can be used in the classification step. For example, we could (a) minimize the distance between the response and the furthest outlier or (b) classify according to closest individual match instead of the average. For a detailed exposition of the algorithm, discussion of the limitations and biases due to small sample size, and more examples see [117] and references therein. One of the advantages of this framework is that it generalizes well for multiple cases of response classes. The entire classification structure can be easily seen from the matrices depicted in Fig. 4.1 where 10 stimulus/response classes are assumed.

4.3 Loss of information in Poisson spike trains

Before quantifying the loss of transmitted information, we investigate the spike train deformations due to axonal swelling and show how FAS can significantly alter the input-to-output spike train. The propagation effects are then quantified by constructing confusion matrices and computing the loss of TI through the function H.

4.3.1 Spike trains before and after axonal swelling

The goal of this subsection is to quantify how much a spike train changes after propagating through an axonal swelling. Factors such as the size (length) of the spike train and its firing rate can drastically affect the outcome and will be described in details. Finally, we compare an ensemble of trains

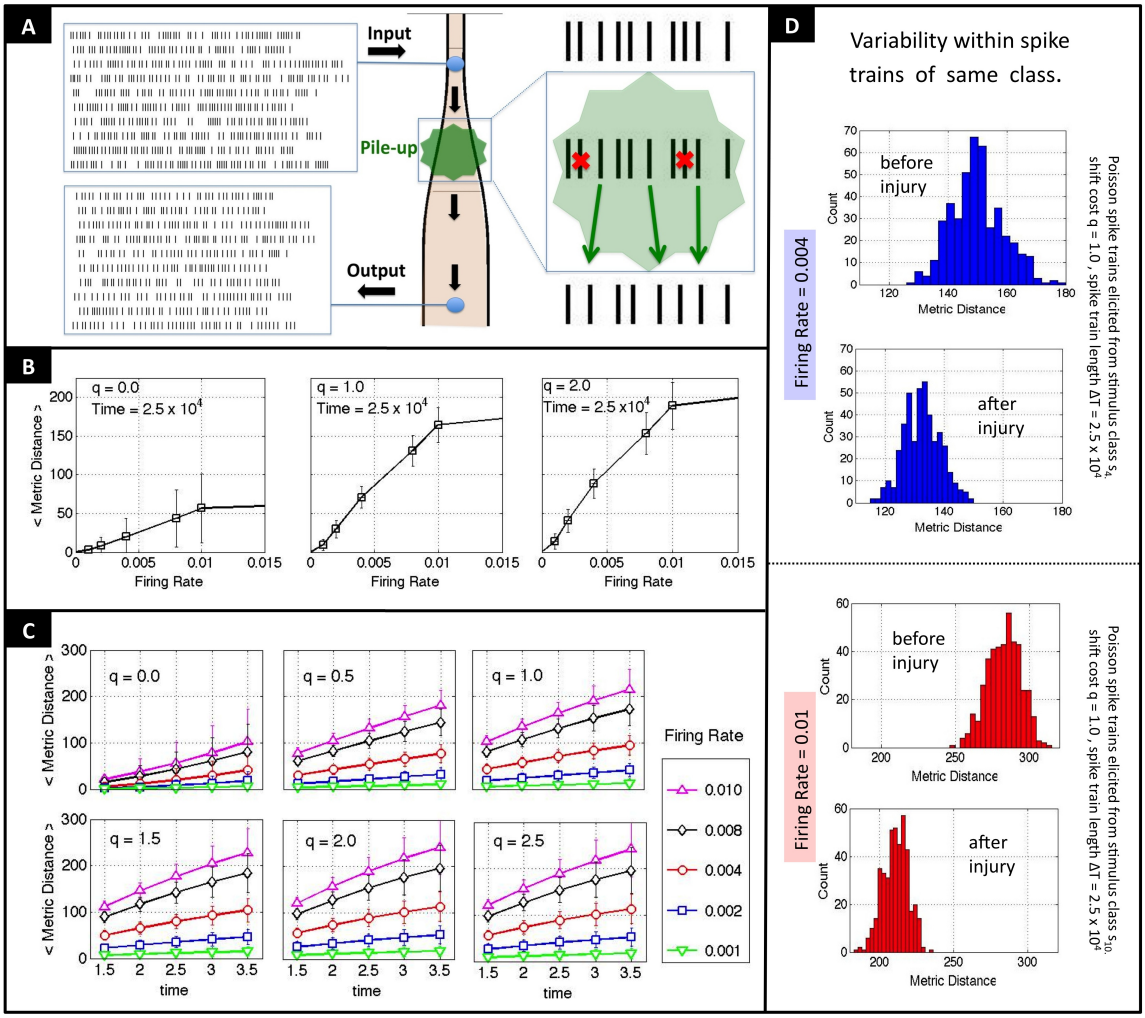

Figure 4.6: Spike metric analysis of morphological effects on Poisson spike trains for a prototypical axonal enlargement operating in a transmission regime. Panel **A**. Schematic of simulations where some spikes are deleted by Pile Up collisions (red x) or shifted (green arrow). Panel **B**. Plots of Average Metric Distance (AMD) between spike trains before/after enlargement for different Firing Rates (FRs). Bars represent one std. dev. above and below average. Temporal length of trains are fixed ($\Delta T = 2.5 \times 10^4$ non-dimensional units). Metric values depend strongly on the shift cost q associated to the metric calculation. Panel **C**. Temporal scalings of AMD for different FRs and shift costs q. Panel **D**. Comparison of the variability within a single stimulus class of moderate firing rate s_4 (FR=0.004 non-dimensional units) and of high firing rate s_{10} (FR=0.01) before/after being reshaped by the axonal swelling. Shown are histograms of metric distances between train i and j within each class.

Table 4.2: Examples of classification matrices

Ex. 1	r_1	r_2
s_1	40	0
s_2	0	40

Ex. 2	r_1	r_2
s_1	37	3
s_2	2	38

Ex. 3	r_1	r_2
s_1	22	18
s_2	15	25

Ex. 4	r_1	r_2
s_1	20	20
s_2	20	20

Examples of classification matrices for 40 trains elicited by two stimulus classes. The diagonal matrix **1** has perfect or total TI, and since there are only two classes, H = $\log_2 2 = 1$. Matrix **2** is near-perfect with H = 0.664. Matrix **3** is near-random, because the off-diagonal terms are slightly smaller than the diagonal terms and have H = 0.022. Matrix **4** is totally random and have H = 0.000.

(with different firing rates) before and after the injury and demonstrate that they collectively become more similar.

In Panel **A** of Fig. 4.6 we display the setup for these simulations: Poisson spike trains with different Firing Rates (FRs) are used as input. Effects such as those described in Section 4.1 (spike shifts and pile-up collisions) take place and reshape the train. After recording each spike train in our sample before and after the swelling we follow the procedure described in Sec. 4.2.1 and calculate the metric distance between them.

In Panel **B** of Fig. 4.6 we plot the average of these metric distances (AMDs) as a function of the FRs. The bars indicate one standard deviation above/below the mean. The trains have a fixed temporal length ($T = 2.5 \times 10^4$ non-dimensional units) before/after being reshaped. For low FRs, the inter-spike intervals are (on average) very large and most of the spikes propagate independently from each other. Thus, their AMD between original/reshaped train is low for all shift cost values q since nontrivial interactions between spikes are rare. As the FRs increase, spikes are more likely to experience changes and/or deletions, leading to an increase of AMD. Finally, for higher FRs the number of spikes in a train reaches a limit due to the refractory period of the system that constrains how fast another spike can be formed, i.e. the low-pass filtering effects of the axon morphology

plays a role. With no additional spikes to be shifted or deleted, the AMD reaches a plateau.

In Panel **C** of Fig. 4.6 we depict how the AMD scales with the (temporal) length of the spike trains for different FRs and shift costs. The scalings are linear as a consequence of the memoryless property of Poisson trains: the AMD of an entire train is the sum of the AMD of its segments. We note that the trends for the AMD are better separated for larger values of q.

To account for the variability, not just average values, we display in Panel **D** of Fig. 4.6 the histograms of the metric distances between spike trains of same FRs before and after the axonal injury. We compare the variability within a single stimulus class of moderate firing rate s_4 (FR=0.004 non-dimensional units) and of high firing rate s_{10} (FR=0.01). The histograms show that the morphological injury acts by squeezing and shifting the distributions towards lower values of distances (left), with the effect being more pronounced for the higher FR. Ultimately, variability in the stimulus class is reduced in both cases due to the axonal deformations.

4.3.2 Confusion matrices for injured neurons

Here we extend the classification procedure from [117] to injured neurons. More specifically, to axonal swellings that affect spike train propagation without completely blocking them. The results are displayed in Fig.4.7.

In section 4.2.2, we reviewed how to use a classification matrix to assess how informative a neuron's response is. The classification is perfect (or most informative) when all spike trains elicited by the same stimuli are assigned to the same response class by the metric criteria. A perfect response is associated to a strictly diagonal matrix (see Fig 4.1A and Table 4.2). Conversely, a non-diagonal matrix is associated with less separated, and thus less informative, response classes. Our simulations show that an axonal swelling distorts the *separation structure* of the neural response.

Some key points of our method include:

1. An axonal injury is regarded as a second set of stimuli acting on top of the elicited spike trains, and its effects are viewed *relative* to the original response classes.

2. There are two sets of spike trains: the original, or control, (before injury) and the modified, or reshaped, (after injury). The same distinction is valid for response classes.

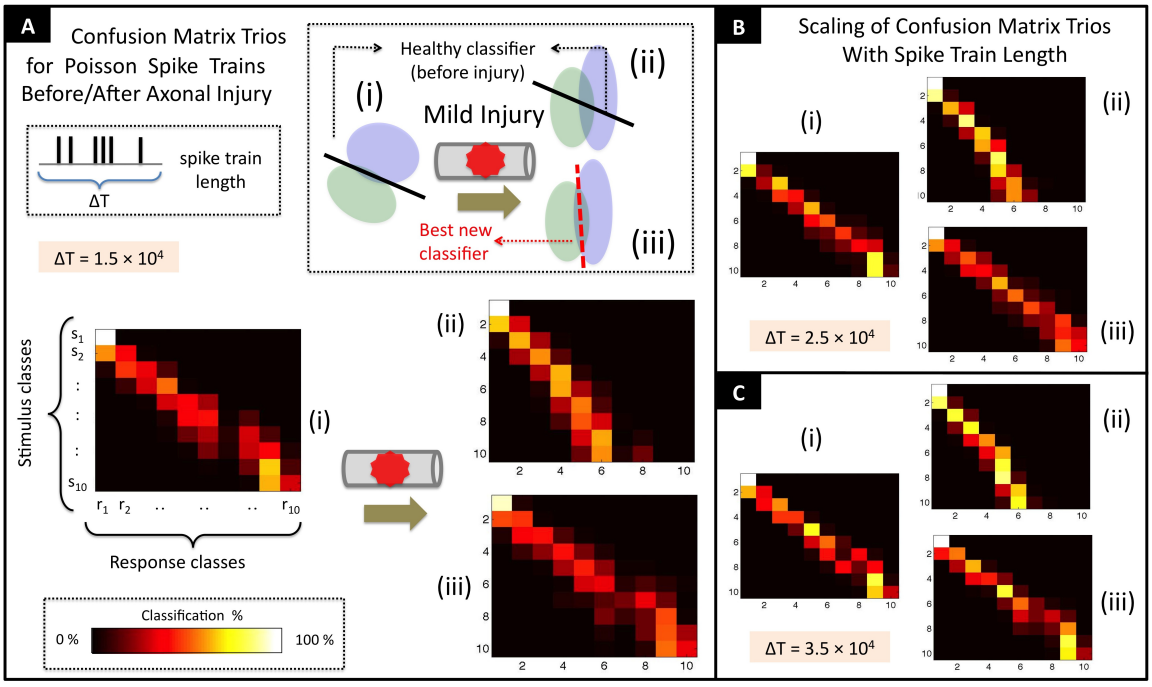

Figure 4.7: Confusion matrix trios. We considered 10 stimulus classes $s_1, \ldots, s_{10}$, where each s_j is associated to a different Poisson Firing Rate λ_j. Each s_j generates multiple (40) spike trains that are then classified to a response class r_k. If $k = j$, it is correctly classified and a contribution is made to the diagonal of the confusion matrix. If $k \neq j$, then it is misclassified and contribution is made to an off-diagonal (α_{kj}) element of the confusion matrix. Each confusion matrix trio is comprised of (i) Classification before the axonal injury with healthy classifier (top left matrix of every trio), (ii) Classification of reshaped spike trains after propagating through the axonal swelling with healthy classifier (top right matrix of every trio), and (iii) Classification of reshaped spike trains with a new classifier that optimally separates the response classes in the injured axon (bottom right matrix of every trio). The different panels show confusion matrix trios when the length (size) of the spike trains in the sample increases. In Panel **A** the length is 1.5×10^4 non-dimensional time units, in Panel **B**, the length is $\Delta T = 2.5 \times 10^4$ and in Panel **C**, $\Delta T = 3.5 \times 10^4$.

3. Since classification matrices for injured neurons provide information about errors in the encoding-decoding scheme, we will refer to them also as *confusion matrices*.

4. Confusion matrices form a *trio*: (i) the original (non-injured) classification matrix with the original metric criteria, (ii) the matrix for reshaped trains with the original metric criteria, and (iii) the matrix for reshaped trains with a new metric criteria. See Panel **A** of Fig. 4.7.

In our simulations (see Figure 4.7), we consider 10 stimulus classes acting before the injury s_{1B}, $s_{2B}, \ldots, s_{10B}$. Each class denotes a Poisson Train Generator with non-dimensional units of Firing Rates (FRs) $\lambda_1 = 0.001$, $\lambda_2 = 0.002$, ..., $\lambda_{10} = 0.010$. We sample 40 spike trains from each class and classify them in response classes before the injury r_{1B}, r_{2B}, ..., r_{10B}. These are depicted in matrix (i) of each trio in Fig. 4.7. Since the injury did not affect the spike trains until this point, the procedure to obtain theses classification matrices is the same as the one discussed in Section 4.2.2. The leftmost matrices are not perfect (diagonal) since some trains elicited from s_j are closer (by the metric criteria) to trains in r_{j-1} or r_{j+1} instead of r_j. As a consequence, the matrix is approximately tridiagonal. The classification improves as the length of the spike trains increase since the width of the diagonal structure decreases. The pre-injury classification matrices for Poisson trains are compatible with the spike metric examples in [117]. We used a shift cost $q = 0.02$ for all classifications to be compatible with the typical spike shifts observed in the FitzHugh-Nagumo model.

The spike trains then propagate through the injury where the deleterious effects of the axonal swelling described in Section 4.1 take place. In Fig.4.7, the resulting confusion matrices (ii) and (iii) in each trio show how injured neurons compromise the stimulus class discrimination.

In matrix (ii) of every trio in Fig. 4.7, each reshaped spike train (after injury) is now compared with the original trains (before injury) for classification purposes. Aside from this change, the classification criteria is the same as before. We observe that there is a dramatic distortion in the diagonal structure of the matrix. This occurs because spike trains with higher FRs lose spikes largely due to pile-up collisions and are confused with spike trains of lower FRs. The last row of the top-right matrices, for example, shows that modified spike trains elicited by s_{10} with $\lambda = 0.010$ (non-dimensional units) are heavily confused with original spike trains from r_{6B} with $\lambda = 0.006$. Therefore, the higher the FR of a spike train, the more susceptible it is to misclassification after axonal swellings (false positive). Conversely, lower FRs are more reliable. This observation

is simply a manifestation of the low-pass filtering expected of FAS. We discuss the biophysical consequences of this in Section 4.4.

In matrix (iii) of every trio in Fig. 4.7, each reshaped spike train (after injury) is now compared with the other reshaped spike trains for classification purposes. This is a *change* in the classification *criteria* to a new optimal discrimination between classes. The confusion matrix still presents some diagonal structure, but with larger width than the leftmost matrix. However, there is a significant improvement compared with the top right matrix. An important consequence is that the overall error in the encoding-decoding process can be reduced in injured neurons if the classifier learns, perhaps through plasticity, a new metric criteria tailored for the reshaped spike trains. We discuss how this idea can lead to different strategies for the neuron's functional recovery in the last section.

4.3.3 Relative Loss of Transmitted Information

In the previous section, we discussed qualitative aspects of the confusion matrix trios displayed in Fig. 4.7. Regardless of the length of spike trains used in the sample, the post-injury matrix, numbered (ii) of each trio, exhibit dramatic distortions of the diagonal structure when the healthy/original metric classifier is used. The classification matrix can be improved however if a new metric classifier is used (see bottom right matrix of each trio). In this section, we calculate the transmission information (TI) associated with these matrices and provide a more quantitative description of the signal processing impairment in an injured axon.

Recall from Section 4.2.2 that the TI of a classification matrix $\mathbf{A}$ is given by equation (4.1). Intuitively, it is the quantity that captures how much the association of the response-to-stimulus classes is informative (or non-random). The calculation penalizes non-perfect (non-diagonal) matrices proportionally to the magnitude of its off-diagonal terms.

In Figure 4.8, we display the TI for the confusion trios of Fig. 4.7 along with a variety of intermediate spike train lengths. Each matrix (within a trio) is colored according to its position/-function (as in Figure 4.7): (i) Black squares for the leftmost matrices, i.e, the healthy classification matrices for spike trains before the injury. (ii) Blue circles for the top-right matrices, that classify reshaped spike trains (after the injury) with the *original* classification criteria. (iii) Red triangles for bottom-right matrices that classify reshaped spike trains (after the injury) with the *new* classification

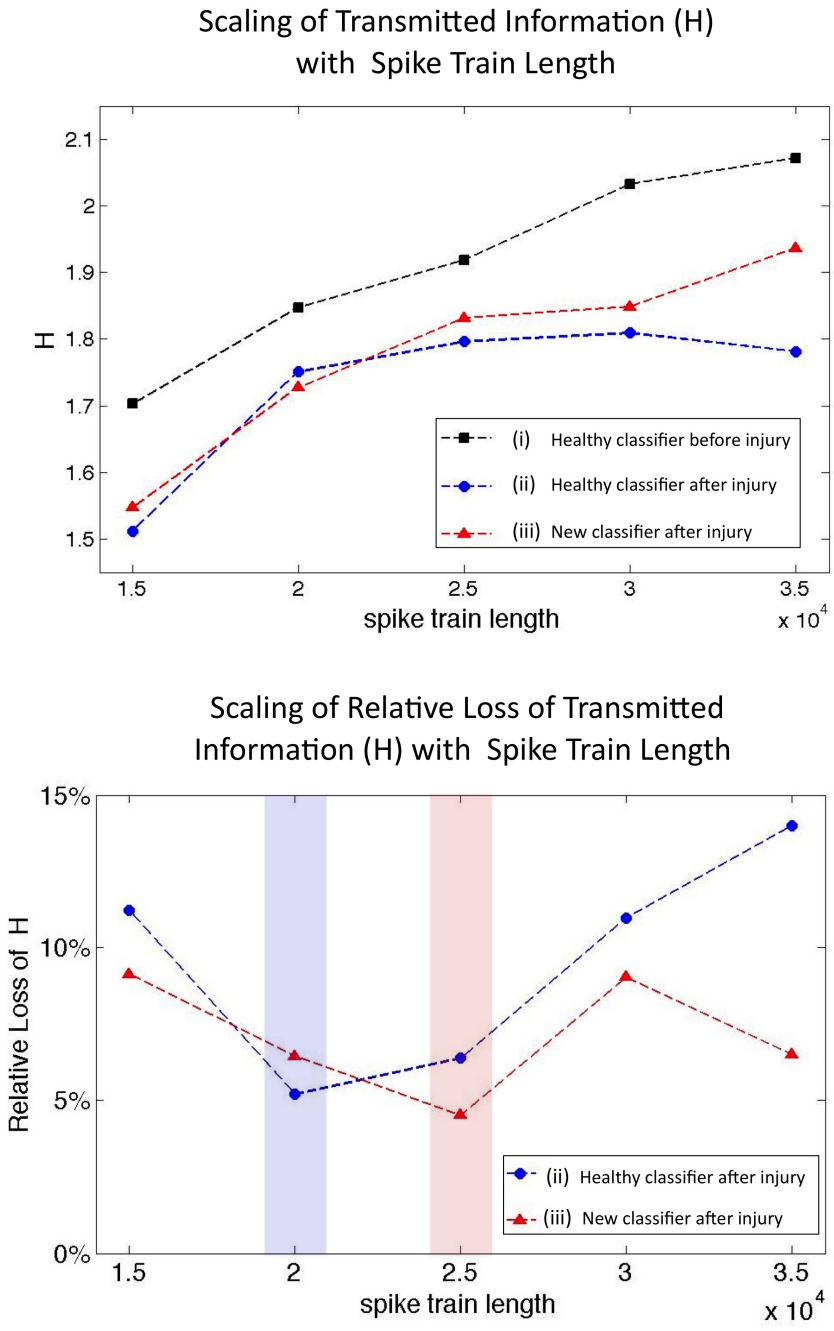

Figure 4.8: Top panel: Computation of transmitted information H for confusion matrix trios as a function of spike train length (non-dimensional units). Bottom Panel: Computation of relative loss of H after injury as a function of spike train length (non-dimensional units). For both panels, indexes (i), (ii) and (iii) have the same meaning as in Figure 4.7. Note that learning of a new classifier is advantageous provided that meaningful information is encoded in longer spike trains.

criteria.

In the top plot of Fig. 4.8, we note that there is loss of transmitted information after the injury, regardless of the size of the spike trains or classification criteria. As expected from the qualitative discussion in the previous section, the TI of healthy matrices (leftmost matrices) improves as the length of the spike trains increase. The difference in H between the black curve and the others is the absolute loss of transmitted information.

The relative loss in the transmitted information is depicted in the bottom plot of Fig. 4.8. Both curves are concave-shaped starting with a loss around 10% for spike trains of length 1.5×10^4 (non-dimensional time units) and returning near the same value for spike trains of length 3.0×10^4 (non-dimensional time units). For spike train lengths above 3.0×10^4 however, the two curves diverge: the curve that uses the original classifier (blue) keeps increasing while the curve that uses the new classifier (red) decreases. There is a large discrepancy between the two curves in this region, and the one associated to the new classifier performs much better. In fact, larger spike trains usually exhibit more secondary features than shorter spike trains. The injury might affect these features less then the primary features (number of spikes, etc). It is reasonable that a new classifier, that favors these more robust properties, can lead to a better classification. Thus, in a scenario where long spike trains are used for TI, the plot suggests that there is room for functional improvement if the networks learn a new classifier through neuro-plasticity, for instance. We discuss this in more detail in the next section.

The concave-shaped curves in the bottom plot of Fig. 4.8 have distinct minima: spike train lengths of 2.0×10^4(non-dimensional time units) minimize the relative loss of TI for the blue curve (see blue stripe) and lengths of 2.5×10^4 minimize it for the red curve (see red stripe). The minimum for the blue curve shows the length for which the number of misclassifications in the spike train is the smallest. The minimum of the red curve gives the lengths for which the relative loss of TI is smallest by potentially learning a new classifier.

We expected that larger spike trains would loose relatively more information: they would be better separated (law of large numbers) before injury and since the FAS affects spike train regardless of their size, there is more TI to loose. It remains an open question why small trains loose (relatively) more TI than medium sized trains, which represent the minima. Both classifiers exhibit them, suggesting that its existence might not depend on the nature of the classifier.

In conclusion, Figure 4.8 shows for our working example how the relative loss of transmitted information scales with the length (size) of the spike trains used in the sample. For smaller lengths, learning a new classifier does not improve the TI significantly, but the payoff of switching to a new classifier for longer spike trains can be significant. We believe that our example is insightful, but much study is needed to assess if these conclusions will hold for different stimulus classes and different classifiers.

4.4 Discussion of the results

This chapter introduces a theoretical/computational framework to quantify how FAS reshape spike trains, confuse responses to different stimulus classes, and lose information during transmission. As detailed in Section 4.1, many nontrivial effects can take place in the FAS, thus potentially reshaping the propagating spike train (Fig. 4.6A). We used a spike train metric analysis to quantify changes that Poisson spike trains undergo when encountering FAS, but other statistical criteria could be used as well (Section 4.2). The spike train metric analysis accounts for spike deletions and timing shifts dueto FAS and relates them to observed biophysical mechanisms (Table 4.1).

The following key observations were made:

1. Poisson trains with high FRs are impacted more than trains with low FRs. Thus spike trains with lower firing rates are more robust to axonal swellings then those with higher firing rates. This reflects the low-pass filtering that occurs under FAS, where the filter strength is increased with larger FAS.

2. In a healthy axon, only a few spike trains are misinterpreted as a response to another stimuli. This notion is captured by a strong diagonal dominance in the confusion matrix.

3. FAS lessens the separation between different response classes and many misclassifications occur. This notion is captured by a distortion in the diagonal of the confusion matrix, i.e. off-diagonal terms in the confusion matrix are accentuated (Fig. 4.7).

4. TI always decreases after FAS (Fig. 4.8, top plot).

5. The relative loss in TI depends on the length of the spike trains (Fig. 4.8, bottom plot).

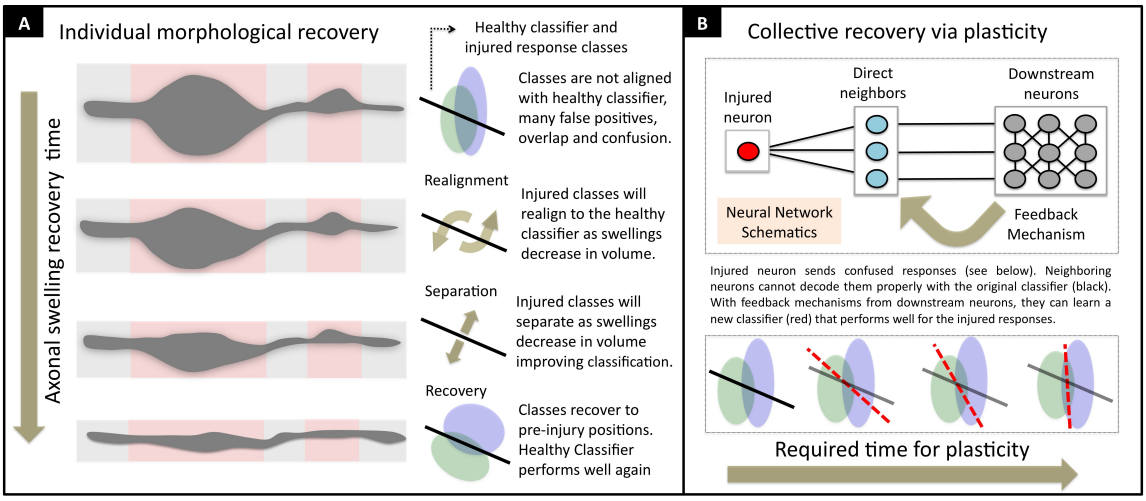

Figure 4.9: Elements of two prototypical functional recovery paradigms. **A** Individual morphological recovery, whereby the slow reduction of swelling, potentially aided by pharmacological agents, returns the axon to normal operation. **B** Collective recovery via plasticity, whereby re-weighting of neural connections leads to new population encoding vectors and a new optimal classification of stimulus.

6. With FAS leading to a potential 30-fold increase in axon diameter [108, 109], the transmission of spikes might be blocked completely with no information is transmitted.

7. Blockage can occur even in swellings of small volumes if the increase in diameter is sufficiently abrupt. Thus the geometrical tapering parameters of FAS are of utmost importance [74].

Our confusion matrices quantify the impact of a single axonal swelling in Poisson spike trains and also demonstrates low-pass filtering their firing rates. We remark however that an injured axon most likely have multiple FAS, each with different geometrical tapering parameters; This can add significant complexity to spike propagation dynamics. Thus, even in a very simplified scenario – where the varicosities are assumed to be of the same material as the axoplasm – it is unclear what the combined effect of multiple FAS will be. At this point, the available biophysical information is insufficient to understand potential changes in the resistivity of the axon after injury. Many varicosities contain mitochondria (that regulate presynaptic Ca+2) or other electrically active vesicles that can interact with propagating spikes. We hope to improve the computational modeling of FAS presented here with features from future experimental advancements .

4.5 Insights to recover the functionality of injured neurons

A better theoretical understanding of the effects of axonal injuries to spike encodings can lead to novel strategies to recover the functionality of injured neurons, ultimately leading to biophysical schemes for suppressing the deleterious effects of TBI and/or other neurodegenerative diseases. We imagine at least two broad directions:

1. Individual morphological recovery through natural healing and/or pharmacological agents (Fig. 4.9A)

2. Collective recovery via neuro-plasticity (Fig. 4.9B).

In the first type (Fig. 4.9A), the axonal swelling would decrease naturally [80] or by responding to some pharmacological treatment [52]. While injured, the neuron's response classes would not be aligned with the original/healthy classifier. Instead, the response classes would have significant

overlap, leading to increased confusion and misclassifications. As the axonal swellings decrease in volume, the response classes would realign and separate as the FAS returns to its healthy state. Finally, the response classes would return to their pre-injury position and the healthy classifier would perform well again.

The second type (Fig. 4.9B) is a collective (network) strategy to circumvent the confusion caused by a neuron with persistent axonal swellings. The injured neuron would keep sending reshaped spikes trains to their direct neighbors. However, due to feedback mechanisms in the network, the neighboring neurons would learn (via plasticity) how to re-interpret these reshaped spikes. Specifically, by learning a new classifier, or criteria, (in red) instead of the healthy/original classifier they used before the injury. Figure 4.8, for instance, shows how the relative loss of transmitted information scales with the length (size) of the spike trains used in the sample. For smaller lengths, learning a new classifier does not improve the TI significantly, but the payoff of this recovering strategy can be tremendous for large lengths.

The different strategies are not exclusive, and perhaps the optimal treatment would combine them. Thus, the *time scales* of individual recovery and collective (plasticity) recovery are of extreme importance. We would not wish the two mechanisms to work against each other, i.e. attempt to return a neuron to its original response classes (pharmacologically) when the rest of the network is trying to learn a new classifier for the reshaped spire trains.

As a next step in this study, we wish to extend our computational studies to neural networks. If we add injured neurons with different FAS in a network, how would it affect the population codes? Can the confusion matrices developed in this work be used to update the *effective* firing rate of injured neurons? We believe that such computational models can bridge the observed changes in the single cell level to the functional deficits observed in behavioral and cognitive studies of patients and animals exposed to concussion, traumatic brain injury, and other neurodegenerative diseases such as Alzheimer's and Parkinson's disease.

Acknowledgements: We are especially grateful to Bingni Brunton, Steven Brunton, Borna Dabiri and Matthew Hemphill for discussions relating to the filtering and functionality of the injured axons. We also thank Eric Shea-Brown, Ben Lansdell and Alex Cayco-Gajic for helpful discussions relating to this work.

Chapter 5

BUILDING A COMPUTATIONAL TOOLBOX FOR FAS DIAGNOSIS

In this chapter we develop a computational toolbox that extracts meaningful geometrical parameters from sequential images of injured axon segments. The algorithm provides a principled approach for dealing with imaging distortions caused by experimental artifacts in order to extract the cross-section of an axon by detecting local symmetries, turning points and turning regions. The characterization of FAS allows for an assessment of its impact on spike propagation, leading to a color coding of the axon that highlights problematic regions for information propagation. Our MATLAB toolbox thus highlights potential trouble spots of axonal morphology, and similar to car traffic maps, identify blocked or impaired routes for information flow.

Until now we characterized the propagation of spike trains in FAS by evaluating the parameter $\eta(\delta_B, \delta_T, \delta_A)$ with highly idealized geometric structures. Real axons have much more challenging geometries then the idealized case, thus requiring further innovations around how to process their structure. In this chapter we develop algorithms to deal with the complications of more realistic structures in a principled way. Our goal is to extract the required geometrical parameters from axonal images and color-code FAS according to how severely they are expected to jeopardize the transmitted information. The effects of injuries in the neuronal network are visualized much like live traffic maps that indicate blocked and/or congested roads.

To demonstrate the method, we applied our MATLAB toolbox to small samples of (i) uninjured hippocampal rat neurons with rich geometrical structures [102] and (ii) some of our own in vitro injured axons from magnetic-twisting cytometry experiments. Figure 5.1 shows in detail some of the axons that are used for quantifying the effects of FAS. The figure also shows how the methodology presented can be used as an evaluation tool for quantifying the statistical distribution of swellings, thus providing a neuronal traffic map of signal propagation (or transmitted loss) for individual axons as a function of time. Specifically, areas of compromised information transmission are color coded

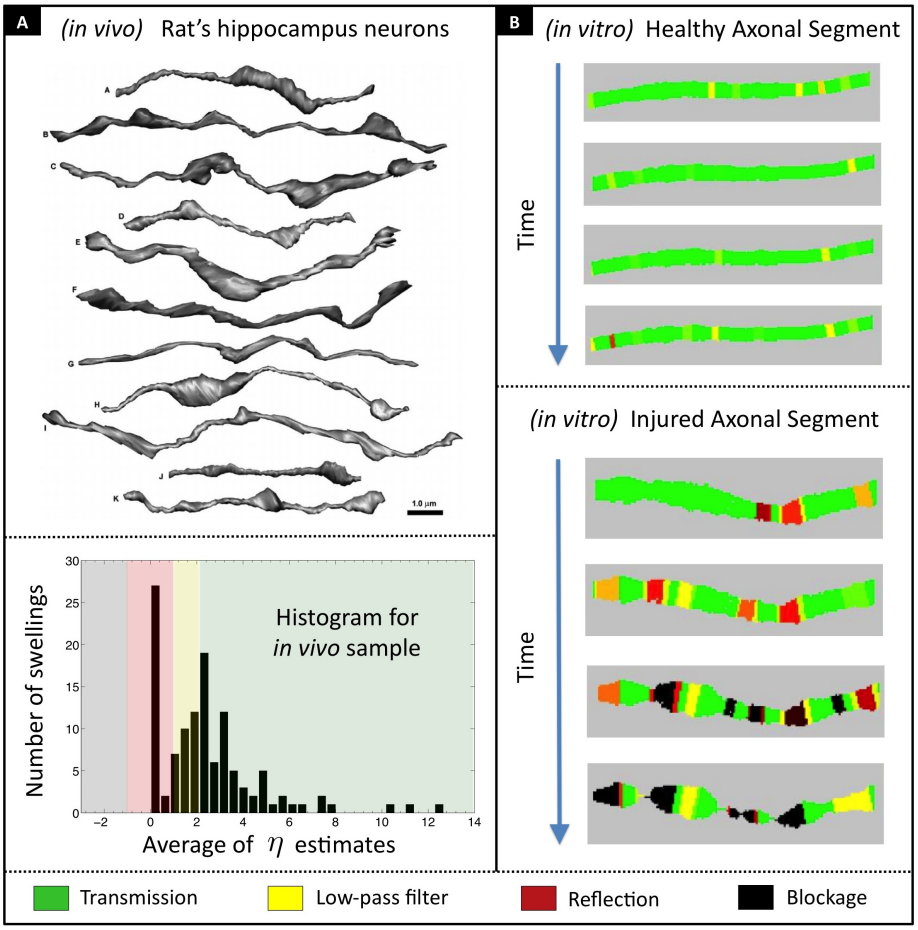

Figure 5.1: Panel **A**. Membrane contours for reconstructed unmylienated axon segments of CA3 $\rightarrow$ CA1 rat Hippocampal neurons. Courtesy of *SynapseWeb*, Kristen M. Harris, PI, from [102]. Below, we show the corresponding swelling distribution among different functional propagation regimes (transmission, low-pass filter, reflection and blockage). Panel **B**. Typical evolution of swellings in healthy and injured axonal segment. *In vitro* injury experiments performed by Dr. Matthew Hemphill at Disease Biophysics Group, Wyss Institute for Biologically Inspired Engineering, Harvard University.

from yellow, to red, to black depending upon the level of injury. It also shows that information propagation changes as a function of time as swellings grow. Figure 5.1B represents the key diagnostic tool achieved in this work. A full quantification of the axon shaft is demonstrated, where traffic congestion maps inspire a novel representation of the deleterious effects of FAS.

We expect this toolbox to be of broad interest to the neuroscience, neurological and biomedical engineering communities due to the critical role that focal axonal swellings play in modulating the transmission of information in traumatic brain injuries and/or neurodegenerative diseases.

5.1 Extracting geometrical features from real axon segments

To evaluate the critical parameter η across an axonal segment, the geometrical features of a given axonal swelling must be extracted from a time sequence of axonal images. As a first step, we apply techniques from statistical shape analysis to fix distortions caused by experimental contrast issues in the image acquisition. After accounting for the distortions, we then extract the axonal cross-section.

5.1.1 Shape comparison after Procrustes superimposition

It is customary during *in vitro* axonal injury experiments (see Figure 5.1B) to take image snapshots at regular time intervals to monitor the formation of Focal Axonal Swellings and keep track of how each axonal process evolves [72, 52]. Many experimental artifacts however, can distort these images by introducing position shifts, image rotation and/or contrast issues. Consequently, axon processes may appear artificially larger or smaller then they should simply from image distortions (See Figure 5.2A). These distortions can lead to incorrect measurements of the geometrical parameters of the axon and consequently to a misleading FAS diagnosis. To compare the shape of two or more objects in a sequence they must be first correctly superimposed. This is achieved via a Procrustes analysis which optimally translates, rotates and scales the compared objects. Figure 5.2B shows some simple examples of how the analysis accounts for the translation, rotation and dilation of two exemplar objects.

In statistical shape analysis, a *shape S* is defined as a collection of data points where their cartesian coordinates are stored in a matrix. In the context of an axon, it refers to all the points comprising

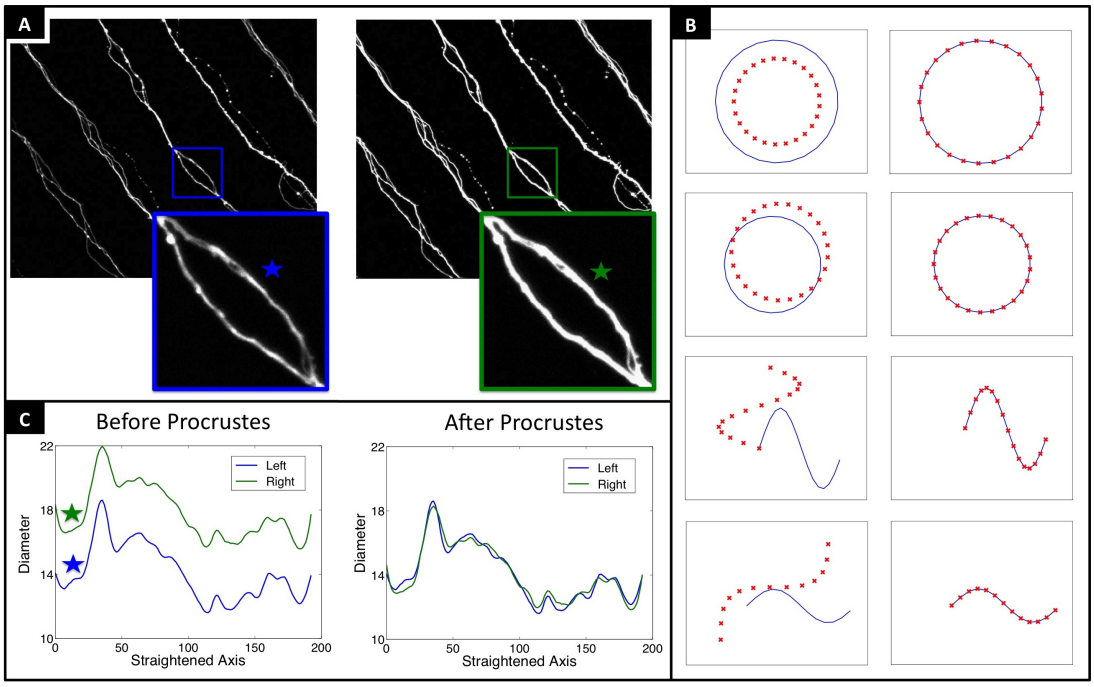

Figure 5.2: Shape comparison after Procrustes superimposition. Panel **A**. Pictures taken with a five minute interval display contrast problems from experimental artifacts. The right zoomed segment (green) appears larger than the left zoomed segment (blue) even if no significant biological change occurred. Panel **B**. Procrustes superimposition is an algorithm in statistical shape analysis that can be used to align shapes via scaling, shifting, rotation and/or a combination of such effects. Panel **C**. By applying Procrustes superimposition to the highlighted segments, we obtain the optimal factors to correct the contrast issues. See section 5.1.1 for details.

the axon segment and/or its contour. To optimally superimpose shape S_A to shape S_B we minimize what is called the Procrustes distance between these objects:

$$\begin{aligned} &\text{find} && \text{scaling factor } b>0, \text{ a rotation matrix } R, \text{ and a shift vector } c \\ &\text{to minimize} && ||S_B - b\cdot S_A \cdot R + c||_2, \end{aligned} \tag{5.1}$$

where the goodness-of-fit criterion is the sum of squared errors. This step significantly improves images for posterior analysis. Figure 5.2C exemplifies a contrast issue successfully resolved using this least-square optimization procedure.

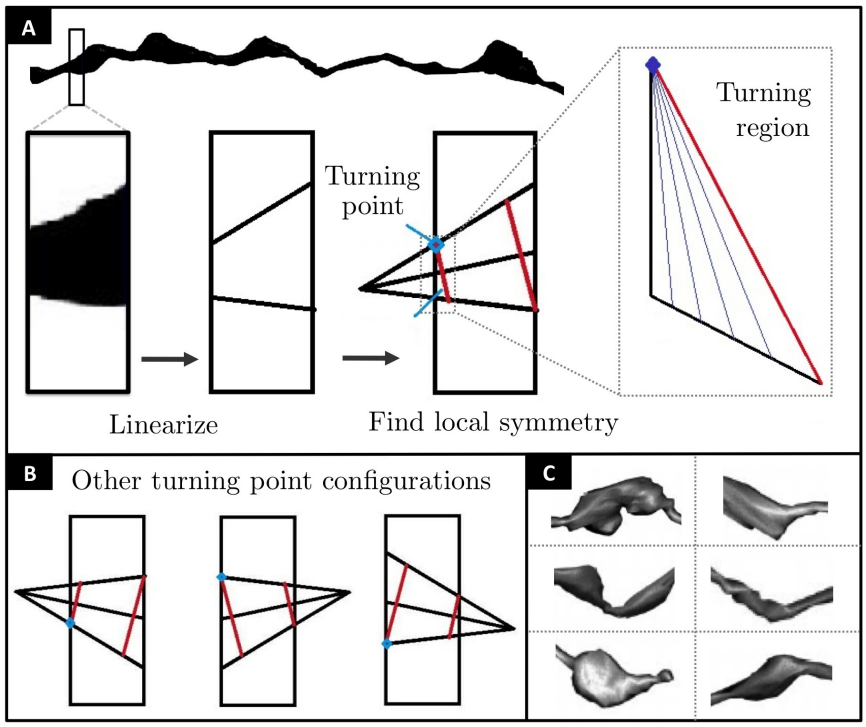

Figure 5.3: Extracting axonal cross-section. Panel **A**. Axonal contours are approximated by patched trapezoids. A non-symmetric trapezoid can be decomposed into a turning region (zoomed) and a symmetric trapezoid (red). One of the vertices is the turning point. Panel **B** shows other turning point configurations. The algorithm of section 5.1.2 handle nontrivial enlargements such as those in Panel **C**.

5.1.2 Extracting axonal cross-section

The next step of our shape analysis extracts axonal cross-sections from the captured images by using a principled algorithm outlined here and depicted in Fig. 5.3:

1. Pre-process each image to prune individual axon segments and reduce imaging noise. Convert the image to a grayscale data matrix M_{ij} whose entries vary between zero (black) and one (white). Enhance contrast by applying a threshold τ, i.e., set

$$M_{ij} = \begin{cases} 0 & \text{if } M_{ij} < \tau, \\ 1 & \text{if } M_{ij} > \tau. \end{cases}$$

2. Locate upper and lower axonal contour points by verifying neighboring entries in M where there is a transition from black to white and vice-versa.

3. Approximate the axon segment with patched *trapezoids*, each composed of two vertices in the upper axonal contour and two from the lower axonal contour. The problem is now reduced to extracting the cross-section of each trapezoid.

    - If the trapezoid is symmetric the discrete cross-section values are simply the segments connecting the upper contour vertices to the lower contour vertices.
    - If the trapezoid is non-symmetric, it can be decomposed into a *turning region* patched to a symmetric trapezoid. One of the vertices is the *turning point*. Our cross-section linearly interpolates the turning region until the start of the symmetric trapezoid component. See Fig. 5.3A for details.

In Figure 5.3B we display three prototypical configurations of turning points and turning regions. Thus the method can extract the geometrical features associated with non-trivial axonal sections such as those of Fig. 5.3C. We remark that there is a simple criteria for determining which vertex is the turning point. As illustrated in Fig. 5.4A, there are two left angles $[\theta_u, \theta_l]$ associated with a non-symmetric trapezoid. The turning point is always *opposite to the larger angle*. By approximating an axon with a set of turning regions patched to symmetric trapezoids, we can systematically extract its cross-section. The algorithm can be iteratively applied in order to refine the grid as necessary. Figure 5.4B applies the algorithm to a typical axon segment and the results are illustrated for this process.

5.2 Characterizing propagation in real axons

By using the extracted cross sections of the axonal geometry, such as the one in the bottom panel of Fig. 5.4, the FAS can be characterized along the axon segment.

The characterization of the axon segment is done by evaluating the parameter $\eta(\delta_B, \delta_T, \delta_A)$ as a function of distance down the axon. However, the effects of η were associated with the highly idealized geometric structure of Sec. 7.1. Real axons have much more challenging geometries then

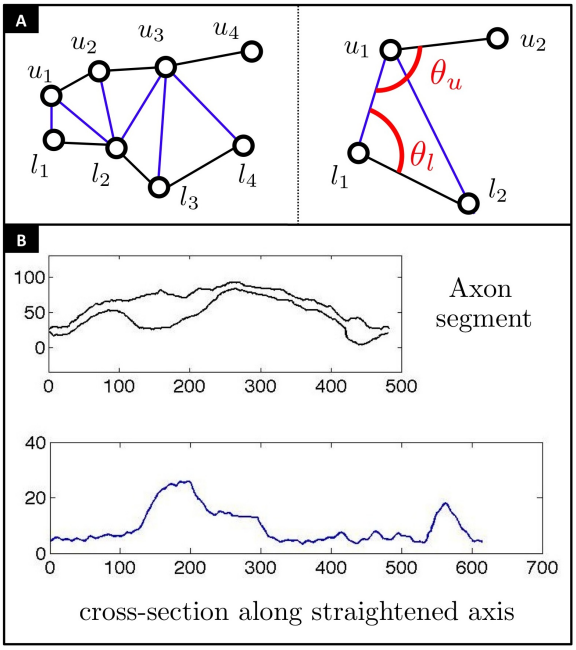

Figure 5.4: Criteria to find the turning point. Panel **A** depicts the left angles $[\theta_u, \theta_l]$ associated to a non-symmetric trapezoid with vertices $\{u_1, u_2, l_1, l_2\}$. The turning point is always the vertex *opposed to the larger angle*. Panel **B** show a typical result of the axonal cross-section extraction algorithm of section 5.1.2.

the idealized case, thus requiring further innovations around how to process their structure. The following algorithm is a principled way to deal with the complications of more realistic structures.

Sliding windows: The idea behind this method is to slide parameter-extracting windows of various sizes along the axonal cross-section plots. This technique is reminiscent of a windowed Fourier transform where time-frequency localization can be computed with a spectrogram. Here, the sliding window is used instead to capture FAS events and the geometrical associated with them. See Figure 5.5A for an example. As the window slides, it follows some rules to extract $[\delta_B, \delta_T, \delta_A]$ from the portions of the axonal diameter $d(x)$ contained in it. Specifically:

1. Set the length L of the parameter-extracting window and let $d_{max} = d(x_{max})$ be the maximal diameter value contained in $[x, x+L]$.

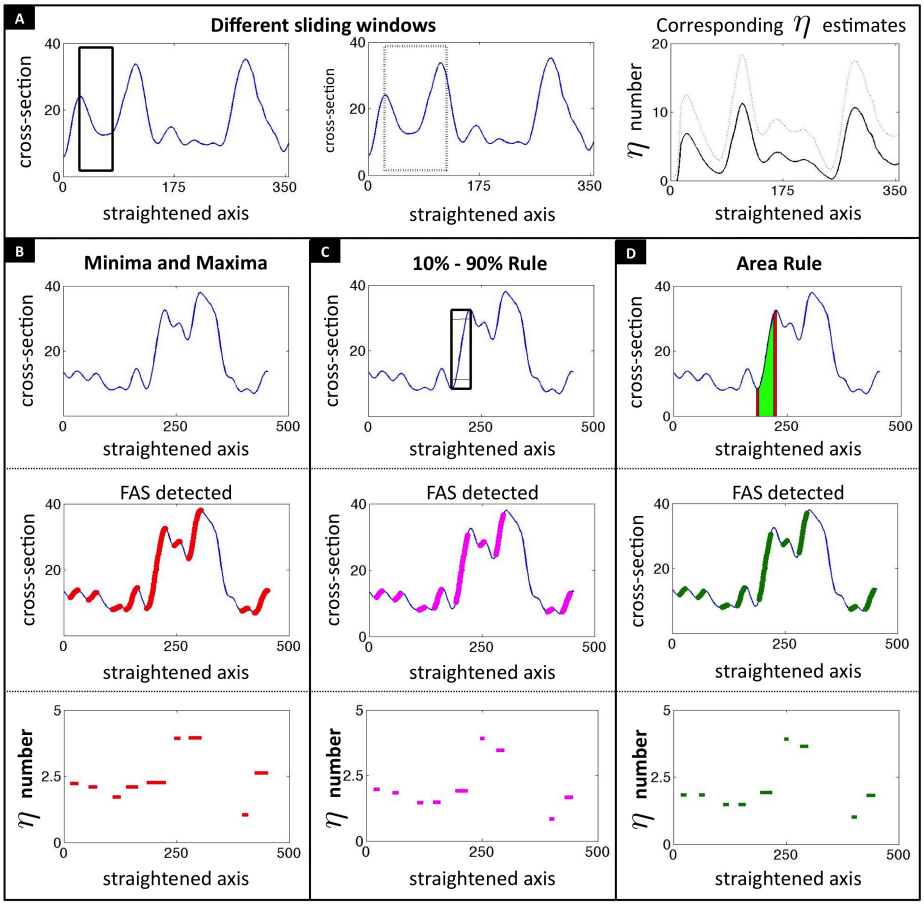

Figure 5.5: η estimates from axonal cross-sections. Panel **A** illustrates the *sliding window* method with two window sizes and their corresponding η estimates. Panel **B** illustrates the *minima/maxima* method with the axonal cross-section (top), swelling locations (middle) and the corresponding η estimates (bottom). Panel **C** illustrates the *10%-90% rule* regarding total diameter change and Panel **D** the same rule regarding total area change. Panels **C-D** show the axonal cross-section (top), swelling locations (middle) and the corresponding η estimates (bottom).

2. If x_{max} is the first point in the window, set

$$\delta_B = d_{max}, \;\; \delta_T = L, \;\; \text{and}, \;\; \delta_A = d(x+L),$$

otherwise, set

$$\delta_B = d(x), \;\; \delta_T = x_{max} - x, \;\; \text{and}, \;\; \delta_A = d_{max}.$$

As we slide the parameter-extracting window, η is continuously calculated along the axon segment. Estimates of η vary considerably with the window lengths (see Figure 5.5A); larger windows can contain multiple FAS whereas smaller windows may not capture an entire swelling due to the limited window size. The method may also handle swollen and non-swollen regions of the axon indistinguishably.

Minima and Maxima: To refine the estimates above, we recalculate η for each FAS. They are located by properly pairing the extrema of the diameter function, with each swelling starting at a local minimum x_{min} and ending at the next local maximum x_{max}. Then, we assign for each located swelling:

$$\delta_B = d(x_{min}), \;\; \delta_T = x_{max} - x_{min}, \;\; \text{and}, \;\; \delta_A = d(x_{max}).$$

Constant values of η for each swelling provide clearer diagnostic interpretations (see Figure 5.5B). This method works well for swellings with linear diameter growth but might fail for those with sigmoid shapes. If the detected swellings include large flat sections of the axonal diameter, δ_T can grow disproportionately to δ_A and δ_B. Since flat regions are not expected to interfere significantly with the propagating signal [74], it helps to trim them off from the detected swellings.

The $10\% - 90\%$ **rule:** To revise the swelling's endpoints, we borrow an idea from electronic signal processing [77]: we set the left and right limits where the total diameter increase – or total area increase – reaches 10% and 90% respectively, hence the name of the rule. The η estimates are now calculated from the revised endpoints (see Figures 5.5C and 5.5D). The two variants of the rule agree in the majority of cases and return values of η typically smaller than the other methods.

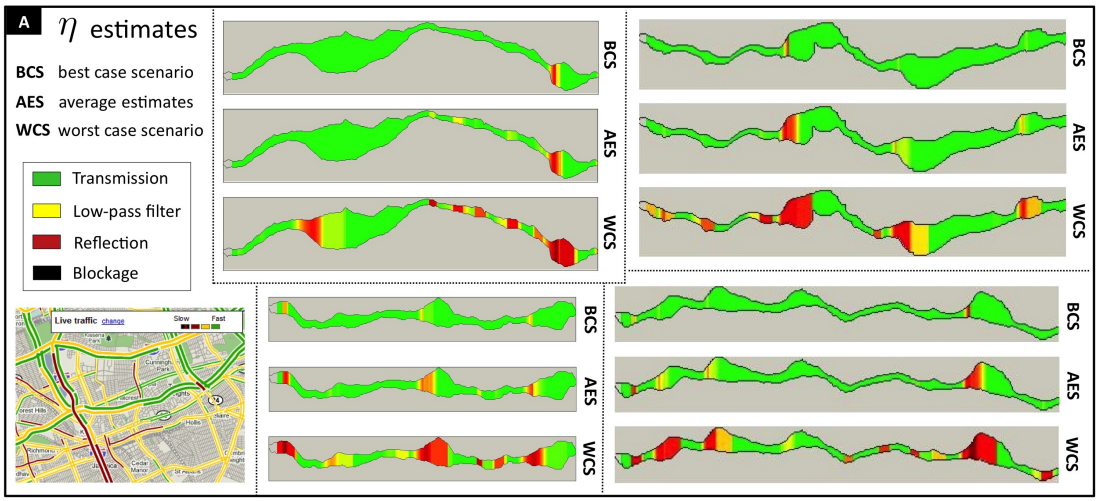

Figure 5.6: Four axon segments modified from *SynapseWeb*, Kristen M. Harris, PI, from [102]. Each axon segment is color-coded spatially according to the propagation regime number η. Different criteria lead to different η estimates, and there are multiple ways to integrate them: best case scenario (BCS), average estimates (AES) and worst case scenario (WCS). These plots are analogous to car traffic maps (bottom left) that can identify blocked or impaired routes for signal flow. This framework could lead to important improvements in FAS (cognitive deficit) diagnostics and to our understanding of the several pathologies in which they are implicated.

Combining estimates: These algorithms produce a set of η estimates which we combine in different ways: (1) best-case scenario, (2) worst-case scenario and (3) average estimates. In the best/worse case scenario we overwrite sliding window estimates with those taken from the extrema and/or $10\% - 90\%$ rules. In the third case, we average all estimates along the axonal axis. These various estimates for η are pursued in order to provide a more robust measure of the effects associated with FAS.

5.3 Completing the FAS diagnostics

Our combined algorithms color-code swellings along axonal segments as displayed in Figure 5.6; we show four axonal segments from the set of *SynapseWeb*, Kristen M. Harris, PI, from [102]. The plots are analogous to traffic maps that depict congested areas of traffic by color coding. Specifically

this traffic map can identify – for spike train encodings and signal flow – blocked or impaired routes. One should simply keep track of where the color changes from green to yellow (filtering of spikes), to red (spike reflection), or to black (spike blockage), in order to identify regions where transmitted information is lost.

We used three different criteria to combine the multiple η estimates: best case scenario (BCS), average estimates (AES) and worst case scenario (WCS). They can differ significantly in the assessment of the propagation regimes; However, having multiple ways to combine η estimates allow more flexibility to calibrate our geometrical measurements to the specific physiological settings of the analyzed neuron. In Figure 5.6, for example, we normalized the geometrical parameters to match the smallest cross-section value of the sample to the smallest radius of the simulations in [74]. Thus, even if the electrophysiological predictions are incorrect, one can still compare swellings of various shapes relative to each other. We believe this framework is a promising starting point for diagnosing axonal swellings implicated in several neuropathologies.

Chapter 6

HOW FAS CAN COMPROMISE NETWORK FUNCTIONALITY

In this chapter we study how Focal Axonal Swellings (FAS) occurring at a cellular level can compromise the activity of a neuronal network. In this setup, we treat neurons as firing-rate units that respond collectively to known stimuli with well-defined response patterns. As we injure neurons in the population by impairing their individual firing-rate capabilities, we reduce the network's overall ability to produce these patterns. We propose a few metrics to quantify loss of network functionality and compare the effects of different distributions of swellings in the neuronal population.

Up until this chapter, we considered neuron models sophisticated enough to include detailed geometrical axonal structure. Signal transmission was studied in the level of spikes and nontrivial propagation phenomena induced by FAS was analyzed in depth. However, it is unclear how individual impaired neurons (micro scale) can disrupt the functionality of a neural network (macro scale). To investigate the effects of FAS within a macro-level description, we make a few simplifications: neurons are now considered as single compartment units and their spike train encodings are regarded as an average firing rate. We simplify the deleterious effects of FAS to spike trains to modifications to the overall firing rate, but keep the flavor of different FAS injuries in the model.

The biggest novelty of this framework is that now neurons are *connected*. The wiring of the network is typically modeled as a connectivity matrix M_{ij} indicating how strongly neuron i is connected to neuron j, with disconnected neurons yielding $M_{ij} = 0$. The connections can also have different signs, exciting or inhibiting other neuron's activity. Thus, a neuron's firing rate depends not only on its own internal dynamics, but also on the integrated input received from other neurons.

6.1 Neuronal network model

The modeling of neuronal networks is one of the most vibrant fields of computational neuroscience. There are hundreds of network models throughout the literature, with varying levels of complexity,

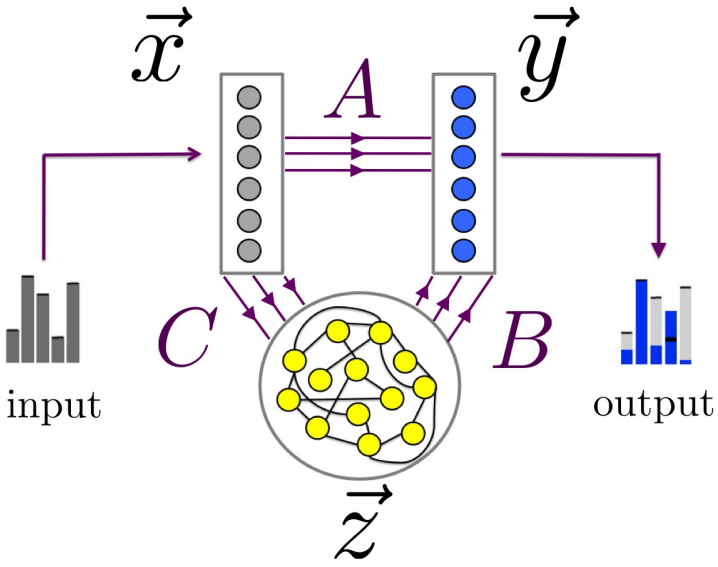

Figure 6.1: Neuronal network setup. A population of receptor neurons ($\vec{x}$) receives input from an external source. They excite the projection neurons ($\vec{y}$), which in turn, generate output encodings. Both $\vec{x}$ and $\vec{y}$ are affected by a third population of local interneurons ($\vec{z}$). The matrices A, B and C represent the strength of the connections between the neurons from different populations. See Equation 6.1 for the dynamics of the model and Table 6.1 for a full list of parameters and variables.

Table 6.1: Variables and parameters for neuronal network model

Symbol	Description	Remarks
$\vec{x}$	input/receptor neurons	N firing-rate units
$\vec{y}$	output/projection neurons	N firing-rate units
$\vec{z}$	lateral inhibitory neurons	N firing-rate units
1	time scale for dynamics of $\vec{x}$	reference
β^{-1}	time scale for dynamics of $\vec{y}$	required to achieve steady state
γ^{-1}	time scale for dynamics of $\vec{z}$	required to achieve steady state
A	connectivity matrix between $\vec{x}$ and $\vec{y}$	assumed to be known
C	connectivity matrix between $\vec{x}$ and $\vec{z}$	assumed to be known
B	connectivity matrix between $\vec{z}$ and $\vec{y}$	calibrated to match input/output patterns
E	connectivity matrix between $\vec{z}$ and $\vec{z}$	randomly connected
$\mathbf{J}(t)$	External input	usually $\mathbf{J_A}$ or $\mathbf{J_B}$
μ	noise intensity	assumed Brownian (dW)
$[\ ]^+$	linear threshold function	see Equation (6.2)

architectural configurations and capabilities. Neuronal network models are used in decision making studies, learning tasks, memory studies, control theory and others. The range of biophysical details may vary, with some systems being vaguely inspired from biological settings, to others that incorporate cutting-edge experimental measurements.

As our first network study, we merely wish to illustrate ways to introduce FAS in a setup where a clear loss of functionality can be observed and quantified. Thus, we choose the model discussed in Shlizerman et al. ([103]), originally posed to model odor discrimination in the insect antennal lobe. In this model, there are three subpopulations of neurons corresponding to different anatomical groups (see Figure 6.1): $\vec{x}$ represents the receptor (input) neurons that receives different stimuli from the environment, $\vec{y}$, the projection (output) neurons and $\vec{z}$, the local interneurons. Each neuron is modeled as a firing-rate unit and the network's dynamical equations are given by:

$$\begin{aligned} d\vec{x} &= -\vec{x}\,dt + \mathbf{J}(t)dt + \mu dW \\ d\vec{y} &= -\beta\vec{y}\,dt + \left[A\,\vec{x} - B\,\vec{z}\right]^{+} dt + \mu dW \\ d\vec{z} &= -\gamma\vec{z}\,dt + \left[C\,\vec{x} - E\,\vec{z}\right]^{+} dt + \mu dW \end{aligned} \tag{6.1}$$

The operator $[\,]^{+}$ refers to the standard linear threshold function, i.e.,

$$\left[\,s\,\right]^{+} = \begin{cases} 0 & \text{if } s \leq 0, \\ s & \text{if } 0 < s < 1, \\ 1 & \text{if } s \geq 1\,. \end{cases} \tag{6.2}$$

Table 6.1 summarizes all parameters and variables of the model. The function of this network is to produce distinguished, stable response patterns to different external stimuli. Shlizerman et al. ([103]), for example, used this model to predict neuronal responses in insects when presented to different odors. The idea is that the population of input neurons $\vec{x}$ lock onto the driving input $\mathbf{J}(t)$. In the case of constant input, the input population will converge to a fixed point $\vec{x}_0 = \mathbf{J}$. This in turn, will excite the other neural populations to produce their response patterns. We will first explore a few properties of the healthy setup and in the next sections explain in details how the injuries affect the firing rates of dynamics.

6.1.1 Low-dimensional representation of network responses

The output neuron population $\vec{y}$ can produce very different firing-rate patterns and not all of these responses are of biological interest. In fact, we are interested only in *meaningful* responses, i.e., stable and easily distinguishable patterns $\vec{y}^{P}$, thought as library elements:

$$\underbrace{L = \begin{bmatrix} \vdots & & \vdots \\ \vec{y}_1^{P} & \cdots & \vec{y}_l^{P} \\ \vdots & & \vdots \end{bmatrix}_{N\times l}}_{\text{Library}}$$

Each library element encodes a different stimuli ($\vec{y}_1^{P}$ encodes $\mathbf{J_1}$, $\vec{y}_2^{P}$ encodes $\mathbf{J_2}$, and so on). Note that usually $\vec{y}^{P} \neq \mathbf{J}$. With the proper transformation and change of basis, one can rewrite these patterns

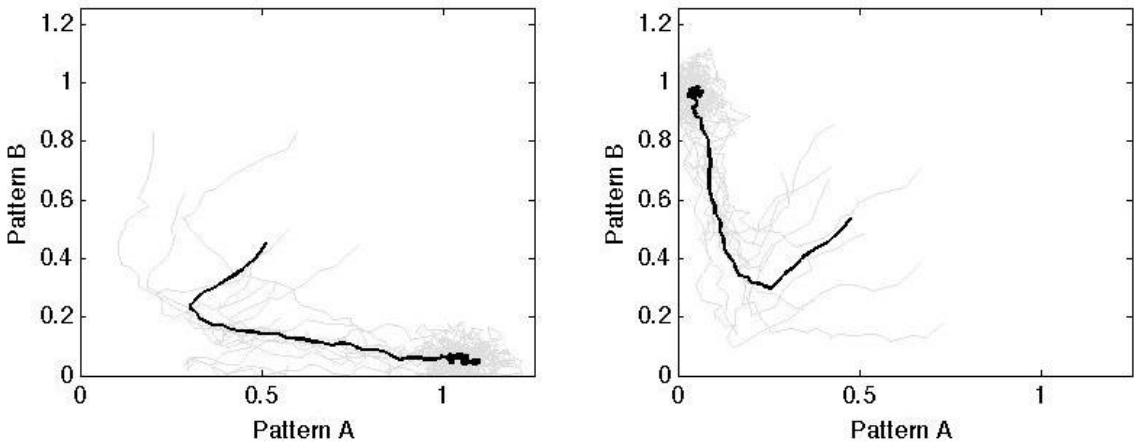

Figure 6.2: Healthy network responses to different stimuli. In the left panel, 10 trajectories when stimulus $\mathbf{J_A}$ is presented. In the right panel, 10 trajectories when stimulus $\mathbf{J_B}$ is presented. In both cases, the average trajectory is plotted in bold. Size of the Network = 20 neurons per population.

as *orthonormal* vectors (see [103] for details):

$$L = \begin{bmatrix} \vdots & & \vdots \\ \vec{y}_1^P & \cdots & \vec{y}_l^P \\ \vdots & & \vdots \end{bmatrix}_{N\times l} \longrightarrow O = \begin{bmatrix} \vdots & & \vdots \\ \vec{o}_1^P & \cdots & \vec{o}_l^P \\ \vdots & & \vdots \end{bmatrix}_{N\times l}$$

This allow us to describe the dynamics of output neurons with the following low-rank decomposition:

$$\vec{y}(t) = p_1(t)\vec{o}_1^P + \cdots + p_l(t)\vec{o}_l^P + r(t)\vec{o}^R \tag{6.3}$$

What completes the decomposition is the *remainder* vector $\vec{o}^R$ onto which all meaningless activity are projected.

Simple case: Throughout this chapter we will limit our library to only two distinct patterns (A and B). The dynamics of the output vector $\vec{y}$ can be written as

$$\vec{y}(t) = p_A(t)\vec{o}^A + p_B(t)\vec{o}^B + r(t)\vec{o}^R$$

In Figure 6.2, we initiate $\vec{y}(t=0)$ with a random combination of $\vec{o}^A$ and $\vec{o}^B$. Then, we stimulate the network with inputs $\mathbf{J_A}$ or $\mathbf{J_B}$ and plot several trajectories of $p_A(t)$ vs $p_B(t)$. Without noise,

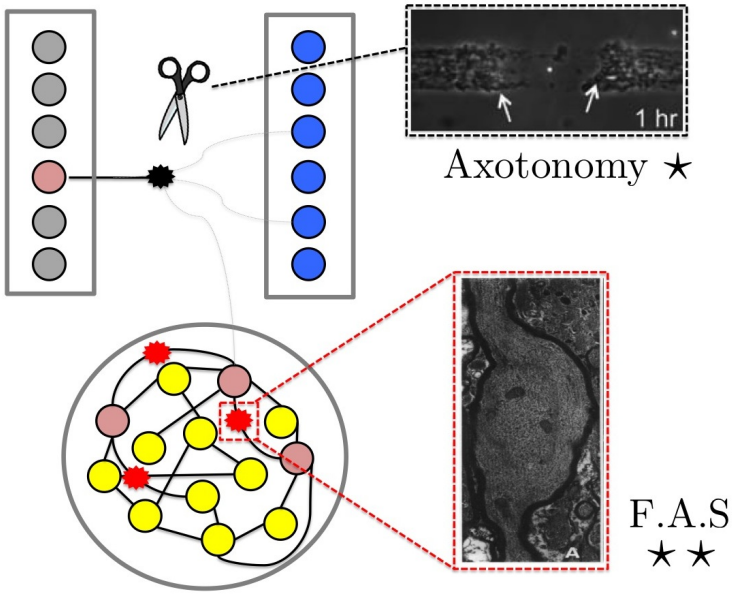

Figure 6.3: Elements of axonal pathologies following TBI and/or neurodegeneration: Axotonomy in box ($\star$) adapted from Hellman et al. ([51]). Focal Axonal Swellings in box ($\star\,\star$) adapted from Maxwell et al. ([80]).

all trajectories would converge to a fixed point ([103])– corresponding to the presented stimulus. Instead, the trajectories randomly fluctuate around them (see Fig. 6.2). We define a healthy network as a network capable of discriminating between these two stimuli successfully, i.e., that yields at $t = T_{Final}$:

$$(p_A, p_B, r) \approx \begin{cases} (1,0,0) & \text{if } \mathbf{J_A} \text{ is presented,} \\ (0,1,0) & \text{if } \mathbf{J_B} \text{ is presented,} \\ (0,0,1) & \text{if no stimulus is presented.} \end{cases} \tag{6.4}$$

6.2 Compromised neuronal networks

Traumatic Brain Injuries and/or neurodegenerative diseases can produce pathologies even at a celular scale. As a result, axonal injury is a common outcome, which in turn, can lead to Focal Axonal Swellings (FAS) and Axotomies. See the schematics of Figure 6.3. In this section we present ways to introduce injurious effects to the neuron's firing-rate capability based on the studies of Maia et al.

([74, 73]). In particular, we will discuss confusion of firing rates (filtering), reflection of spikes and spike blockage. By modifying the internal dynamics of injured neurons as well as their connections to others, we can incorporate pathological effects that will disrupt the network's functionality. Both the number of injured neurons and the type of FAS can alter the outcome of the network, suggesting that different types of injury lead to different functional deficits.

6.2.1 Damaging single-neuron firing-rate capabilities

According to the studies of Maia et al. ([74, 73]), FAS can damage a single-neuron firing-rate capability in different ways. We discuss each type of injury separately.

Confusion of firing rates: Recent theoretical and computational works ([73]) demonstrated that spike trains of certain firing rates can be reshaped along the axonal swelling. Spikes are shifted and deleted and the modified spike train can be confused by a spike train of a different firing rate. The overall changes can be summarized by a *confusion matrix*. This matrix describes the chance that a firing rate s_i is perceived as a response r_j after the injury. When $i = j$, the spike train is correctly classified (and contributes to the diagonal entries of the matrix), while $i \neq j$ means that the spike train is incorrectly classified (contributing to the off-diagonal entries).

%	r_1	r_2	r_3	r_4	r_5	r_6	r_7	r_8	r_9	r_{10}
s_1	100									
s_2	90	10								
s_3	2.5	65	32.5							
s_4		10	87.5	2.5						
s_5			27.5	67.5	5					
s_6				62.5	37.5					
s_7				15	85					
s_8				2.50	70	27.5				
s_9					30	60	7.5	2.5		
s_{10}					17.5	60	22.5			

(6.5)

Within this framework, if an injured neuron has a firing rate of s_8 at time t_n, for example, it will *effectively* fire with rate r with the following probability:

%	r_1	r_2	r_3	r_4	r_5	r_6	r_7	r_8	r_9	r_{10}
s_8	0	0	0	2.50	70	27.5	0	0	0	0

(6.6)

Reflection and Blockage: Maia and Kutz ([74]) showed that for certain geometries of FAS a spike can split into two spikes, one traveling forward and the other traveling backwards. The backward propagating pulse collides with the next spike in the original spike train and both spikes get deleted. As a consequence, in a reflection regime, the firing rate is *effectively* halved. For more dramatic shapes, the spike train can be completely blocked by setting the effective firing rate to zero.

Axotomy: In extreme cases, the axon can be severed and completely separated (see Fig. 6.3). Cell death typically follows this event. We can add axotomies to our models by permanently setting entries in the connectivity matrix to zero. We remark that swellings that lead to blockage can sometimes improve and allow for partial signal transmission while only in special circumstances can an axon regenerate after an axotomy.

6.2.2 Anomalous network responses

In the previous section we discussed how a healthy network responds to different stimuli. Regardless of the initial conditions, the trajectories end fluctuating around the fixed points that correspond to that pattern (see Fig. 6.2 and Eq. 6.4). The network responses can change significantly when we introduce injured neurons. To illustrate this fact, we randomly injured 30% of the neurons in the network (10% of confusion/filtering, 10% of reflection and 10% of blockage). The corresponding anomalous responses (trajectories) are shown in Figure 6.4. Note that the trajectories do not form clear clustering regions near the fixed points anymore. Instead, many trajectories end near the origin, which means no stable response pattern (or library element) was produced.

To evaluate these anomalous responses, we simulate again several trajectories, keeping track of their endpoints. The endpoints are clustered before and after the injury according to two different criteria (discussed below). The % of endpoints that leave their original clusters can be used to access the loss of the transmitted information of the system.

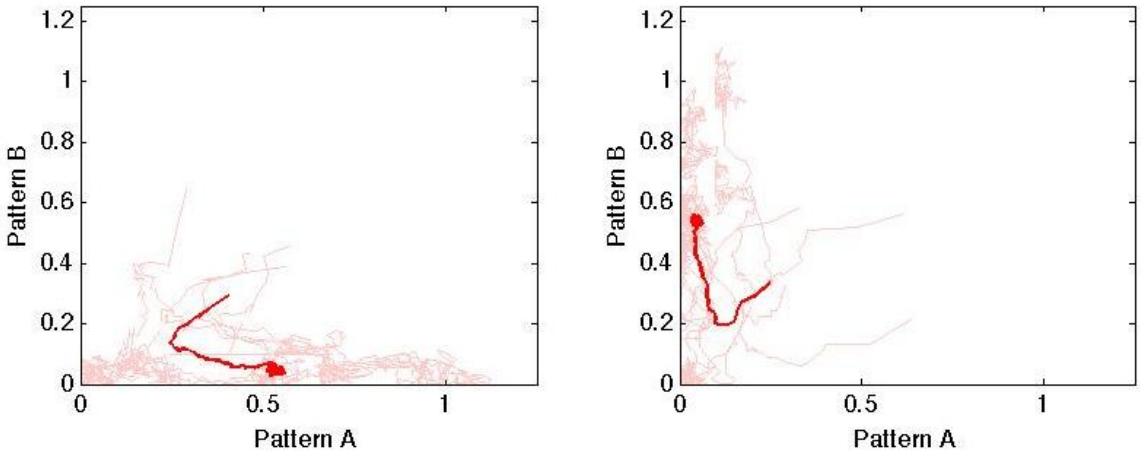

Figure 6.4: Injured network responses to different stimuli. In the left panel, 10 trajectories when stimulus $\mathbf{J_A}$ is presented. In the right panel, 10 trajectories when stimulus $\mathbf{J_B}$ is presented. In both cases, the average trajectory is plotted in bold. Size of the Network = 20 neurons per population, where 30% of the neurons were randomly injured with FAS (10% in confusion/filtering regime, 10% in the reflection regime and 10% in the blockage regime).

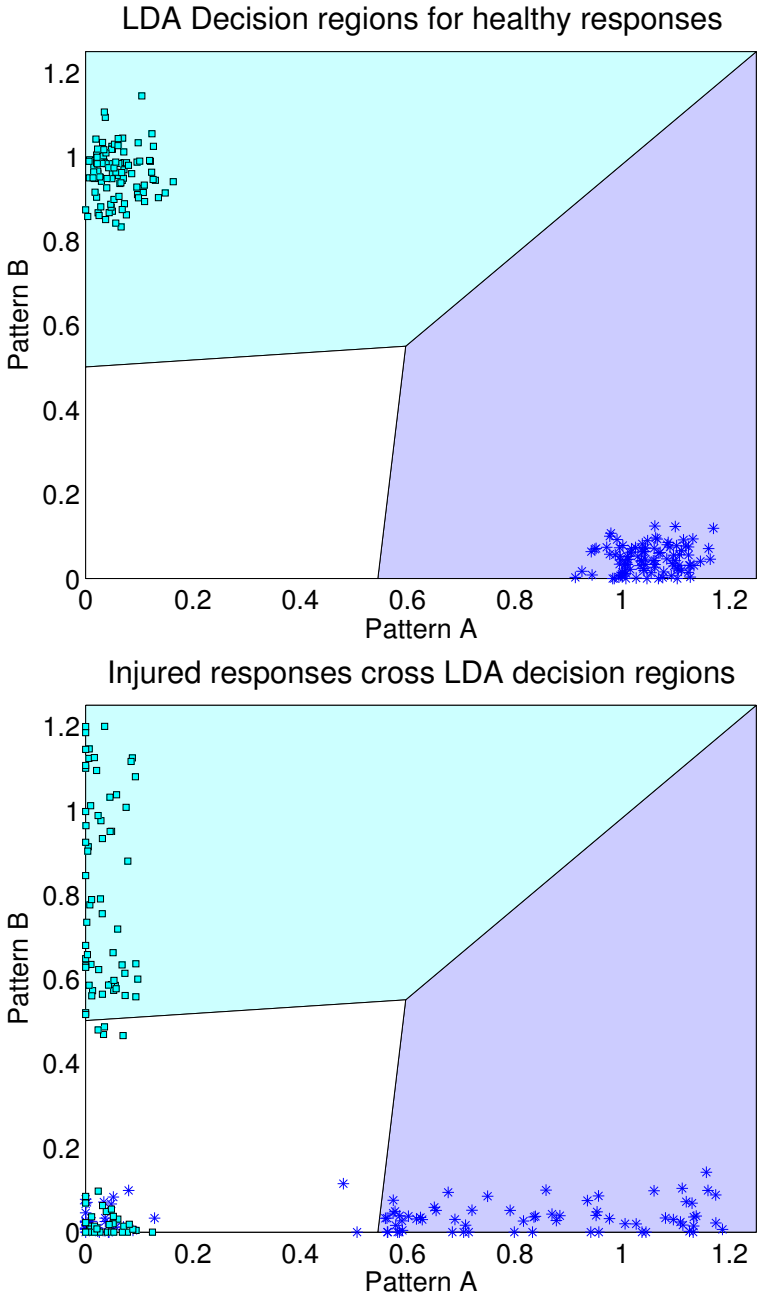

Figure 6.5: Endpoints of several trajectories after presenting inputs $\mathbf{J_A}$ and $\mathbf{J_B}$ to the network. (Top) In a healthy network the endpoints are grouped in clusters corresponding to different stimulus. LDA provides the lines that give maximum separation between the clusters. (Bottom) In an injured network, several endpoints cross the original separation lines being misclassified, and thus, jeopardizing the system's ability to transmit information.

Linear Discriminant Analysis (LDA): LDA is a method used in statistics, pattern recognition and machine learning to find a linear combination of features which separates two or more classes of objects of events. In our case, we use LDA to separate the network responses in three classes: response pattern A, response pattern B and no response. We generate a *training set* of responses where the classes of the sample are known. The classification problem is then to find a good predictor for the classes of any sample with the same distribution (not necessarily from the training set). The result of this analysis are hyperplanes that yield maximum separation between the classes (lines in the 2D case). See Figure 6.5 (top panel) for an example of LDA classification (where the dark blue region corresponds to Pattern A, the light blue region to Pattern B and the white region to no response). Figure 6.5 (bottom panel) shows that after injuring the network, many of its responses now cross the original separating lines, mostly falling in the white region. The misclassification can be quantified in terms of *confusion matrices*, discussed in details in the previous chapters. For this example we have:

% in each region	zero	A	B
No Stimulus	100	0	0
Response to A	0	100	0
Response to B	0	0	100

$\xrightarrow{Injury}$

% in each region	zero	A	B
No Stimulus	100	0	0
Response to A	34	66	0
Response to B	38	0	62

Recall from [73] that the *transmitted information* (T.I), a measure of separation between classes, can be associated to each confusion matrix. Since the confusion matrix associated to the injured network is less diagonal than the one associated to the healthy network, there is a clear relative loss of T.I. In this case, of 50.58%.

Gaussian Mixture Models (GMM): GMM refers to a parametric probability density function represented as a weighted sum of Gaussian component densities and commonly used for data clustering. In our case, we use GMM to cluster the network responses in three distinct gaussian components: pattern A, pattern B and no response. The method uses an iterative algorithm that converges to a local optimum, and yields (in an appropriate sense) the best 3-gaussian fit to our data. See Figure 6.6 (top panel) for an example, where each ellipse represent the 95% confidence interval

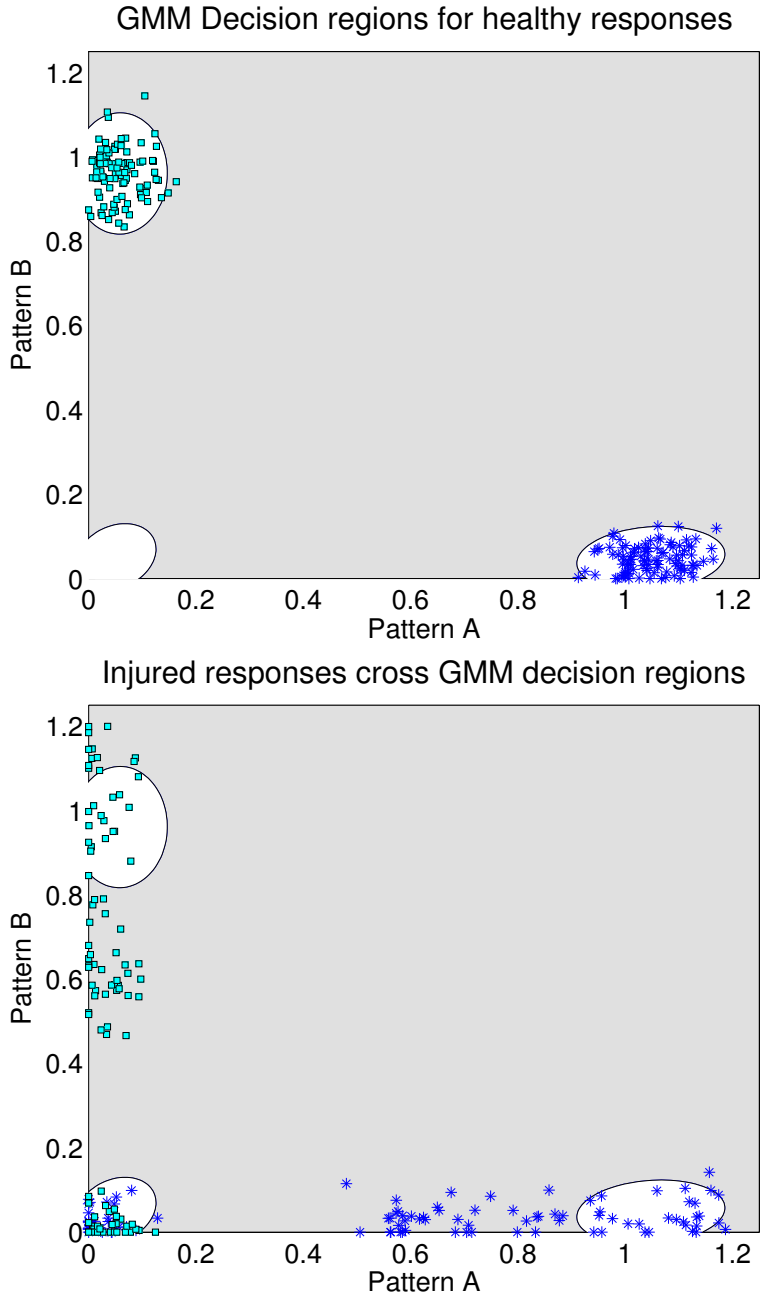

Figure 6.6: Endpoints of several trajectories after presenting inputs $\mathbf{J_A}$ and $\mathbf{J_B}$ to the network. (Top) In a healthy network the endpoints are grouped in clusters corresponding to different stimulus. GMM provides the best 3-Gaussian fit to the data. The ellipses correspond to 95% confidence interval for each Gaussian component. (Bottom) In an injured network, several endpoints leave the confidence intervals being misclassified, and thus, jeopardizing the system's ability to transmit information.

for each gaussian component. Computations were performed using the `gmdistribution` function from MATLAB's Statistics Toolbox. Figure 6.6 (bottom panel) shows that after injuring the network, many trajectories do not end within the original ellipses. The GMM criteria produce much more accentuated misclassification than the LDA criteria. The corresponding confusion matrices (before and after injury) for the same example are now given by:

% in each ellipse	none	A	B
No Stimulus	100	0	0
Response to A	5	95	0
Response to B	4	0	96

$\xrightarrow{Injury}$

% in each ellipse	none	A	B
No Stimulus	100	0	0
Response to A	75	25	0
Response to B	84	0	16

The relative loss of transmitted information after the injury in this case is equal to 83.96% (and as expected, the loss is above the 53% given by the LDA criteria).

6.3 Results

This far, we have established that:

1. We can extract meaningful response patterns (to either stimulus $\mathbf{J_A}$ or $\mathbf{J_B}$) from the output of the neuronal network.

2. For a healthy network, the endpoints of trajectories typically form well-separated response clusters. Either LDA or GMM can be used to discriminate responses from $\mathbf{J_A}$ or $\mathbf{J_B}$.

3. For an injured network, the trajectories may end outside the original classification regions (crossing separation lines in LDA and leaving the confidence-interval ellipses in GMM).

4. The % of misclassified responses of an injured network, summarized in confusion matrices, can be used to quantify the loss of transmitted information in the system.

We also remark that since the decision ellipses in GMM are much smaller that the decision regions in LDA, it produces much more misclassification (and bigger losses in transmitted information). Regardless of the classification criteria, the loss in transmitted information depends on the % of injured neurons in the population and the corresponding distribution of FAS (in the filtering regime,

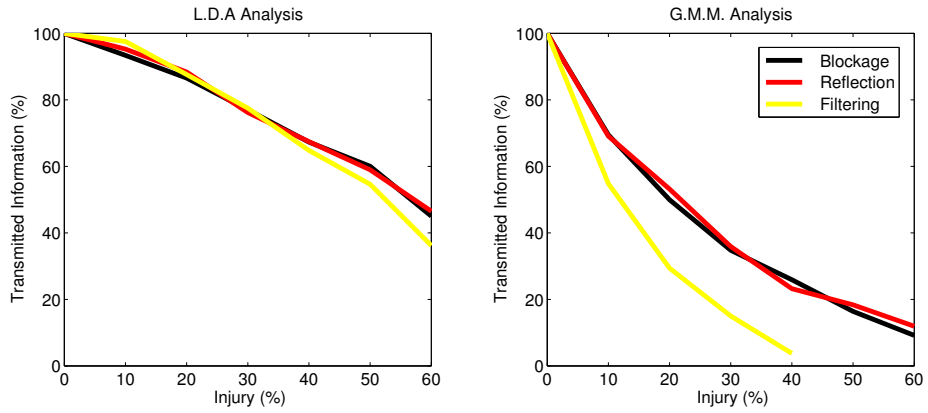

Figure 6.7: Transmitted Information (%) as a function of damaged neurons in the population. Within each injury, all FAS have the same dysfunctional type of regime: filtering/confusion (yellow), reflection (red) and blockage (black). In the left panel LDA was used as the classification criteria and in the right panel, GMM was used as the classification criteria. Size of the network = 20 neurons for each population.

in the reflection regime or in the blockage regime). In this section we will study how different distributions of FAS lead to different deficits in the network's responses.

6.3.1 FAS distributions and loss of transmitted information

We first consider homogeneous distributions of FAS in the network, i.e., when all injured neurons operate in the same dysfunctional regime. For a network of 20 neurons in each population, we calculate how the transmitted information (TI) decays as we increase the % of injured neurons. See Figure 6.7.

Our results show that when the GMM criteria is used, FAS in the confusion/filtering dysfunctional regime are significantly more harmful than those in the blockage and reflection regimes. This result is very intriguing since the most damaged neurons typically exhibit FAS in the blockage regime ([74]). When the LDA criteria is used, the type of FAS regime does not seem to influence the loss of TI except for larger (%) of injured neurons, where again, the confusion/filtering regime is slightly worse than the others.

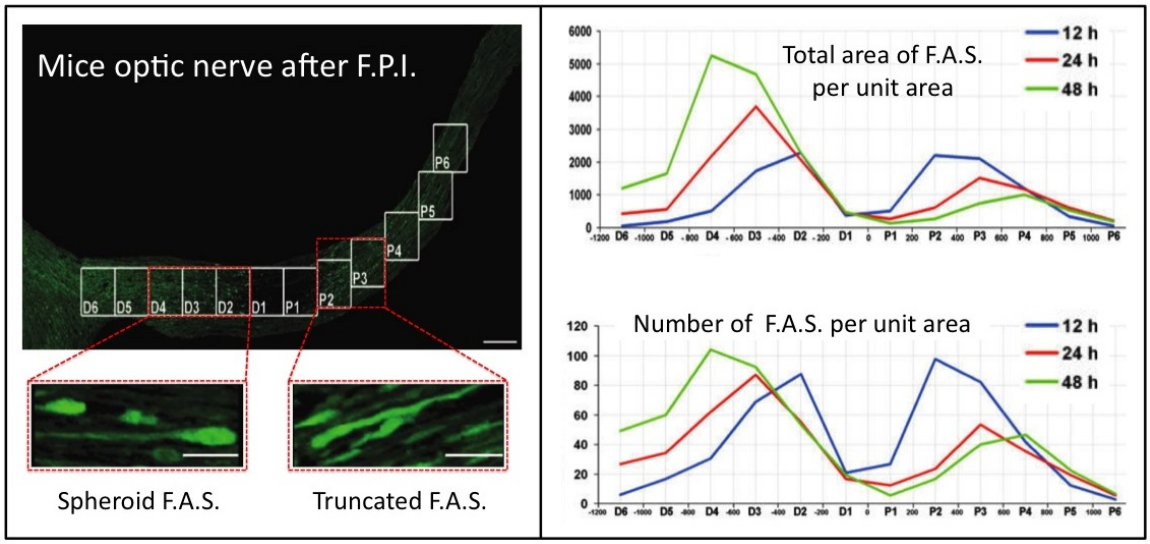

Figure 6.8: Experimental results adapted from Wang et al. ([119]). After traumatically inducing axonal injury in mice, the optical nerve was removed and analyzed for fluorescence and confocal microscopy. Focal Axonal Swellings (FAS) were reported to have *qualitatively* different shapes: spheroids (ellipses) at the distal segment and truncated shapes at the proximal segment. The total area and number of FAS varied as the injury progressed in time (12h, 24h and 48h).

6.3.2 Experimental injury distributions from Wang et al.

The shapes of FAS after traumatic brain injuries can vary wildly and we should not expect a homogeneous distribution of FAS. In fact, we will try to infer heterogenous distribution of FAS from a set of experimental results.

Wang et al. ([119]) followed the progression of traumatically-induced axonal injury in mice. Each animal's optical nerve –which is a relatively organized and aligned bundle of axons– was damaged after a central fluid percussion injury. See Figure 6.8 (top-left). At different times after the injury (12h, 24h and 48h), mice were euthanized and had their optic tract removed from the skull for fluorescence analysis and confocal microscopy. Focal Axonal Swellings (FAS) were reported to have *qualitatively* different shapes: spheroids (ellipses) at the distal segment and truncated shapes at the proximal segment. See Figure 6.8 (bottom-left).

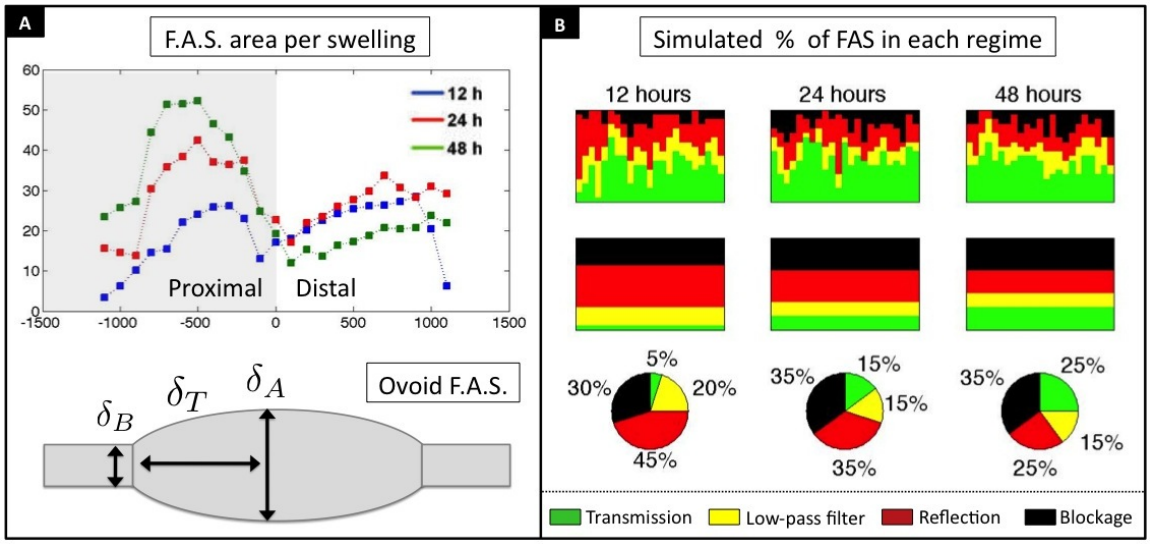

Figure 6.9: We generate a family of ovoids having area within one standard deviation from the distributions of FAS area per swelling. For each generated FAS, we extracted the parameters $[\delta_B, \delta_T, \delta A]$, necessary to estimate the propagation regime η (following [74, 73]). By equating the regime of an axon to the worse regime of it's FAS (intermediate row in right panel), we infer the % of FAS in transmission, filtering, reflection and blockage regimes.

The most innovative part of this study was the assessment of the *distributions* of the total-area & number of FAS (per unit area). See the right panel at Figure 6.8. Despite the lack of standard protocols for these type of measurements, the study demonstrates some important features:

1. FAS injury distributions differ along the spatial segments of the bundle/network in shape, size and number.

2. FAS shape distributions are not static but change dynamically as the injury progress in time.

Detailed descriptions of the geometry of individual FAS were unavailable and only distributions of number and sizes of FAS per unit area provided. We divided one distribution by the other to estimate distributions for the *average area per swelling* (see Fig. 6.9). Since FAS in the distal segment were described as spheroids (elliptical shapes), we can generate a family of ovoids having area within one standard deviation of the measurement (see bottom left panel of Fig. 6.9). For each generated FAS, we extracted the parameters $[\delta_B, \delta_T, \delta A]$, necessary to estimate the propagation regime η ([74, 73]). By equating the regime of an axon to the worst regime of it's FAS (intermediate row in right panel of Fig. 6.9) we infer the % of FAS in transmission, filtering, reflection and blockage regimes.

In Figure 6.10 we calculated the decay of the Transmitted Information (%) as a function of damaged neurons in the population. The three different heterogenous distributions of FAS (for 12h, 24h and 48h) yield different decay rates. For a small percentage of injured neurons, different heterogeneities did not significantly alter the decay of TI (for both LDA and GMM criteria). For larger fractions of injured neurons however, the results show a clear improvement as the injury progressed in time, suggesting that recovering mechanisms might have played a role.

The results of Figure 6.10 are interesting, because although the % of FAS in the transmission regime increased from 12h to 48h, the % of FAS in the blockage regime also increased (see Fig. 6.9). Based on the results for homogeneous FAS distributions, the reduction of FAS in the confusion/filtering regime should also contribute to an improvement in the TI. As a consistency check, we note that the heterogeneous distributions yield better results than the worse homogeneous distribution (filtering/confusion alone).

Our heterogeneous distributions were derived from imperfect and indirect calculations (as shown at the bottom-right panel of Figure 6.9). We hope that our results will incentivize experimentalists to

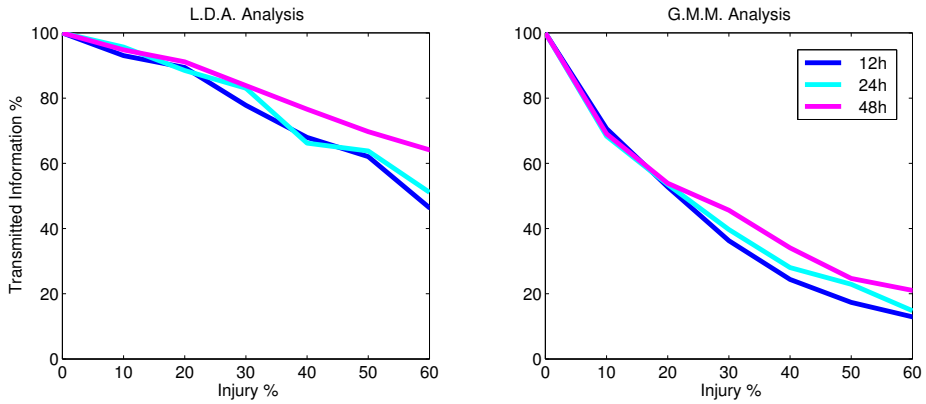

Figure 6.10: Transmitted Information (%) as a function of damaged neurons in the population. The (%) of FAS in different dysfunctional types follow the pie charts in Figure 6.9. The three different heterogenous distributions of FAS (for 12h, 24h and 48h) were estimated from the experiments of Wang et al. ([119]). In the left panel LDA was used as the classification criteria and in the right panel, GMM was used as the classification criteria. Size of the network = 20 neurons for each population.

keep track of key geometric parameters for each swelling so that we can infer better heterogeneous FAS distributions. Nevertheless, the distributions showed some interesting features and allowed us to illustrate novel methodologies to quantify the loss of functionality in injured networks.

6.3.3 Insights to recover functionality of injured networks

A better theoretical understanding of the *collective* effects of FAS in neuronal populations can lead to novel strategies to recover the functionality of injured neuronal networks, ultimately leading to biophysical schemes for suppressing the harmful effects of TBI and/or other neurodegenerative diseases. We imagine at least two broad directions:

1. The network retrains its classifiers to better separate the injured responses. We show these new optimal classifiers for LDA and GMM criteria in Figure 6.11 for the example discussed previously. One can observe new separation lines for the LDA criteria and "stretched" new ellipses for the GMM criteria. In other words, the network slightly adjusts the low-dimensional

manifold in which it used to encode meaningful patterns.

2. The network replaces broken response patterns by adding new *library elements* to its repertoire. The idea is to re-route the bulk of the encoding activity to different and uninjured neurons instead of using the pre-existing routes by re-weighting the connectivity matrices. In this case, the network is creating a completely different low-dimensional manifold to encode meaningful patterns.

In either case, the time-scales involved in plasticity/recovery will be of utmost importance. We guess that it might be faster and cheaper metabolic-wise for a network to slightly adjust its classifier to better separate injured response clusters. However, if the responses (after changing classifiers) still transmit little information, the only alternative might be to replace broken elements in the library by new ones. We hope to explore these questions in future works.

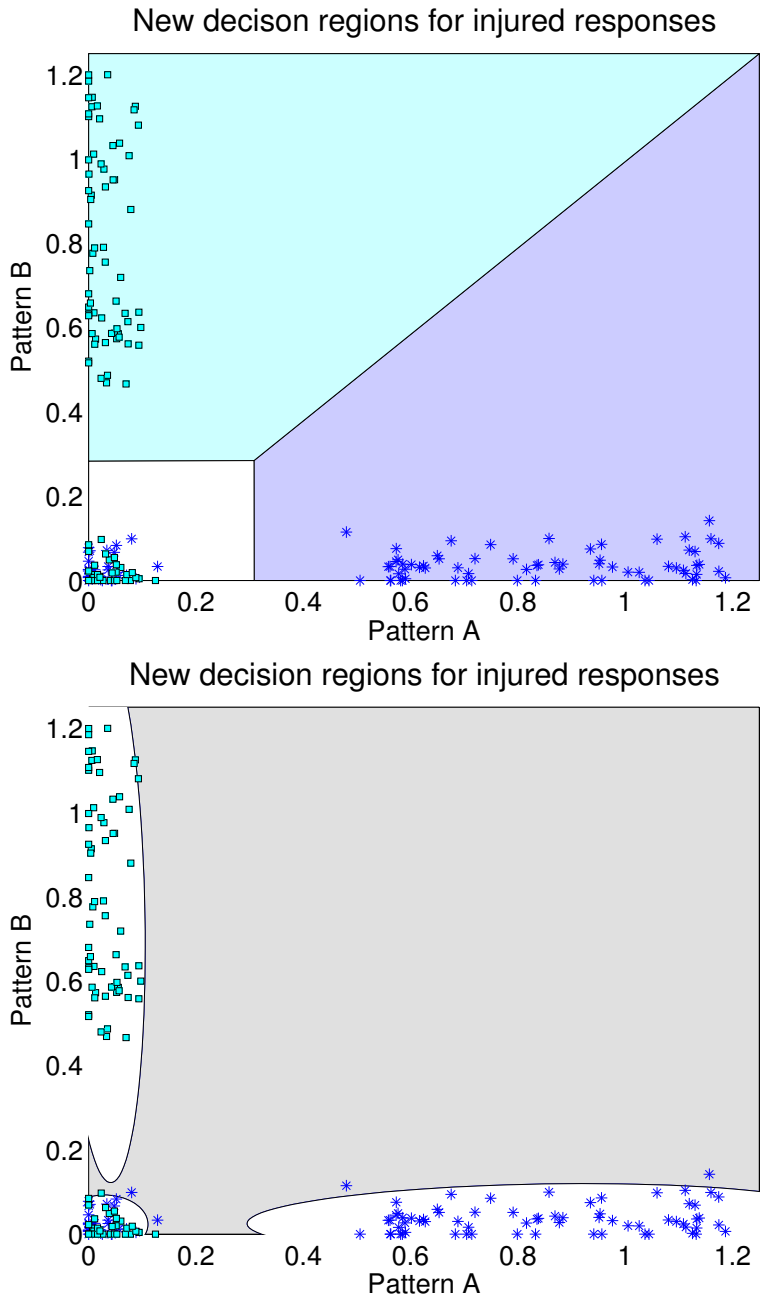

Figure 6.11: New classifiers can better separate the injured responses to $\mathbf{J_A}$ and $\mathbf{J_B}$. (Top) By retraining the LDA classifiers one can recuperate misclassified endpoints not too close to the origin. (Bottom) By re-evaluating the 3-Gaussian best fit to the data, we obtain "stretched" ellipses for each Gaussian component. It also recuperates misclassified endpoints not too close to the origin, improving the system's ability to transmit information.

Chapter 7

CONCLUSIONS AND FUTURE WORKS

In this chapter we discuss our findings and directions for future works.

Importance of this research: There is a broad need in the neuroscience, neurological and biomedical engineering communities to better classify, quantify, and diagnose Focal Axonal Swellings (FAS), and their impact on cognitive deficits and/or neural functionality [82, 20]. FAS is a critical biomarker in several leading neurodegenerative diseases such as Alzheimer's [113, 65], Parkinson's [40], Creutzfeldt-Jakob's [67], HIV dementia [1] and Multiple Sclerosis [37, 110]. They are also a hallmark feature of concussions and Traumatic Brain Injury (TBI) - the leading cause of death among youngsters worldwide and a lightning rod issue in contact sports [33]. Further, TBI is the signature injury of the wars in Iraq and Afghanistan, affecting a large percentage of returning veterans [60, 120]. Figure 7.1 depicts a number of focal axonal swellings resulting from TBI and a variety of different neurodegenerative diseases.

One of the most challenging aspects of research in neurodegenerative diseases and TBI is understanding how neuronal pathologies that develop at a cellular level [59, 84] compromise the functionality of an entire network of neurons. TBI studies demonstrate that FAS can induce up to a 30-fold increase in axon diameter [108, 109], potentially interrupting axonal transport and/or significantly impairing the underlying spike train propagation responsible for encoding information in neural activity [74, 73, 63]. Many studies report cognitive, behavioral, perceptual and sensorymotor impairments resulting from such disorders, yet no framework could link these macro-scale behavioral symptoms to the FAS pathologies observed at the cellular level, or micro-scale biophysics [72, 52, 105, 80].

In this work we quantify the impact of FAS on information encoding at the individual neuron level, creating novel metrics for evaluating cognitive impairments. Recent computational studies show how geometrical properties of FAS can alter their ability to faithfully transmit spike train

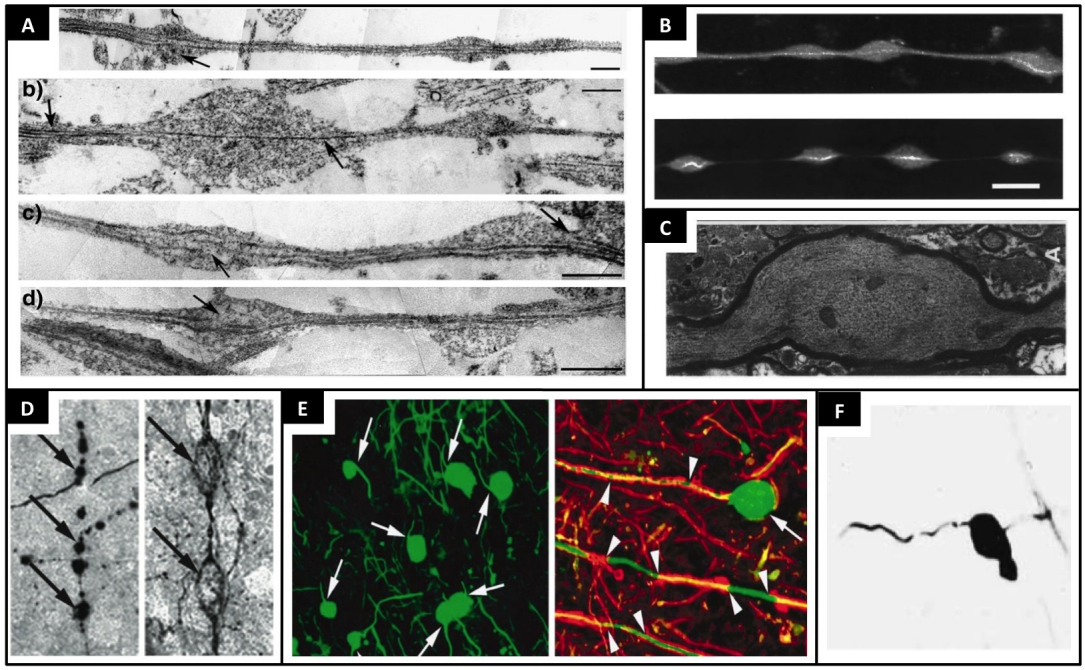

Figure 7.1: Focal Axonal Swellings (FAS) arise in several neurodegenerative diseases, concussions and traumatic brain injuries. Panel **A**. Transmission electron microscopy image of axons 3h post-stretch injury. Modified from [108]. Panel **B**. Image 2h after dynamic stretch injury of two human neuron populations. Modified from [105]. Panel **C**. Image 1h after stretch injury to guinea pig optic nerve. Modified from [80]. The in-vitro stretch injury experiments from Panels A-C mimic the effects of traumatic brain injuries and concussions. Panel **D**. Axonal swellings are implicated in patients with Alzheimer' s disease where stress-induced amyloidal precursor protein accumulates in axonal compartments. Modified from [65]. Panels **E-F**. Images of FAS pathologies in Multiple Sclerosis. Modified from [110] and [37].

encodings by selectively deleting spikes, creating time-delays and/or time-shifts in spike trains, reflecting spikes at the swelling or even completely blocking spike trains altogether [74, 73].

Role of axonal geometry in spike propagation: The classical view on axons as cables that simply transmit spike train encodings is continuously being challenged and revisited as we learn more about their role in signal and information processing [15, 25]. Specifically, the interplay between nonlinearities resulting from ion channel properties and geometric inhomogeneities alters the signal before its arrival at synaptic sites. The effects of axonal geometry are even more dramatic in neuronal dysfunctions where effects from axotonomy, regional compaction and focal axonal swellings are implicated [63]. By compromising spike train propagation, axons thus play a critical role in the loss of transmitted information in neuronal networks.

The spike propagation regime number η: Geometrical tapering parameters of an axonal enlargement can alter spike train propagation properties [73, 74]. Figure 7.2A illustrates a series of spike trains that are reshaped as they travel through an axonal swelling. Spikes can be delayed, reflected or even deleted (red) depending on the three critical parameters:

$$\begin{aligned} \delta_B &= \text{diameter before} \\ \delta_T &= \text{diameter of transition} \\ \delta_A &= \text{diameter after}. \end{aligned}$$

By exploring the geometrical parameter space associated with these parameters (Fig. 7.2B), it is possible to assess individual swellings and their impact on the propagation of an individual spike. Three possibilities exists [73, 74]: (i) transmission, but potentially with time-delay, (ii) reflection, and (iii) blockage (deletion).

Individual spikes, however, are generically part of a larger cohort of spike trains. Thus from a broader viewpoint, the effects on individual spikes can be translated to an evaluation of spike trains. Indeed, we can map any given axonal enlargement to its functional response on spike train encodings. The following possibilities exist in order of increasing damage: normal transmission of the spike train with time-shifting (Fig. 7.2C), low-pass filtering of high firing rates due to pile-up collisions and deletions of selected spikes (Fig. 7.2D) [73], spike reflections that also lead to a low-

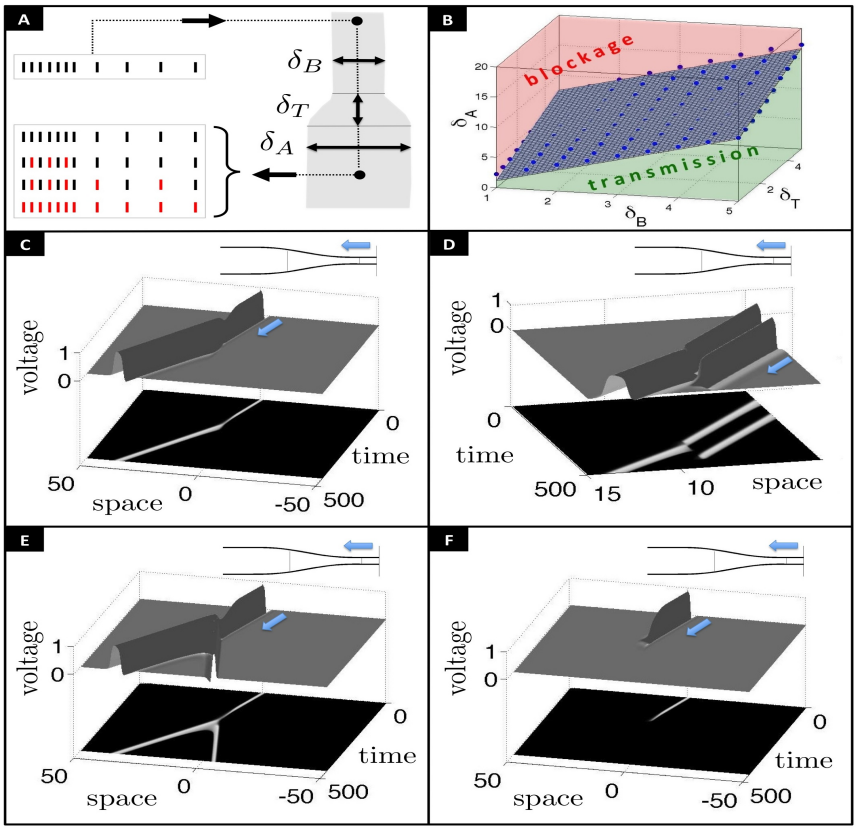

Figure 7.2: Axonal geometry defines spike propagation regime. Panel **A**. Spike trains can be reshaped as they travel along an axonal enlargement. Individual spikes can be delayed or even deleted (red). The geometrical tapering parameters $[\delta_B, \delta_T, \delta_A]$ play a key role. Panel **B**. Explores the parameter space and maps parameter values to their corresponding regime. Panel **C**. Normal transmission regime. Panel **D**. Filtering regime, where the second spike is deleted and only the first one transmits. Panel **E**. Reflection regime, where the pulse splits into two, one propagating forward and the other backwards. The backwards propagating pulse will delete the next pulse in the spike train sequence. Panel **F**. Blockage regime, where no spikes transmit. Modified from [74, 73].

pass filtering on both high and low firing rates (Fig. 7.2E), and spike train blockage (Fig. 7.2F). The relation between the axonal enlargement parameters and the propagation regimes is well captured by the simple function η [74]:

$$\begin{aligned} \eta(\delta_B, \delta_T, \delta_A) &= A + B\delta_B + C\delta_T - \delta_A \\ &= \begin{cases} \gg 1 & \text{for Transmission} \\ \approx 1 & \text{for Filtering} \\ \approx 0 & \text{for Reflection} \\ \ll -1 & \text{for Blockage}, \end{cases} \end{aligned} \tag{7.1}$$

where $A = -1.842$, $B = 2.284$ and $C = 1.415$. This equation predicts trouble regions in axon geometries and will be used throughout the rest of the work. We remark that the η estimate needs to be calibrated, as detailed in later sections, to specific physiological settings in order to be of quantitative predictive value. It should be noted that many experimental works corroborate this analysis by demonstrating that abrupt or gradual changes in the axonal diameter can delay [76, 100], block [44, 124, 2, 63] or reflect a single action potential [31, 96, 2]. Such biophysical evidence in combination with theoretical studies form the foundations of the present work.

Contributions: This work reinforces recent findings that the shape of the FAS are essential for assessing the post-injury capabilities of axons [73, 74, 63, 2]. TBI studies demonstrate that FAS can induce up to a 30-fold increase in axon diameter [108, 109]. Here we combined geometrical tapering parameters with theoretical estimates to provide valuable insight on critical regions for spike propagation; Large swellings with a smooth cross-sectional increase might not significantly alter electrophysiological signaling whereas smaller FAS with abrupt diameter changes are especially prone to blockage or loss of transmitted information.

Challenges posed by real axonal data: It is important to recognize the role of FAS geometry for the broader research community especially when there are no well-established protocols to measure geometrical properties of FAS [72, 52, 105, 80]. In fact, it can be challenging to characterize FAS geometry in a principled, general, and adaptive way. Thus, we developed novel algorithms

and/or tailored existing ones to address the need to better classify, quantify, and diagnose FAS. We used procrustes superimposition to fix image artifacts and extracted axonal cross-section with patched trapezoids alternated with turning regions. From these cross-section results, we used different rules (sliding windows, maxima and minima, 10% - 90% rule) to estimate the tapering parameters $[\delta_B, \delta_T, \delta_A]$ (see Figure 7.2A) necessary to calculate the η estimates and the corresponding spike propagation regime (see equation 7.1).

Some of the limitations of our work include the fact that the η estimates were derived for unmylienated FitzHugh-Nagumo neuron models [73, 74]. This model might not be suited for all physiological settings and may require specific calibrations and/or other adjustments. Regardless, if new η estimates become available for different neuronal settings, they can be easily incorporated into the MATLAB toolbox developed for this work.

Overall, one of the challenging aspects of research in neurodegenerative diseases and TBI is understanding how neuronal pathologies developed at a cellular level [59, 84] compromise the functionality of an entire network of neurons. Many studies reported cognitive, behavioral, perceptual and sensory-motor impairments resulting from such disorders, yet no framework could link these macro scale symptoms to the FAS pathologies observed at the cellular level, or micro scale [72, 52, 105, 80]. Our toolbox provides – in analogy to car traffic maps – a way to identify blocked or impaired routes for spike train encodings and signal flow. By keeping track of where axonal color-code changes from green to yellow (filtering of spikes), to red (spike reflection), or to black (spike blockage), an evaluation of potential cognitive impairment can be made. We believe this framework is a promising starting point for diagnosing axonal swellings and consequently the neurodegenerative disorders in which they are implicated.

FAS in neuronal networks: We discussed ways to introduce FAS in firing-rate neuronal networks. In our example, a healthy network is capable of producing meaningful response patterns to specific stimuli. Additionally, these responses appear clustered (in a proper low-dimensional representation) and can be successfully discriminated by Linear Discriminant Analysis or Gaussian Mixture Models. An injured network however, produce responses that leave the original clustering regions and are thus misclassified, jeopardizing the system's ability to transmit information (TI). The loss of TI depend on the % of injured neuron as well as in the distribution of FAS in differ-

ent dysfunctional regimes (confusion/filtering, reflection, blockage). Our simulations suggest that filtering is the most harmful regime. We also inferred heterogeneous FAS distributions from the experiments of Wang et al. ([119]), and after simulating the network with those parameters, we concluded that the system most likely improved from 12h to 48h after the injury. This suggests that natural recovery mechanisms might have played a role. These different cases allowed us to illustrate new methodologies to access the harmful effects of TBI and neurodegenerative diseases.

Future works: There are several other neuronal network settings to investigate under the presence of traumatic brain injuries and other pathologies. In particular, *learning* networks, that via plasticity mechanisms, can adapt themselves to produce desired activity patterns. By damaging these networks, after and during the learning process, we might be able to gain insight about cognitive losses typically associated to these disorders. Another direction to explore is how FAS spread in disorders such as Alzheimer's disease in slower time-scales. Based on our results for TBI, we conjecture that the distribution of swellings in different dysfunctional regimes may also change as the neurodegenerative disease evolves. This can have strong implications since different distributions lead to different collective responses.

BIBLIOGRAPHY

[1] H. Adle-Biassette, F. Chretien, L. Wingertsmann, C. Hery, T. Ereau, F. Scaravilli, M. Tardieu, and F. Gray. Neuronal apoptosis does not correlate with dementia in hiv infection but is related to microglial activation and axonal damage. *Neuropathology and Applied Neurobiology*, 25:123–133, 1999.

[2] R. Altemberger, K.A. Lindsay, J.M. Ogden, and J.R. Rosenberg. The interaction between membrane kinetics and membrane geometry in the transmission of action potentials in non-uniform excitable fibres: a finite element approach. *Journal of Neuroscience Methods*, 112:101–117, 2001.

[3] S. Antic, J.P. Wuskell, L. Loew, and D. Zecevic. Functional profile of the giant metacerebral neuron of helix aspersa: temporal and spatial dynamics of electrical activity in situ. *The Journal of Physiology*, 527:55–69, 2000.

[4] D. Aronov and D. Victor, J. Non-euclidean properties of spike train metric spaces. *Physical Reviews E - Stat. Nonlin. Soft Matter Phys.*, 69, 2004.

[5] S.A. Baccus. Synaptic facilitation by reflected action potentials: enhancement of transmission when nerve impulses reverse direction at axon branch points. *Proceedings of the National Academy of Sciences*, 95(14):8345–8350, 1998.

[6] S.A. Baccus, B.D. Burrell, C.L. Sahley, and K.J. Muller. Action potential reflection and failure at axon branch points cause stepwise changes in epsps in a neuron essential for learning. *Journal of Neurophysiology*, 83(3):1693–1700, 2000.

[7] D.J Bakkum, U. Frey, M. Radivojevic, T.L. Russel, Müller. J., M. Fiscella, H. Takahashi, and A. Hierlemann. Tracking axonal action potential propagation on a high density micro electrode array across hundreds of sites. *Nature communications*, 4(2181), 2013.

[8] D.H. Barron and B.H. Matthews. Intermittent conduction in the spinal cord. *The Journal of Physiology*, 85:73–103, 1935.

[9] N. Becker, C.J. Wierenga, Bonhoeffer Fonseca, R., and U.V. T., Nagerl. Ltd induction causes morphological changes of presynaptic boutons and reduces their contacts with spines. *Neuron*, 60(4), 2008.

[10] D. Beeman and J.M. Bower. The book of genesis: exploring realistic neural models with the general neural simulation system, second edition. *Springer-Verlag, New York.*, 1993.

[11] K. Bielefeldt and M.B. Jackson. A calcium-activated potassium chan- nel causes frequency-dependent action-potential failures in a mammalian nerve terminal. *Journal of Neurophysiology*, 70:284–298, 1993.

[12] P.C. Blumbergs, G. Scott, J. Manavis, H. Wainwright, D.A. Simpson, and A.J. McLean. Topography of axonal injury as defined by amyloid precursor protein and the sector scoring method in mild and severe closed head injury. *Journal of Neurotrauma*, 12:565–572, 1995.

[13] C.W. Bourque. Intraterminal recordings from the rat neurohypophysis in vitro. *The Journal of Physiology*, 421:247–262, 1990.

[14] K. D. Browne, X. H. Chen, D. F. Meaney, and D. H. Smith. Mild traumatic brain injury and diffuse axonal injury in swine. *Journal of Neurotrauma*, 28(9):1747–1755, 2011.

[15] D. Bucher and J. M. Goaillard. Beyond faithful conduction: short term dynamics, neuromodulation, and log-term regulation of spike propagation in the axon. *Progress in Neurobiology*, 94:307–346, 2011.

[16] M. Butz, F. Worgotter, and A. van Ooyen. Activity-dependent structural plasticity. *Brain Research Reviews*, 60(2):287–305, 2009.

[17] N.T. Carnevale and M.L. Hines. *The Neuron Book*. Cambridge University Press, 2009.

[18] W.R. Chen, G.Y. Shen, G.M. Shepherd, M.L. Hines, and J. Midtgaard. Multiple modes of action potential initiation and propagation in mitral cell primary dendrite. *Journal of Neurophysiology*, 88:27552764, 2002.

[19] C.W. Christman, M.S. Grady, S.A. Walker, K.L. Hol-Loway, and J.T. Povlishock. Ultrastructural studies of diffuse axonal injury in humans. *Journal of Neurotrauma*, 11:173–186, 1994.

[20] M. Coleman. Axon degeneration mechanisms: commonality amid diversity. *Nature Reviews Neuroscience*, 6(11):889–898, 2005.

[21] J.W. Cooley and F.A. Dodge. Digital computer solutions for excitation and propagation of the nerve impulse. *Biophysical Journal*, 6(5):583–599, 1966.

[22] P. Dayan and L.F. Abbot. *Theoretical neuroscience*. MIT Press, 2001.

[23] V. De Paola, A. Holtmaat, G. Knott, S. Song, L. Willbrecht, P. Caroni, and K. Svoboda. Cell type-specific structural plasticity of axonal branches and boutons in the adult neocortex. *Neuron*, 49:861–875, 2006.

[24] D. Debanne. Information processing in the axon. *Nature Reviews Neuroscience*, 5(4):304–316, 2004.

[25] D. Debanne, E. Campanac, A. Bialowas, E. Carlier, and G. Alcaraz. Axon physiology. *Physiological Reviews*, 91:555–602, 2011.

[26] D. Debanne, N.C. Guerineau, B.H. Gahwiler, and S.M. Thompson. Action-potential propagation gated by an axonal i(a)-like k?? conductance in hippocampus. *Nature*, 389:286–289, 1997.

[27] M. Deschenes and P. Landry. Axonal branch diameter and spacing of nodes in the terminal arborization of identified thalamic and cortical neurons. *Brain Research*, 191:538–544, 1980.

[28] C. Ducreux, J.C. Reynaud, and J.J. Puizillout. Spike conduction properties of t-shaped c neurons in the rabbit nodose ganglion. *Pflgers Arch*, 424:238–244, 1993.

[29] R.E. Dyball, R. Grossmann, G. Leng, and K. Shibuki. Spike propagation and conduction failure in the rat neural lobe. *The Journal of Physiology*, 401:241–256, 1988.

[30] G. B. Ermentrout and D.H. Terman. *Mathematical Foundations of Neuroscience*. Springer, 2010.

[31] G.B. Ermentrout. Mathematical foundations of neuroscience. *Springer*, 2010.

[32] C.G. Evans, B. Ludwar, and E.C. Cropper. Mechanoafferent neuron with an inexcitable somatic region: consequences for the regulation of spike propagation and afferent transmission. *Journal of Neurophysiology*, 97:3126–3130, 2007.

[33] M. Fainaru-Wada and S. Fainaru. League of denial: The nfl, concussions, and the battle for truth. *Crown Archetype*, 2013.

[34] M. Faul, L. Xu, M. M. Wald, and V. G. Coronado. Traumatic brain injury in the united states: emergency department visits, hospitalizations, and deaths. *Atlanta (GA): Centers for Disease Control and Prevention, National Center for Injury Prevention and Control*, 2010.

[35] Imran Fayanz and Charles H. Tator. Modeling axonal injury in vitro: injury and regeneration following acute neuritic trauma. *Journal of Neuroscience Methods*, 102:69–79, 2000.

[36] D. Feeney, M.G. Boyeson, R.T. Linn, H.M. Murray, and W.G. Dail. Responses to cortical injury: I methodology and local effects of contusion in the rat. *Brain Research*, 211:67–77, 1981.

[37] M. K. Ferguson, B.and Matyszak, M. M. Esiri, and V. H. Perry. Axonal damage in acute multiple sclerosis lesions. *Brain*, 120:393–399, 1997.

[38] J. C. Fiala, J. Spacek, and K. M. Harris. Dendritic spine pathology: cause or consequence of neurological disorders? *Brain Research Reviews*, 39:29–54, 2002.

[39] R. Fitzhugh. Impulses and physiological states in theoretical models of nerve membrane. *Biophysical Journal*, 1(6):445–466, 1961.

[40] J. E. Galvin, K. Uryu, V. M. Lee, and J. Q. Trojanowski. Axon pathology in parkinsons disease and lewy body dementia hippocampus contains α-, β-, and γ-synuclein. *Proceedings of National Academy of Science*, 96:13450–13455, 1999.

[41] W. Gerstner and W.M. Kistler. *Spiking Neuron Models*. Cambridge University Press, 2002.

[42] N. Gogolla, I. Galimberti, and P. Caroni. Structural plasticity of axon terminals in the adult. *Current Opinion in Neurobiology*, 17:516–524, 2007.

[43] M.D. Goldfinger. Rallian "equivalent" cylinders reconsidered: comparisons with literal compartments. *Journal of Integrative Neuroscience*, 4(2):227–263, 2005.

[44] S.S. Goldstein and W. Rall. Changes of action potential shape and velocity for changing core conductor geometry. *Biophysical Journal*, 14:731–757, 1974.

[45] M.S. Grady, M.R. Mclaughlin, C.W. Christman, A.B. Valadaka, C.L. Flinger, and J.T. Povlishock. The use of antibodies against neurofilament subunits for the detection of diffuse axonal injury in humans. *Journal of Neuropathology and Experimental Neurology*, 52:143–152, 1993.

[46] Y. Grossman, I. Parnas, and M.E. Spira. Differential conduction block in branches of a bifurcating axon. *The Journal of Physiology*, 295:283–305, 1979.

[47] Y. Grossman, I. Parnas, and M.E. Spira. Mechanisms involved in differential conduction of potentials at high frequency in a branching axon. *The Journal of Physiology*, 295:307–322, 1979.

[48] X. N. Gu. Effect of conduction block at axon bifurcations on synaptic transmission to different postsynaptic neurones in the leech. *The Journal of Physiology*, 441:755–778, 1991.

[49] H. Hatt and D.O. Smith. Synaptic depression related to presynaptic axon conduction block. *The Journal of Physiology*, 259:367393, 1976.

[50] Stephen L. Hauser and Jorge R. Oksenberg. The neurobiology of multiple sclerosis: Genes, inflammation, and neurodegeneration. *Neuron*, 52(1):61–76, 2006.

[51] Amy N. Hellman, Behrad Vahidi, Hyung Joon Kim, Wael Mismar, Oswald Steward, Noo Li Jeonde, and Vasan Venugopalan. Examination of axonal injury and regeneration in micropatterned neuronal culture using pulsed laser microbeam dissection. *Lab on a Chip*, 16:20832092, 2010.

[52] M.A. Hemphill, B.E. Dabiri, S. Gabriele, L. Kerscher, C. Franck, J.A. Goss, P.W. Alford, and K.K. Parker. A possible role for integrin signaling in diffuse axonal injury. *PLos ONE*, 6(7):e22899, 2011.

[53] B. Hille. *Ionic channels of excitable membranes*. Sinauer Associates, Sunderland, MA, 1988.

[54] M.L. Hines and N.T. Carnevale. The neuron simulation environment. *Neural Computation*, 9:1179–1209, 1997.

[55] A. Holtmaa and K. Svoboda. Experience-dependent structural synaptic plasticity in the mammalian brain. *Nature Reviews Neuroscience*, 10(9):647–658, 2009.

[56] Segev I. and Rall W. Excitable dendrites and spines: earlier theoretical insights elucidate recent direct observations. *Trends in Neuroscience*, 21(11):453–460, 1998.

[57] E.M. Izhikevich. *Dynamical systems in neuroscience: the geometry of excitability and bursting.* MIT Press., 2007.

[58] M.B. Jackson and S.J. Zhang. Action potential propagation and propagation block by gaba in rat posterior pituitary nerve terminals. *The Journal of Physiology*, 483:597–611, 1995.

[59] V. E. Johnson, W. Stewart, and D. H. Smith. Axonal pathology in traumatic brain injury. *Experimental Neurology*, 246:35–43, 2013.

[60] R. E. Jorge, L. Acion, T. White, D. Tordesillas-Gutierrez, R. Pierson, B. Crespo-Facorro, and V.A. Magnotta. White matter abnormalities in veterans with mild traumatic brain injury. *American Journal of Psychiatry*, 169(12):1284–1291, 2012.

[61] James Keener and James Sneyd. *Mathematical Physiology*. Springer, Interdisciplinary Applied Mathematics, 1998.

[62] B.I. Khodorov and E.N. Timin. Nerve impulse propagation along nonuniform fibres. *Progress in Biophysics and Molecular Biology*, 30(23):145–184, 1975.

[63] Katarina V. Kolaric, Gemma Thomson, Julia M. Edgar, and Angus M Brown. Focal axonal swellings and associated ultrastructural changes attenuate conduction velocity in central nervous system axons: a computer modeling study. *Physiological reports*, 1(3):e00059, 2013.

[64] K. Krnjevic and R. Miledi. Presynaptic failure of neuromuscular propagation in rats. *The Journal of Physiology*, 149:1–22, 1959.

[65] D. Krstic and I. Knuesel. Deciphering the mechanism underlying late-onset alzheimer disease. *Nature Reviews Neuroscience*, 9(1):25–34, 2012.

[66] J.N. Kutz. *Data-driven modeling and scientific computing.* Oxford Press, 2013.

[67] P. P. Liberski and H. Budka. Neuroaxonal pathology in creutzfeldt-jakob disease. *Acta Neuropathology*, 97:329–334, 1999.

[68] P. P. Liberski and H. Budka. Neuroaxonal pathology in creutzfeldt-jakob disease. *Acta Neuropathology (Berlim)*, 97:329–334, 2008.

[69] C. Luscher, J. Streit, P. Lipp, and H.R. Luscher. Action potential propagation through embryonic dorsal root ganglion cells in culture. ii. decrease of conduction reliability during repetitive stimulation. *Journal of Neurophysiology*, 72:634–643, 1994.

[70] H.R. Luscher and Shiner J.S. Simulation of action potential propagation in complex terminal arborizations. *Biophysical Journal*, 58(6):1389–1399, 1990.

[71] H.R. Luscher and J.S. Shiner. Computation of action potential propagation and presynaptic bouton activation in terminal arborizations of different geometries. *Biophysical Journal*, 58(6):1377–1388, 1990.

[72] M. H. Magdesian, F. S. Sanchez, M. Lopez, P. Thostrup, N. Durisic, W. Belkaid, D. Liazoghli, P. Grütter, and R. Colman. Atomic force microscopy reveals important differences in axonal resistance to injury. *Biophysical Journal*, 103(3):405–414, 2012.

[73] Pedro D. Maia and J. Nathan Kutz. Compromised axonal functionality after neurodegeneration, concussion and/or traumatic brain injury. *Journal of Computational Neuroscience*, 27:317–332, 2014.

[74] Pedro D. Maia and J. Nathan Kutz. Identifying critical regions for spike propagation in axon segments. *Journal of Computational Neuroscience*, 36(2):141–155, 2014.

[75] Y. Manor, J. Gonczarowski, and I. Segev. Propagation of action potentials along complex axonal trees. model and implementation. *Biophysical Journal*, 60(6):1411–1423, 1991.

[76] Y. Manor, C. Koch, and I. Segev. Effect of geometrical irregularities on propagation delay in axonal trees. *Biophysical Journal*, 60:1424–1437, 1991.

[77] D. Marcuse. *Theory of dielectric optical waveguides.* Academic Press, 1974.

[78] A. Marmarou. A new model of diffuse brain injury in rats. part i: pathophysiology and biomechanics. *Journal of Neurosurgery*, 80:291–300, 1994.

[79] M. Mascagni. The backward euler method for numerical solution of the hodgkin-huxley equations of nerve conduction. *SIAM Journal on Numerical Analysis*, 27(4):941–962, 1990.

[80] W. L. Maxwell, J. T. Povlishock, and D. L. Graham. A mechanistic analysis of nondisruptive axonal injury: A review. *Journal of Neurotrauma*, 17(7):419–440, 1997.

[81] J.P. Meeks and S. Mennerick. Selective effects of potassium elevations on glutamate signaling and action potential conduction in hippocampus. *Journal of Neuroscience*, 24:197–206, 2004.

[82] S. Millecamps and J.P. Julien. Axonal transport deficits and neurodegenerative diseases. *Nature Reviews Neuroscience*, 14(161):161–176, 2013.

[83] R.M. Miura. Accurate computation of the stable solitary wave for the fitzhugh-nagumo equations. *Journal of Mathematical Biology*, 13(3):247–269, 1982.

[84] Barclay Morrison, Benjamin S. Elkin, Jean Pierre Dolle, and Martin L. Yarmush. In vitro models of traumatic brain injury. *Annual Reviews in Biomedical Engineering*, 13(1):91–126, 2011.

[85] S. Arimoto Nagumo and S. Yoshizawa. An active pulse transmission line simulating nerve axon. *Proceedings of the IRE*, 50(10):2061–2070, 1962.

[86] Ivana Nikic, Doron Merkler, Catherine Sorbara, Mary Brinkoetter, Mario Kreutzfeld, Florence Bareyre, Wolfgang Bruck, Derron Bishop, Thomas Misgeld, and Martin Kerschensteiner. A reversible form of axon damage in experimental autoimmune encephalomyelitis and multiple sclerosis. *Nature Medicine*, 17(4):495–499, 2011.

[87] S.N. Niogi, P. Mukherjee, J. Ghajar, C. Johnson, R.A. Kolster, R. Sarkar, H. Lee, M. Meeker, R.D. Zimmerman, G.T. Manley, and B.D. Mccandliss. Extent of microstructural white matter injury in postconcussive syndrome correlates with impaired cognitive reaction time: A 3t diffusion tensor imaging study of mild traumatic brain injury. *American Journal of Neuroradiology*, 29(5):967–973, 2008.

[88] I. Parnas. Differential block at high frequency of branches of a single axon innervating two muscles. *Journal of Neurophysiology*, 35:903–914, 1972.

[89] I. Parnas. Propagation in nonuniform neurites: form and function in axons. *The Neurosciences, Cambridge, MIT Press*, pages 499–512, 1979.

[90] I. Parnas, S. Hochstein, and H. Parnas. Theoretical analysis of parameters leading to frequency modulation along an inhomogeneous axon. *Journal of Neurophysiology,*, 39(4), 1976.

[91] D. P. Purpura, N. Bodick, K. Suzuki, I. Rapin, and S. Wurzelmann. Microtubule disarray in cortical dendrites and neurobehavioral failure. i. golgi and electron microscopy studies. *Developing Brain Research*, 5:287–297, 1982.

[92] W. Rall. Branching dendritic trees and motoneuron membrane resistivity. *Experimental Neurology*, 1:491–527, 1959.

[93] W. Rall. Theory of physiological properties of dendrites. *Annals of the New York Academy of Sciences.*, 1962.

[94] W. Rall and J. Shepherd. Theoretical reconstruction of field potentials and dendrodendritic synaptic interactions in olfactory bulb. *Journal of Neurophysiology*, 173, 1968.

[95] F. Ramon, R.W Joyner, and J.W. Moore. Propagation of action potentials in inhomogeneous axon regions. *Federation proceedings*, 34:1357–1363, 1975.

[96] J. Rinzel. Mechanisms for nonuniform propagation along excitable cables. *Annals of the New York Academy of Sciences*, 591, 1990.

[97] V. Rubovitch, M. Ten-Bosch, O. Zohar, C.R. Harrison, C. Tempel-Brami, E. Stein, B.J. Hoffer, C. Balaban, S. Schreiber, W.T. Chiu, and C.G. Pick. A mouse model of blast-induced mild traumatic brain injury. *Experimental Neurology*, 232(2):280–289, 2011.

[98] A. Scott. *Neuroscience: a mathematical primer.* Springer, 2002.

[99] I. Segev, J. Rinzel, and Shepherd G.M. (eds.). he theoretical foundation of dendritic function: Selected papers of wilfred rall with commentaries. *Bradford/MIT Press, Cambridge.*, 1995.

[100] I. Segev and E. Schneidman. Axons as computing devices: basic insights gained from models. *The Journal of Physiology*, 93:263–270, 1999.

[101] David J. Sharp, Gregory Scott, and Robert Leech. Network dysfunction after traumatic brain injury. *Nature Reviews Neurology*, 10:156–166, 2014.

[102] G.M.G. Shepherd and K. Harris. Three-dimensional structure and composition of ca3 to ca1 axons in rat hippocampal slices: implications for presynaptic connectivity and compartmentalization. *Journal of Neuroscience*, 18(20):8300–8310, 1998.

[103] Eli Shlizerman, Jeffrey A. Riffell, and J. Nathan Kutz. Data-driven inference of network connectivity for modeling the dynamics of neural codes in the insect antennal lobe. *Frontiers in Computational Neuroscience*, 8(70):1–15, 2014.

[104] E. Shohami, Y. Shapira, and S. Cotev. Experimental closed head injury in rats: prostaglandin production in a noninjured zone. *Neurosurgery*, 22:859–863, 1988.

[105] D.H. Smith, J.W. Wolf, T.A. Lusardi, V.M.Y. Lee, and D.F. Meaney. High tolerance and delayed elastic response of cultured axons to dynamic stretch injury. *The Journal of Neuroscience*, 19(11):4263–4269, 1999.

[106] D.O. Smith. Mechanisms of action potential propagation failure at sites of axon branching in the crayfish. *The Journal of Physiology*, 301:243–259, 1980.

[107] A.F. Soleng, K. Chiu, and M. Raastad. Unmyelinated axons in the rat hippocampus hyperpolarize and activate an h current when spike frequency exceeds 1 hz. *The Journal of Physiology*, 552:459–470, 2003.

[108] M. D. Tang-Schomer, V. E. Johnson, P. W. Baas, W. Stewart, and D. H. Smith. Partial interruption of axonal transport due to microtubule breakage accounts for the formation of periodic varicosities after traumatic axonal injury. *Experimental Neurology*, 233:364–372, 2012.

[109] M. D. Tang-Schomer, A.R. Patel, P. W. Bass, and D. H. Smith. Mechanical breaking of microtubules in axons during dynamic stretch injury underlies delayed elasticity, microtubule disassembly, and axon degeneration. *The FASEB Journal*, 24(5):1401–1410, 2010.

[110] B.D. Trapp, J. Peterson, R.M. Ransohoff, R. Rudick, S. Mrk, and L. B. Axonal transection in the lesions of multiple sclerosis. *The New England Journal of Medicine*, 338:278–285, 1998.

[111] Bruce D Trapp and Klaus-Armin Nave. Multiple sclerosis: An immune or neurodegenerative disorder? *Annual Review Neuroscience*, 31(1):247–269, 2008.

[112] L.N. Trefethen. *Spectral Methods in Matlab*. SIAM, 2000.

[113] J. Tsai, J. Grutzendler, K. Duff, and W. B. Gan. Fibrillar amyloid deposition leads to local synaptic abnormalities and breakage of neuronal branches. *Nature Neuroscience*, 7:1181–1183, 2004.

[114] Henry Tuckwell. *Introduction to theoretical neurobiology: linear cable theory and dendritic structure*. Cambridge Press, 1988.

[115] D.C. Van Essen. The contribution of membrane hyperpolarization to adaptation and conduction block in sensory neurons of the leech. *The Journal of Physiology*, 230:509534, 1973.

[116] J. D. Victor. Spike train metrics. *Current opinion in Neurobiology*, 15:585–592, 2005.

[117] J. D. Victor and K. P. Purpura. Metric space analysis of spike trains: theory, algorithms and application. *Network: Computational Neural Systems*, 8:127–164, 1997.

[118] A. Vladimirescu, K. Zhang, A.R. Newton, D.O. Pederson, and A. Sangiovanni-Vincentelli. Spice version 2g user's guide. department of electrical engineering and computer sciences. *University of California, Berkeley*, 1981.

[119] J. Wang, R. J. Hamm, and J. T. Povlishock. Traumatic axonal injury in the optic nerve: evidence for axonal swelling, disconnection, dieback and reorganization. *Journal of Neurotrauma,*, 28(7):1185–1198, 2011.

[120] Y. Xiong, A. Mahmood, and M. Chopp. Animal models of traumatic brain injury. *Nature Reviews Neuroscience*, 14(22):128–142, 2013.

[121] K. Xylouris, G. Queisser, and G. Wittum. A three-dimensional mathematical model of active signal processing in axons. *Computing and Visualization in Science*, 13(8):409–418, 2010.

[122] K.W Yau. Receptive fields, geometry and conduction block of sensory neurones in the central nervous system of the leech. *The Journal of Physiology*, 263:513–538, 1976.

[123] S.J. Zhang and M.B. Jackson. Gaba-activated chloride channels in secretory nerve endings. *Science*, 259:531–534, 1993.

[124] Y. Zhou and J. Bell. Study of propagation along nonuniform excitable fibers. *Mathematical Biosciences*, 119(2):169–203, 1994.